THE CONTOUR-ADVECTIVE SEMI-LAGRANGIAN HYBRID ALGORITHM APPROACH TO WEATHER FORECASTING AND FREELY PROPAGATING INERTIA-GRAVITY WAVES IN THE SHALLOW-WATER SYSTEM

Robert K. Smith

A Thesis Submitted for the Degree of PhD
at the
University of St. Andrews

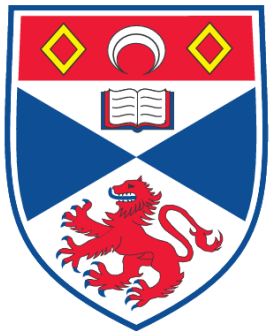

2009

UNIVERSITY OF ST ANDREWS

The Contour-Advective Semi-Lagrangian hybrid algorithm approach to weather forecasting and freely propagating inertia-gravity waves in the shallow-water system

by

Robert K. Smith

A thesis submitted in partial fulfillment for the degree of Doctor of Philosophy

in the

Vortex Dynamics Research Group

Department of Applied Mathematics

September 2008

Declaration of Authorship

I, Robert K. Smith, declare that this thesis has ben composed by myself, that it is a record of my own work and that it has not been accepted in any previous application for any degree.

Signed:

Date:

I was admitted as a research student in October 2001 and as a candidate for the degree of PhD in October 2001; the higher study for which this is a record was carried out in the University of St Andrews between 2001 and 2008 on a part-time basis.

Signed:

Date:

I hereby certify that the candidate has fulfilled the conditions of the Resolution and Regulation appropriate for the degree of PhD in the University of St Andrews and that the candidate is qualified to submit this thesis in application for that degree.

Signed:

Date:

Abstract

This thesis is aimed at extending the spherical barotropic contour-advective semi-Lagrangian (CASL) Algorithm, written in 1996 by David Dritschel and Maarten Ambaum, to more complex test cases within the shallow-water context. This is an integral part for development of any numerical model and the accuracy obtained depends on many factors, including knowledge of the initial state of the atmosphere or ocean, the numerical methods applied, and the resolutions used.

The work undertaken throughout this thesis is highly varied andy produces important steps towards creating a versatile suite of programs to model all types of flow, quickly and accurately. This, as will be explained in later chapters, impacts both public safety and the world economy, since much depends on accurate medium range forecasting. There shall be an investigation of a series of tests which demonstrate certain aspects of a dynamical system and its progression into more unstable situations — including the generation and feedback of freely propagating inertia-gravity waves (hereafter "gravity waves"), which transmit throughout the system. The implications for increasing forecast accuracy will be discussed.

Within this thesis two main CASL algorithms are outlined and tested, with the accuracy of the results compared with previous results. In addition, other dynamical fields (besides geopotential height and potential vorticity) are analysed in order to assess how well the models deal with gravity waves. We shall see that such waves are sensitive to the presence, or not, of sharp potential vorticity gradients, as well as to numerical parameter settings. In particular, large time-steps (convenient for semi-Lagrangian schemes) may not only seriously affect gravity waves, but may also have an adverse impact on the primary fields of height and velocity. These problems are exacerbated by a poor resolution of potential vorticity gradients, which we shall attempt to improve.

Acknowledgements

Many thanks go to my family and friends for their continued support and of course to the University of St Andrews and Professor David Dritschel[1] for their guidance and thought provocation throughout my research.

[1]David Dritschel, Mathematics Dept. University of St Andrews, North Haugh, KY16 9SS. dgd@mcs.st-andrews.ac.uk

Contents

List of Figures

List of Tables

Symbols

Symbol	Description
x, y, z	Cartesian Coordinate system
$\mathbf{i}, \mathbf{j}, \mathbf{k}$	Unit vectors in (x, y, z) directions
t	Time
ϕ, λ	Latitude, Longitude
L, H	Horizontal and Vertical length scale
$\mathbf{u} = (u, v)$	Two-dimensional velocity components
p	Pressure
ρ	Density
g	Acceleration of gravity
$\Omega_E, \mathbf{\Omega}_E$	Rotation rate of Earth and associated vector
f	Coriolis parameter (constant)
ζ	Vorticity
q	Potential vorticity
ψ	Streamfunction
χ	Divergence potential
R_o	Rossby number, U/fL
F_r	Froude number
$\mathbf{v} = (u, v, w)$	Three-dimensional velocity components

This thesis is dedicated to my daughter, Megan, born 7^{th} February 2007 weighing 7lb 0oz.

Chapter 1

The shallow-water system

1.1 Introduction

This thesis concentrates on using a Contour-Advective numerical method [13, 16] for solving the Shallow Water Equations (SWEs), which describe the motion of a thin layer of fluid held down by gravity. The details of the SWEs are outlined in many books (e.g. see Bibliography: [30, 53]) and have been used as an idealised model of a planet's atmosphere or oceans for many years. They are capable of describing diverse nonlinear fluid phenomena, including vortices and gravity waves, over a broad range of spatial and temporal scales.

This flexibility means that a comprehensive understanding of their solution properties is difficult to achieve. However, by studying these (single and multi-layer [51]) models a surprisingly accurate picture of meso and large-scale flows in the continuously stratified ocean or atmosphere can be gained. This has become of particular importance in recent years, with Global Circulation Models (GCMs) forecasting large-scale atmospheric evolution over a period of decades, leading to valuable insights into the possible ways our climate could change.

1.2 The single-layer SWEs

Fluid dynamics is characterised by both wave propagation and advection in and out of different regions, which allows certain properties of the fluid, such as the density, to change. Other properties, like the mass, which cannot be created or destroyed, only change due to the transport of mass across each region interface. There is therefore the requirement of an explicit equation, that must be satisfied at all times, ensuring the conservation of mass over the entire fluid region. In addition, we will need to know how a fluid element will react to forces imposed on it, taken from Newton's laws of motion, describing the rate of change of momentum of a body under an external force.

1.2.1 The spherical coordinate system

As the Earth can be taken as approximately spherical, many current global circulation models use a spherical coordinate system and the algorithms detailed within this thesis are no exception. We will use the meteorological definition of spherical coordinates, shown in figure (1.1), where λ is the azimuthal angle from the x-axis[1] with $0 \leq \lambda \leq 2\pi$ and where ϕ is the polar angle from the equatorial plane[2], with $-\pi/2 \leq \phi \leq \pi/2$. We must also consider the rotation of the Earth, which requires all frames of reference to include a rotational vector, $\mathbf{\Omega}_E$.

Taking an inviscid (negligible friction), adiabatic fluid element (one not subject to external heating), the equations expressing momentum balance (Euler's equation)

[1] θ is denoted λ when referred to as the longitude.
[2] $\varphi = 90° - \phi$, where ϕ is the latitude.

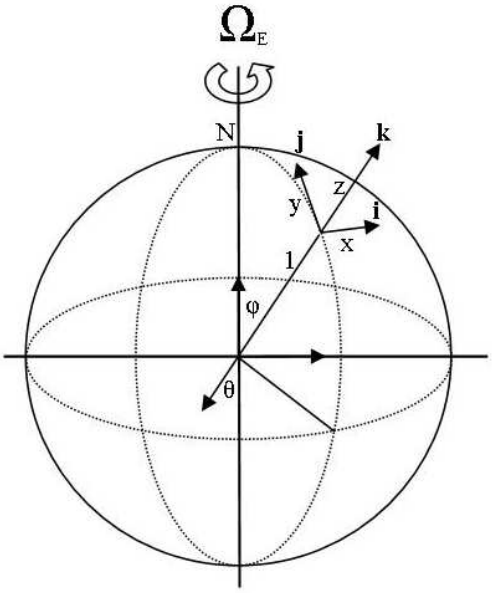

FIGURE 1.1: The unit sphere outlining the spherical polar coordinate system

and mass continuity can be expressed as follows, [30],

$$\frac{\mathrm{D}\mathbf{u}}{\mathrm{D}t} + 2\boldsymbol{\Omega}_E \times \mathbf{u} = -\boldsymbol{\nabla}\Phi\,, \tag{1.1}$$

$$\frac{\partial \Phi}{\partial t} + \boldsymbol{\nabla}\cdot(\Phi\mathbf{u}) = 0 \tag{1.2}$$

where $\mathbf{u}$ is the layer mean horizontal velocity, $\Phi = gh$ is the geopotential (the potential energy of a unit mass, relative to $h = 0$ taken as sea level) and h is the local fluid height. The geopotential embodies hydrostatic balance, which states that the pressure increases with depth, i.e. the force of gravity (buoyancy)must balance the vertical pressure gradient, from which one obtains the hydrostatic balance relation

$$\frac{\partial p}{\partial z} = -\rho g\,. \tag{1.3}$$

If the density, ρ, remains constant, then equation (1.3) implies that the horizontal flow is independent of the height and vertical acceleration is negligible.

Indeed, in the shallow-water system, the horizontal scale of the flow is much larger

FIGURE 1.2: Flows, like the above gravity wave structure, in the atmosphere are shallow with only weak vertical motions, leading to density (or temperature) surfaces which can be taken as nearly horizontal

than the depth of the fluid and therefore, in equation (1.2), only components parallel to the Earth's surface are retained. An example can clearly be seen in figure (1.2) with a large scale structure being far wider than it is tall.

We also non-dimensionalise lengths by the Earth's radius (not shown, although commonly denoted a), and time by $T_{day} = 2\pi/\Omega_E$, where the rotational frequency $\Omega_E = 7.292 \times 10^{-5} s^{-1}$. That is, our unit of length is the radius of the Earth and unit of time is one day.

Furthermore, the shallow-water approximation retains only the local vertical component of the rotational vector and hence we can define the *Coriolis parameter* (or frequency) as $f = 2\Omega_E \sin\phi$. Upon taking a local vertical unit vector, $\mathbf{k}$, this

leads to the momentum equation, (1.1), in the standard SWE form,

$$\frac{\mathrm{D}\mathbf{u}}{\mathrm{D}t} + f\mathbf{k}\times\mathbf{u} = -\boldsymbol{\nabla}\Phi\,. \tag{1.4}$$

1.3 Vorticity and divergence

Taking (x, y, z) as local Cartesian coordinates pointing eastwards, northwards and upwards, the two-dimensional velocity (denoted $\mathbf{u} = (u, v)$) consists of just two components, u and v, directed eastward and northward respectively. On a sphere of unit radius, we have $dx = rd\lambda$ and $dy = d\phi$, where λ and ϕ denote longitude and latitude respectively, and $r = \cos\phi$ is the horizontal radius from the axis of rotation.

The curl (denoted $\boldsymbol{\nabla}\times$) and divergence ($\boldsymbol{\nabla}\cdot$) of the velocity field, lead us to the vorticity (denoted ζ) and divergence (δ) fields, which completely define the flow. As such, instead of using u and v, many numerical algorithms use the vorticity and divergence

$$\zeta = \frac{1}{r}\frac{\partial v}{\partial\lambda} - \frac{1}{r}\frac{\partial}{\partial\phi}(ru)\,, \tag{1.5}$$

$$\delta = \frac{1}{r}\frac{\partial u}{\partial\lambda} + \frac{1}{r}\frac{\partial}{\partial\phi}(rv) \tag{1.6}$$

as the prognostic variables (most convenient for spectral models where the horizontal derivatives can be calculated exactly).

Within the SWEs, the fluid height is also separated into a constant mean value, H, and a deviation, h', i.e. $h = H + h'$. The mean short-scale gravity wave speed may then be defined as $c = \sqrt{gH}$. In the following, we make use of the dimensionless height anomaly given by $\tilde{h} = h'/H$.

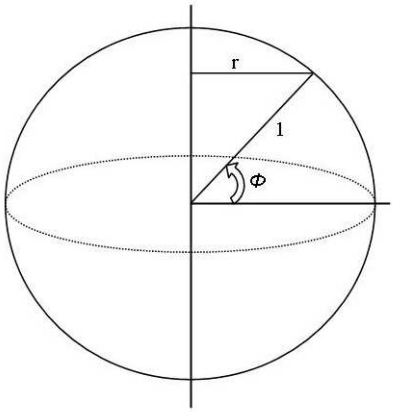

FIGURE 1.3: Diagram showing the basic spherical geometry layout to compliment the definition of the SWEs on the unit sphere in equations (1.7) to (1.9).

In spherical coordinates, with $r \equiv \cos\phi$, as in figure (1.3), the SWEs take the form

$$\frac{\mathrm{D}u}{\mathrm{D}t} - fv + uv\tan\phi = -\frac{c^2}{r}\frac{\partial\tilde{h}}{\partial\lambda}\,, \tag{1.7}$$

$$\frac{\mathrm{D}v}{\mathrm{D}t} + fu - u^2\tan\phi = -c^2\frac{\partial\tilde{h}}{\partial\phi}\,, \tag{1.8}$$

$$\frac{\partial\tilde{h}}{\partial t} + \boldsymbol{\nabla}\cdot((1+\tilde{h})\mathbf{u}) = 0\,. \tag{1.9}$$

Therefore, the full equations in terms of our shallow-water variables ζ, δ and $\tilde{h}$ become

$$\frac{\partial\zeta}{\partial t} + f\delta = -\boldsymbol{\nabla}\cdot(\mathbf{u}\zeta)\,, \tag{1.10}$$

$$\frac{\partial\delta}{\partial t} + c^2\boldsymbol{\nabla}^2\tilde{h} - f\zeta = 2J(u,v) - \boldsymbol{\nabla}\cdot(\mathbf{u}\cdot\boldsymbol{\nabla}\mathbf{u})\,, \tag{1.11}$$

$$\frac{\partial\tilde{h}}{\partial t} + \delta = -\boldsymbol{\nabla}\cdot(\mathbf{u}\tilde{h})\,, \tag{1.12}$$

where J is the Jacobian operator,

$$J(u,v) = \frac{1}{r}\left(\frac{\partial u}{\partial \lambda}\frac{\partial v}{\partial \phi} - \frac{\partial u}{\partial \phi}\frac{\partial v}{\partial \lambda}\right) .$$

Streamfunctions, ψ and χ, of the two-dimensional flow can be defined such that the flow velocity is given by the relation

$$\mathbf{u} = \mathbf{k} \times \boldsymbol{\nabla}\psi + \boldsymbol{\nabla}\chi \,, \tag{1.13}$$

where $\mathbf{k}$ is the local vertical unit vector. Here, χ is commonly referred to as the divergence potential, see equation (1.16) below. This separation into rotational and divergent parts is called the "Helmholtz decomposition".

With the Laplace-Beltrami operator for a sphere of unit radius,

$$\boldsymbol{\nabla}^2 = \frac{1}{\cos^2\phi}\frac{\partial^2}{\partial \lambda^2} + \frac{1}{\cos\phi}\frac{\partial}{\partial \phi}\left(\cos\phi \frac{\partial}{\partial \phi}\right) , \tag{1.14}$$

the vorticity and divergence are related to ψ and χ via

$$\boldsymbol{\nabla}^2\psi = \zeta \,, \tag{1.15}$$

$$\boldsymbol{\nabla}^2\chi = \delta \,. \tag{1.16}$$

Hence, the velocity components are recovered from ζ and δ by solving the Poisson equations (1.15) and (1.16) for ψ and χ and differentiating them in equation (1.13).

1.3.1 Potential vorticity

Divergence and vorticity play a large part in the numerical method. However an even more important dynamical quantity can be derived, namely the *Potential*

Vorticity (hereafter PV). Since this is a central quantity in the contour-advective method, the fundamental significance of PV shall be outlined, following [72].

Given the shallow-water momentum equation in the form

$$\frac{\mathrm{D}\mathbf{u}}{\mathrm{D}t} + \mathbf{f} \times \mathbf{u} = -c^2 \boldsymbol{\nabla} \tilde{h} \,, \tag{1.17}$$

where $\mathbf{f} = f\mathbf{k}$, we can define a vector as the curl of the horizontal velocity alone ($\boldsymbol{\omega} = \boldsymbol{\nabla} \times \mathbf{u}$) which, due to the fact that the horizontal components of $\boldsymbol{\omega}$ are zero, means

$$\boldsymbol{\omega} = \mathbf{k}\zeta \,. \tag{1.18}$$

After re-arranging equation (1.17) in the following form

$$\frac{\partial \mathbf{u}}{\partial t} + (\boldsymbol{\omega} + \mathbf{f}) \times \mathbf{u} = -\boldsymbol{\nabla} \left(c^2 \tilde{h} + \frac{|\mathbf{u}|^2}{2} \right) \,, \tag{1.19}$$

taking its curl and using the vector identity

$$(\mathbf{u} \cdot \boldsymbol{\nabla})\mathbf{u} = \frac{1}{2}\boldsymbol{\nabla}(\mathbf{u} \cdot \mathbf{u}) - \mathbf{u} \times (\boldsymbol{\nabla} \times \mathbf{u}) = \frac{1}{2}\boldsymbol{\nabla}(|\mathbf{u}|^2) - \mathbf{u} \times \boldsymbol{\omega} \,,$$

we arrive at the vorticity equation

$$\frac{\partial \zeta}{\partial t} + (\mathbf{u} \cdot \boldsymbol{\nabla})(\zeta + f) + (f + \zeta)\boldsymbol{\nabla} \cdot \mathbf{u} = 0 \,, \tag{1.20}$$

or

$$\frac{\partial \zeta}{\partial t} + (\mathbf{u} \cdot \boldsymbol{\nabla})(\zeta + f) + (\zeta + f)\delta = 0 \,. \tag{1.21}$$

Using the definition of the material derivative, $\mathrm{D}/\mathrm{D}t = \partial/\partial t + \mathbf{u} \cdot \boldsymbol{\nabla}$ and combining equation (1.21) and (1.12), one finds the expression of material PV conservation, namely

$$\frac{\mathrm{D}q}{\mathrm{D}t} = 0 \,, \tag{1.22}$$

where

$$q \equiv \frac{\zeta + f}{1 + \tilde{h}} \tag{1.23}$$

is the PV in a rotating shallow-water system, first derived by Rossby, [60] and in a general form by Ertel, [22–25].

PV is a unique variable, not only because of its material conservation (essential in semi-Lagrangian and CASL algorithms) in the absence of dissipation and heating, but also because of the role it plays in "balance" or PV inversion (see [17, 38, 44, 49] and section 1.5 below).

PV is the primary field used to follow the evolution of fluid elements, as seen e.g. in the atmosphere and oceans, and will feature strongly in Chapter 2, when we come to describe the model in detail. The SWEs in terms of the prognostic variables $(q, \delta, \tilde{h})$ used by the algorithm are the set of equations

$$\frac{\mathrm{D}q}{\mathrm{D}t} = 0\,, \tag{1.24}$$

$$\frac{\partial \delta}{\partial t} + c^2 \boldsymbol{\nabla}^2 \tilde{h} - f^2 \tilde{h} = f(\zeta - f\tilde{h}) + 2J(u,v) - \boldsymbol{\nabla} \cdot (\mathbf{u} \cdot \boldsymbol{\nabla}\mathbf{u})\,, \tag{1.25}$$

$$\frac{\partial \tilde{h}}{\partial t} + \delta = -\boldsymbol{\nabla} \cdot (\mathbf{u}\tilde{h})\,. \tag{1.26}$$

1.4 Elliptic equations and the concept of balance

As previously mentioned, the vorticity and divergence are paramount to modelling flow on the sphere and so, to obtain (u, v) from ζ and δ, one must solve the Poisson equations for the streamfunction and divergence potential, seen previously as

$$\boldsymbol{\nabla}^2 \psi = \zeta\,, \quad \boldsymbol{\nabla}^2 \chi = \delta\,.$$

These are examples of elliptic equations. Using the relations

$$u = \frac{1}{r}\frac{\partial \chi}{\partial \lambda} - \frac{\partial \psi}{\partial \phi} \quad \text{and} \quad v = \frac{\partial \chi}{\partial \phi} + \frac{1}{r}\frac{\partial \psi}{\partial \lambda}\,,$$

the velocity components then may be computed directly.

Other elliptic equations may arise e.g. in the numerical time-stepping (see section 2.3) and also when diagnosing "balance", here defined as the component of the flow directly attributable to PV. This gives rise to the Helmholtz operator, $\mathcal{H}$, defined by

$$\mathcal{H} = \boldsymbol{\nabla}^2 - \frac{f^2}{c^2}\,. \tag{1.27}$$

This operator already appears on the left hand side of equation (1.25).

1.5 Achieving balance

1.5.1 Balance in the atmosphere and oceans

In the Earth's atmosphere and oceans, and possibly other planetary atmospheres, [6], PV advection (generally) dominates inertia-gravity wave propagation and therefore the fluid motion principally depends on the PV distribution. This leads to the idea of imposing *balance relations* to extract the part of dynamics attributable to PV, [38]. Unfortunately, this approach is not precise and balance is, to some extent, ambiguous, e.g. [18, 38].

Given the general equation of motion (cf. equation (1.1)) in the form inclusive of pressure and density

$$\frac{\mathrm{D}\mathbf{u}}{\mathrm{D}t} + 2\boldsymbol{\Omega}_{\mathbf{E}} \times \mathbf{u} = -\frac{\boldsymbol{\nabla} p}{\rho} - \boldsymbol{\nabla}\Phi\,, \tag{1.28}$$

we can expect that (at least for sufficiently slow motions) a flow will exhibit approximate "geostrophic balance", and in which the Coriolis acceleration ($2\boldsymbol{\Omega}_E \times \mathbf{u}$) balances the horizontal pressure gradient (i.e. a sufficiently small Rossby number), and "hydrostatic balance", in which buoyancy ($\boldsymbol{\nabla}\Phi$) balances the vertical pressure gradient. However, balance can mean more than this — it can be defined in a multitude of ways, see e.g. [17, 18, 30, 44, 53, 71] amongst others.

As a consequence, there have been many approaches to diagnosing the balance within a dynamical system, e.g. see [45, 72] and references therein. However, these approaches have rarely been exploited in the design of accurate numerical algorithms. That is, while balance may dominate the flow evolution, this is not explicitly taken into account!

1.5.2 Balance within the numerical method

As will be discussed in Chapter 5.2, balance within numerical models can be understood in terms of the amount of gravity-wave excitation within the system. The concept of balance is supported by observational data, with observed flows often having little deviation or imbalance in the form of gravity waves, [45].

Erroneous gravity wave production is often thought of as the numerical breakdown of balance and a greater understanding of balance can be gained by studying a hierarchy of balance conditions, in various numerical algorithms, [49, 64, 74]. Detection and separation of these falsely generated gravity waves and those correctly

modelled is immensely challenging however, and these waves are sensitive to both resolution and the type of numerical algorithm used [17].

In order to compute the balance within a system we must distinguish between the large-scale motions, dominated by sub-inertial frequency vortical motions (described by the PV) and the higher frequency gravity waves, of generally weaker amplitude (not induced by PV), [11]. The problem with this wave-vortex decomposition (or balance-imbalance decomposition) is that it is not unique and so approximations must be made, based on reductions of the full non-linear equations. Where the gravity waves are artificially damped within a numerical model, this approximation also leads to a filtering of a significant portion of vortical motion, [17, 18, 45, 51, 64].

To accurately include wave-vortex decomposition in the algorithm, a careful choice of the prognostic variables must be made. We use directly the PV and, as will be outlined in a new approach, in Chapter 5.1, the remaining variables should be chosen such that they vanish in the limit of rapid rotation and strong stratification (i.e. small Rossby and Froude numbers, as we shall see in later chapters). These variables represent the imbalance to leading order, i.e. the departure from balance between flow variables assumed in the wave-vortex decomposition.

A more matched representation between PV and the other prognostic fields leads to a gain in accuracy, with less false generation of gravity waves within the system. Indeed, each addition in the algorithm hierarchy shows that it is possible to maintain non-linear balance in the presence of sharp PV gradients, without resorting to explicit diffusion. As discussed in [49], where there is an underlying balance within the system, this must be preserved by implementing that balance in the numerical algorithm. Otherwise, by transferring energy from vortices to waves erroneously (due to sometimes inevitable truncation errors), it is possible

to lose balance. This, of course, is most prevelant in low to medium resolutions and longer time simulations.

Chapter 2

The contour-advective semi-Lagrangian method

2.1 An introduction to discretisation

There are a number of techniques used to create and discretise the spherical domain, or sections thereof. Common methods include finite differencing, where a regular grid is superimposed on the sphere and the parameters of the SWEs are approximated by low order polynomials at the grid points. This is a simple and successful method, but may lead to areas requiring separate treatment, due to the inevitable irregularity of the grid. An extension of this method, which can reduce the grid problems, is that of finite elements. Here, a mesh of geometric shapes is used to fill the domain. The solution to the SWEs would then be approximated by smooth functions at the mesh intersections.

Spectral (and pseudo-spectral) methods use global functions, such as Fourier-Legendre (spherical harmonic) series or high order polynomials, to approximate

the solution of the partial differential equations by a system of ordinary differential equations and solving them using a time-stepping method. For more simple, well behaved systems of partial differential equations, spectral methods give a high degree of accuracy and efficient computation.

There are also more recent methods for efficiently solving the SWEs in spherical geometry. For example, the cubed sphere method, introduced for solving partial differential equations in [59], shows how starting with a regular grid over a cube you can expand the sides in order to generate six coordinate systems over a sphere, much like inflating a Rubik's cube.

We will also introduce the use of a new type of regular grid in Chapter 6, used in [51], which gives an improvement in accuracy compared with the 'standard' regular grid arrangement.

2.1.1 The hybrid approach

Due to the complex nature of global fluid dynamics within the SWEs, a hybrid approach is taken by the CASL method. This discretises the domain using spectral Fast Fourier Transforms (hereafter FFTs) in longitude and finite differencing in latitude. The computational expense of the FFTs, given N_λ longitudinal grid points, increases as $\mathcal{O}(N_\lambda \log N_\lambda)$ for each latitude circle, and finite differencing over N_ϕ latitudes, implemented via a tridiagonal solver routine, which is more efficient, requires $\mathcal{O}(N_\phi)$ operations per longitudinal wavenumber. The combined cost is therefore $\mathcal{O}(N_\phi N_\lambda \log N_\lambda)$. By contrast, a purely spectral method (using Legendre transforms) requires $\mathcal{O}(N_\lambda^3 \log N_\lambda)$ operations to invert Laplace's equation, [32, 42, 52].

2.2 Contour-advection

Eulerian advection is observed from a fixed point in space as the fluid evolves past that point. This means regular grid spacing is able to be maintained, but the numerical methods using this scheme will require very small time-steps in order to maintain stability. With Lagrangian advection, the observer follows a single fluid particle whilst the system evolves around them. This is typically a more stable method to compute numerically (with many methods applying larger time steps, discussed with the Rossby wave test case in Chapter 4) and allows fine-scale structure to be followed. However, the grid spacing does not stay rigid as the system evolves, potentially making computation more expensive as time progresses.

It seems feasible, therefore, to represent conservative tracer fields such as the PV, which typically contain fine-scale structures, in a Lagrangian form and fields without such properties in an Eulerian form. In order to maintain stability, yet employ the fastest possible methods, the CASL model does exactly this — using both Lagrangian and Eulerian representations within the algorithm, [13]. With this hybrid approach, CASL is able to increase model accuracy by resolving the fine scale structure, running below grid resolution, whilst actually increasing numerical computation efficiency (see Chapter 10.1 for previous results of computational time comparisons with another numerical method).

In addition, the CASL algorithm advects PV contours with a method known as "contour-advection", [38, 48, 54, 76]. The tracer field of PV is represented by a series of contours on a given (constant value) surface or level, shown in figure (2.1), with each contour represented by nodes. These nodes are then advected to their new position in time using the velocity, interpolated from an Eulerian

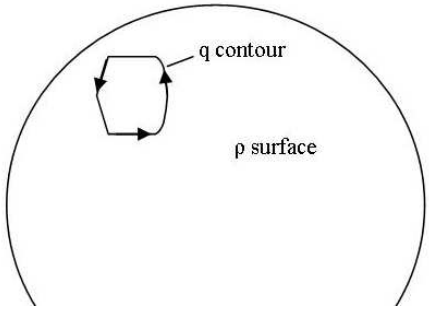

FIGURE 2.1: PV contour example on constant density shallow-water surface.

representation. This is a relatively simple procedure in the shallow-water system, but it is possible to extrapolate this method to a multi-layer environment, [12, 17].

The standard semi-Lagrangian scheme must interpolate the PV field at each time step, in turn leading to diffusive advection [16]. The lack of this diffusive advection within the CASL method leads to an improvement in the representation of the PV field from the increased ability to handle sharp PV gradients, [16]. The use of contour-advection in this manner allows us to include small-scale structures not visible in the grid generated representation of the field, without compromising the efficiency of the algorithm.

2.2.1 Contour to grid conversion

A crucial step in the speed of the CASL algorithm is the use of the fastest possible method in converting the fine-scale Lagrangian PV field into a coarser Eulerian representation, [13]. Given n nodes on the PV contours, this should therefore cost $\mathcal{O}(n)$ operations.

In spherical geometry the domain is only periodic in longitude, however much of the original doubly-periodic algorithm was able to be carried over, due to the use of equally spaced grid points in latitude and longitude, [9]. The routine must first determine which (if any) longitudes are crossed by adjacent nodes, $\mathbf{x}_i$ and $\mathbf{x}_{i+1}$ say,

of a PV contour. This section of contour is an arc, due to the inherently curved surface on which the contours lie. The range of longitudes where this crossing occurs is given by the difference in longitudes, λ_{i+1} and λ_i, where

$$\lambda_i = \tan^{-1}\left(\frac{y_i}{x_i}\right) ,$$

[9]. Using the (integer) values of

$$\frac{\lambda_{i+1}+\pi}{\Delta\lambda_f} \quad \text{and} \quad \frac{\lambda_i+\pi}{\Delta\lambda_f} , \tag{2.1}$$

where $\Delta\lambda_f = \Delta\lambda/m_g$ is the fine-grid longitude spacing, the indices for each longitudinal crossing is found. For the fine-grid, m_g is normally taken to make this grid four times finer and the resulting 'inversion' grid is then used to convert the PV contours to gridded values. This preserves some of the fine-scale circulation, [13]. Similarly, we have $\Delta\phi_f = \Delta\phi/m_g$, where $m_g = 4$.

For each λ, the latitude, ϕ is determined from the requirement that for a crossing point $\mathbf{x}$,

$$\mathbf{x} = (r\cos\lambda, r\sin\lambda, z) , \tag{2.2}$$

where $r = \cos\phi$ and $z = \sin\phi$, lies on the same arc, i.e.

$$\mathbf{x}\cdot(\mathbf{x}_i \times \mathbf{x}_{i+1}) = 0 . \tag{2.3}$$

With $\mathbf{a}_i = (a_i, b_i, c_i) = \mathbf{x}_i \times \mathbf{x}_{i+1}$, we have

$$\frac{z}{r} = \tan\phi = -\frac{a_i\cos\lambda + b_i\sin\lambda}{c_i} . \tag{2.4}$$

The index of the latitude is then given by the integer value of $(\phi+\pi/2)/\Delta\phi_f$, cf. equation (2.1).

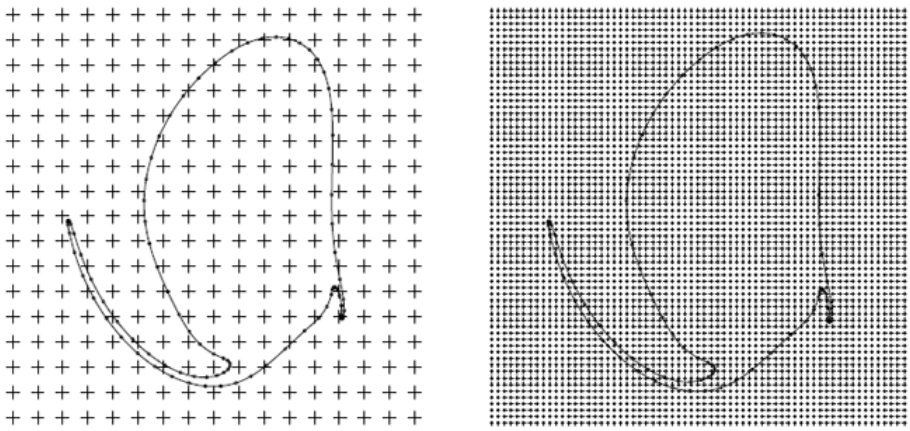

FIGURE 2.2: PV grid schematic showing the velocity inversion grid (left) and the PV conversion grid (right) — demonstrating the fine scale detail able to be resolved in the PV field.

Given the direction and magnitude of the PV jump across the contour (denoted Δq), an array of PV jumps is then built up for the grid points. Finally, the PV field, to within an overall constant, is obtained by summing these jumps, from the south pole to the north pole. This constant is fixed by the requirement that the global average vorticity $\zeta = 0$. This follows since $\zeta = \boldsymbol{\nabla}^2\psi$ and the integral of a Laplacian is zero over the sphere, [8–10].

It is then economical to average this fine-grid PV field back to the inversion grid, [13]. Each iteration of this step therefore doubles the grid scale, halving the number of grid points in each direction using a standard nine-point area-weighted average of the grid points surrounding (and including) the target grid point. Surprisingly, this averaging loses little accuracy, preserving the most important characteristics of the PV field, [13]. This step exploits the fact that the details of the fine-scale PV do not matter for computing the velocity, but rather only their gross characteristics matter[1]. The CASL model then calculates the velocity field from this 'coarse grained' PV field, together with $\tilde{h}$ and δ.

[1]This is justified by observations that velocity spectra decay with decreasing scale, [27, 28, 76]. In addition, the decay in velocity is faster than that for the PV field in this case.

2.2.2 Contour surgery

Since there is no lateral PV diffusion implemented in the CASL method in order to maintain stability, the sub-grid scale processes must be dealt with explicitly to avoid a cascade to small-scale structure. The requirement to control the complexity of the contours during their evolution is achieved using a method termed "Contour Surgery".

Developed in 1988 by D. Dritschel and outlined in [8, 10], this procedure removes filamentary structure on the contours, below a given scale, δ, where $\delta = \frac{1}{4}\mu^2 L$. Here L is the pre-set characteristic length-scale of the PV distribution and μL is approximately equal to the maximum spacing between adjacent nodes on a contour. In order to determine this scale, work originally done in [76] found it appropriate to retain fine-scale PV structure up to ten times finer than the smallest scale of the advecting field. As such, the surgical scale is typically taken as $\delta = \Delta\phi/10$, where $\Delta\phi$ is the latitude grid spacing, [17].

The surgical process involves searching for nodes that are sufficiently close together, which could be a costly procedure where the number of nodes is large and surgery is called every other time step. In order to minimise the cost of implementing this step, the contours are pre-sorted in order of PV level and since only contours on the same level may possibly reconnect, each level is treated separately, where appropriate. Furthermore, a point by point search of a pair of contours is only made if they could potentially be close enough.

Surgery is a very impressive technique, alleviating the requirement (in the improved CASL algorithms) for hyperviscosity (or for hyperdiffusion), commonly used in atmosphere and ocean dynamic modelling — see Chapter 2.4.3 for further discussion on diffusion. In addition, since the surgical scale is typically a tenth

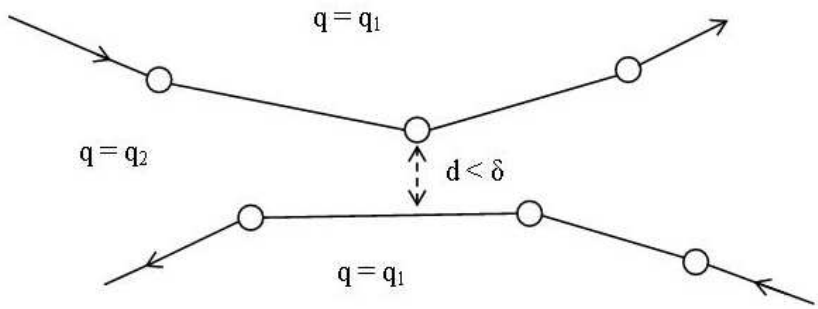

FIGURE 2.3: Contour Surgery, fundamental to the CASL model. With two PV contours separated by a preset value, δ, or less will be subject to surgery shown in figures (2.4) to (2.6).

that of the (inversion) grid scale (and perhaps below, see [48, 76]), it can be expected that the features and structure found in the CASL method are typically reliable down to the grid scale and somewhat beyond, a quality not shared by conventional grid-based models.

The complete surgery procedure thus reconnects contour nodes on the same level (or nodes on the same contour) when they get closer than a prescribed distance δ. An example is given for two PV contours closer than δ in figure (2.3). The contour surgery procedure then recalculates the relevant nodes (figure (2.4)) and the contours are then reconnected to these new nodes (figure (2.5)).

Following the surgical procedure, nodes on each PV contour are redistributed to compensate for increased (or decreased) curvature and length, [8, 10, 13], shown in figure (2.6). The mean curvature between nodes i and $i+1$, denoted κ_i, is given for each i by the cubic-spline interpolation routine, [8, 10]. From this, a modified value is calculated from

$$\tilde{\kappa}_i = \sqrt{\kappa_i^2 + 1/L^2}$$

in order to keep the node spacing greater than μL (here L is a prescribed large-scale length of the flow). With $\mathbf{x}$ the position of a fluid element, the distance $d_i \equiv |\mathbf{x}_{i+1} - \mathbf{x}_i|$ and a weight $w = d_i/(d_i^2 + 4\delta^2)$ is calculated to obtain an intermediate

averaged curvature, namely

$$\check{\kappa}_i = \frac{w_{i-1}\tilde{\kappa}_{i-1} + w_i\tilde{\kappa}_i}{w_{i-1} + w_i}\,,$$

itself averaged with the value at node $i+1$ to give the final curvature over four nodes, $\bar{\kappa}_i$. The number of nodes used per unit length for the contour is then re-calculated by

$$\frac{(\bar{\kappa}_i L)^{1/2}}{\mu L} + \bar{\kappa}_i \quad \text{or} \quad \frac{2}{\delta}\,, \tag{2.5}$$

whichever is smaller.

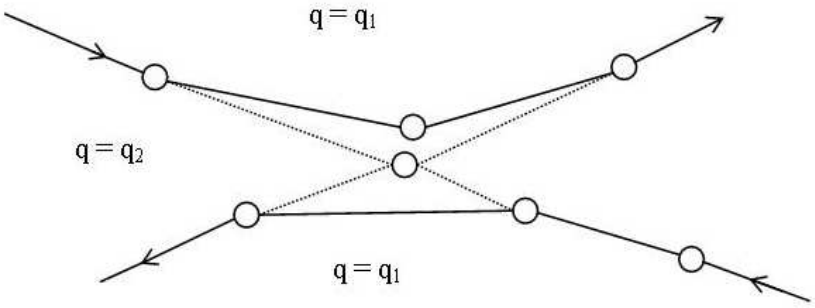

FIGURE 2.4: Midpoint node is calculated

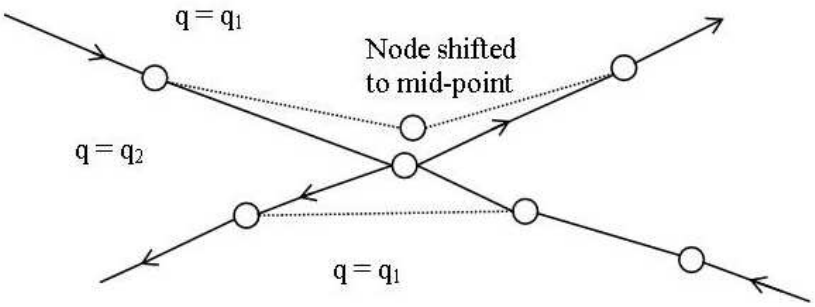

FIGURE 2.5: Node is shifted to the calculated midpoint

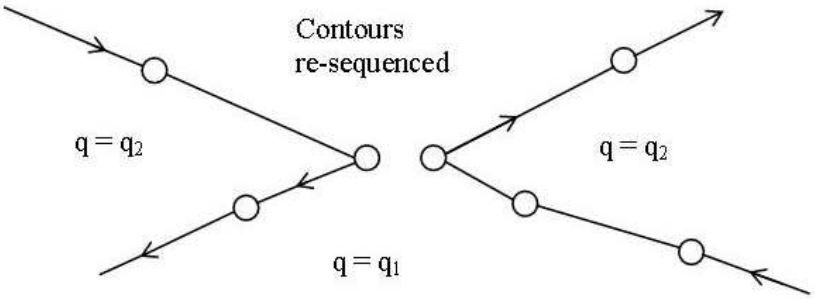

FIGURE 2.6: PV contours are then re-sequenced.

2.3 Time-stepping

The height and divergence fields are already represented in an Eulerian manner and these are discretised and time-stepped using a pseudo-spectral scheme, mentioned in Chapter 2.1 and discussed in Chapter 2.4.1, where all spatial derivatives are computed in spectral space and all product terms are computed in physical space.

There are a number of methods used to integrate the SWEs in time. The most

popular are variations on the Runge-Kutta method, the Adams Bashforth and the leap-frog scheme, for example [19] and others. The semi-implicit leap-frog procedure, [63], used in the CASL algorithm is also widely utilised in spectral models. In this procedure time derivatives are centred, i.e.

$$\frac{\partial \delta}{\partial t} \approx \frac{\delta^{n+1} - \delta^{n-1}}{2\Delta t}\,, \tag{2.6}$$

and all linear terms appearing on the left hand sides of equations (1.25) and (1.26) are averaged over time levels, i.e.

$$\delta \rightarrow \frac{\delta^{n+1} + \delta^{n-1}}{2}\,.$$

The result for equations (1.25) and (1.26) is

$$\frac{\delta^{n+1} - \delta^{n-1}}{2\Delta t} + c^2\mathcal{H}\left(\frac{\tilde{h}^{n+1} + \tilde{h}^{n-1}}{2}\right) = S_\delta\,, \tag{2.7}$$

$$\frac{\tilde{h}^{n+1} - \tilde{h}^{n-1}}{2\Delta t} + \frac{\delta^{n+1} + \delta^{n-1}}{2} = S_h\,, \tag{2.8}$$

where S_δ and S_h are the right hand sides of equations (1.25) and (1.26), respectively, and $\mathcal{H}$ is the Helmholtz operator introduced in equation (1.27).

Letting $\bar{\delta} = (\delta^{n+1} + \delta^{n-1})/2$ and $\bar{h} = (\tilde{h}^{n+1} + \tilde{h}^{n-1})/2$, we can rewrite for example

$$\frac{\delta^{n+1} - \delta^{n-1}}{2\Delta t} = \frac{\bar{\delta} - \delta^{n-1}}{\Delta t}\,. \tag{2.9}$$

Then, with $S'_\delta = S_\delta + \delta^{n-1}/\Delta t$ and $S'_h = S_h + \tilde{h}^{n-1}/\Delta t$, the above discrete equations reduce to

$$\frac{\bar{\delta}}{\Delta t} + c^2\mathcal{H}\bar{h} = S'_\delta\,, \tag{2.10}$$

$$\frac{\bar{h}}{\Delta t} + \bar{\delta} = S'_h \tag{2.11}$$

and substituting $\bar{\delta}$ from equation (2.10) into (2.11) gives (after some rearranging),

$$\left[c^2\mathcal{H} - \frac{1}{\Delta t^2}\right]\bar{h} = S'_\delta - \frac{S'_h}{\Delta t}\,. \tag{2.12}$$

Finally, one can recover the next time-step from $\bar{\delta} = S'_h - \bar{h}/\Delta t$ and

$$\begin{aligned}\tilde{h}^{n+1} &= 2\bar{h} - \tilde{h}^{n-1}\,,\\ \delta^{n+1} &= 2\bar{\delta} - \delta^{n-1}\,.\end{aligned}$$

This time-stepping method is used due to the fact it is unconditionally stable for the linearised equations [63].

At each time-step the PV contours are updated by contour advection, using a standard 3^{rd}-order Adams-Bashforth scheme, while $\tilde{h}$ and δ are updated by the above semi-implicit leap-frog method. In order to maintain synchrony of even and odd time levels, a standard Robert-Asselin filter, [1, 58], is also applied to the prognostic variables, that is, the field δ at time t is replaced by a combination of the field at $t - \Delta t$, t and $t + \Delta t$. i.e. , from [16],

$$\delta^n \leftarrow \delta^n + A\left[\delta^{n+1} - 2\delta^n + \delta^{n-1}\right]\,, \tag{2.13}$$

which effectively damps high-frequency modes. By choosing a small coefficient, A, we can damp small-scale, high-frequency, artificial gravity waves, as discussed in [64].

2.4 Benefits of the CASL method

The CASL model is not restricted to the shallow-water case, indeed CASL was developed first for quasi-geostrophic (QG) flow in [13] and has since been widely

extended to the more complete ageostrophic systems governing the dynamics seen in the atmosphere and ocean, [15, 46, 47, 71]. For a more general system, the vertical structure of the fluid is also prescribed, and PV is advected on density or potential temperature surfaces, [38].

The most common methods for solving the SWEs are the pseudo-spectral (PS) and semi-Lagrangian (SL) methods. In each case, the divergence and mass equations are solved in the same way, outlined above for the CASL method. The differences between the three methods lie in the solution of the vorticity equation, as follows.

2.4.1 The pseudo-spectral method

In this method, equation (1.10) is replaced with

$$\frac{\partial \zeta}{\partial t} + \boldsymbol{\nabla} \cdot ((\zeta + f)\mathbf{u}) = -\nu(-\boldsymbol{\nabla}^2)^n \zeta \,. \tag{2.14}$$

The term on the right is known as "hyperdiffusion" and is required by the PS method for numerical stability, [43]. The coefficients, ν and $n > 1$, are generally chosen such that the smallest features (those comparable to the grid-scale) are effectively dissipated.

2.4.2 The semi-Lagrangian method

As the name suggests, the CASL method is based on the SL scheme, using the principal of PV conservation as *the* central property of the SWEs. For this case, we have of course that the prognostic variable ζ is replaced with q and we have material conservation, equation (1.22). The SL method solves this conservation via trajectory integration,

$$\frac{d\mathbf{x}}{dt} = \mathbf{u}(\mathbf{x}, t) \,, \tag{2.15}$$

since q does not change following the fluid element. Therefore, to determine q at $t + \Delta t$, two steps are required. First, given the arrival point at $t + \Delta t$ of a fluid element (necessarily a grid point), $\mathbf{x}_a$, equation (2.15) must be integrated backward in time in order to determine the departure point, $\mathbf{x}_d$, at time t. Then, since $\mathbf{x}_d$ does not typically land on a grid-point, q must be interpolated at $\mathbf{x}_d$ and time t, hence giving the value of q at $\mathbf{x}_a$ and at time $t+\Delta t$ due to PV conservation.

For further details of the SL method, see references [3, 32, 57, 65], outlining the schemes used and applying specific methods to forecast models.

2.4.3 Where CASL differs

The major difference between the SL and CASL methods is that the SL method interpolates q from a grid at each time step, effectively introducing diffusion, [32]. This diffusion tends to be greater than that introduced for hyper-viscosity in the PS method, [16]. The SL scheme abandons the Lagrangian PV description at every time-step, thereby losing control of conservation.

Using contour-advection and PV, in comparisons with the PS and SL methods, the CASL method has already shown an improvement in accuracy in a variety of contexts, [14, 16]. Furthermore, by implementing a spectral FFT method in longitude and second-order centred finite differencing in latitude, costly Legendre transforms, required in a PS method in latitude, are avoided. Because of this, the CASL method has been shown to be extremely cost effective with respect to computational power. Not only has it been proved that the spectral method's accuracy is *no greater than* that of finite differencing for complex PV fields, [61], but at any given accuracy, contour-advection is 10 to 100 times faster than these other numerical methods in shallow-water simulations, [16].

The CASL method controls the cascade of PV to smaller scales through contour surgery, and therefore diffusion is virtually eliminated. For grid-based models, this diffusion is critical in order to stop the buildup of artificial structures at the grid scale. At lower resolutions, whilst all models suffer from a poor estimation of the advecting velocity field, the PS and SL methods incur further accuracy degradation through excessive diffusion.

As will be discussed further, the CASL scheme used does not omit gravity waves, and is therefore not a 'balanced model'. However, importantly, the latest version of the algorithm has been shown to recover the underlying balance expected, [51, 61]. This shows a great improvement in numerical accuracy and an almost complete elimination of erroneous gravity waves within the system.

Much of this thesis will focus on gravity waves appearing in the SWE system and their potential impact in weather forecasting, climate and ocean models. Gravity waves force the use of a small time-step, which severely undermines model efficiency. General circulation models with large time-steps often have artificially damped gravity waves, since short wavelength gravity waves are considered noise in the numerical system. This method for controlling gravity waves will be challenged in Chapter 4.

Chapter 3

Initial testing

3.1 Introduction

In this section the core routines within the CASL algorithm are tested for their accuracy in a series of calculations. The main aspects of the algorithm include the representation of the underlying grid, the contour representation of PV and the inversion procedure used to determine the advecting velocity field from the PV. The algorithm, introduced in Chapters 1 and 2, uses the prognostic variables of PV, depth and divergence $(q, \tilde{h}, \delta)$, and throughout this algorithm shall be referred to as "CA_0".

Since PV advection typically dominates shallow-water flow, we first verify the methods for calculating the velocity are accurate. This can be demonstrated with two examples, where the exact velocities are known.

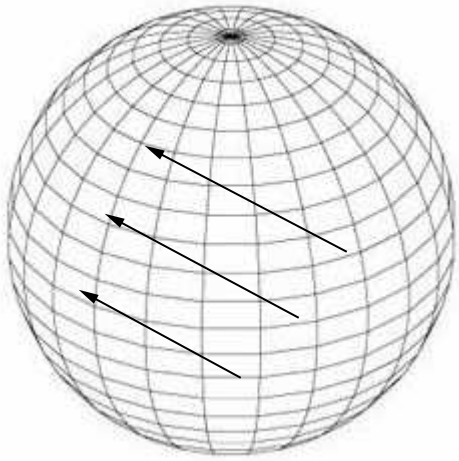

FIGURE 3.1: Rigid body rotation on the sphere about an arbitrary axis.

3.1.1 Rigid rotation

First consider a simple barotropic rigid rotation about a defined axis (specified by the angles $\phi = \phi_c$ and $\lambda = \lambda_c$) in order to confirm the accuracy of the tridiagonal solver routine and finite differencing. Here we have $q = f$ around the axis of rotation, shown in figure (3.1), centred at (ϕ_c, λ_c). The longitudinal and latitudinal velocity components are computed via inverse FFTs of the streamfunction's spectral transform and centred finite differencing.

These computed velocity components were compared to the exact velocities (computed within the test algorithm, given (ϕ_c, λ_c)) and the root mean squared (RMS) errors were calculated in the usual manner. This very simple test case confirmed that, for a very simple flow, the tridiagonal solver routine has the desired accuracy, $\mathcal{O}(n^{-2})$, with increasing number of (latitudinal and longitudinal) grid points (resolution, n) leading to a squared reduction in error (trivial, not shown).

3.1.2 Single PV patch

Next, we consider a variation on the previous case, namely a single circular vortex, placed at varying latitudes on the sphere. The vortex is represented by a patch of uniform PV. There will therefore be a jump, or discontinuity, around the edge of the vortex where the value of PV changes. Whilst this may seem a trivial example, in fact, the discontinuity in PV at the edge of the vortex makes this test more challenging than one might expect. It is also an important example to document, as these sharp PV gradients are often seen in the atmosphere and oceans, [76].

The calculations for this test case are carried out using the barotropic limit of the SWEs, obtained by setting $\delta = 0$ and $h = 1$ in equations (1.10) to (1.12), corresponding to incompressible flow. The PV, from equation (1.23), then simplifies to the absolute vertical vorticity

$$q = \zeta + f \,, \tag{3.1}$$

and remains conserved, i.e.

$$\frac{\mathrm{D}q}{\mathrm{D}t} = 0 \,.$$

Since $\delta = 0$, then (from equation (1.16)) $\chi = 0$ and hence we need only invert

$$\boldsymbol{\nabla}^2 \psi = \zeta \,,$$

or, from equation (3.1),

$$\boldsymbol{\nabla}^2 \psi = q - f \tag{3.2}$$

to find u and v.

A specific section of code was therefore written in which the vortex points are converted to spherical coordinates and the centre of the PV patch rotated, such that it lies over the pole. To do this, the central latitude ϕ_c and longitude λ_c are

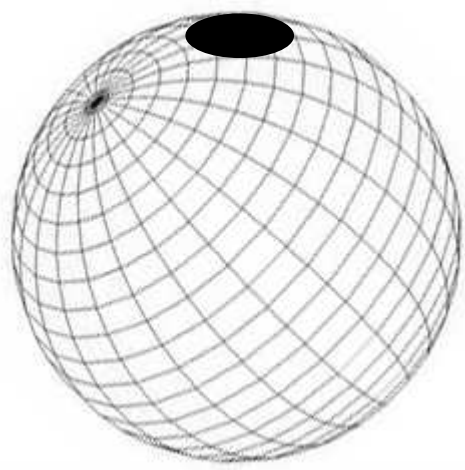

FIGURE 3.2: PV patch on rotated sphere.

given, defining the axis of symmetry for the patch:

$$\begin{aligned} x_c &= \cos\phi_c \cos\lambda_c \,, \\ y_c &= \cos\phi_c \sin\lambda_c \,, \\ z_c &= \sin\phi_c \,. \end{aligned}$$

In this test case, $\lambda_c = 0$ and so, only the latitude of the vortex was changed. Then the PV field corresponding to rigid rotation within the patch was set up, using equation (3.1), around a rotated z coordinate

$$z_r = x_c \cos\phi \cos\lambda + y_c \cos\phi \sin\lambda + z_c \sin\phi \,, \tag{3.3}$$

with ψ, from equation (3.2), computed for inversion (here, $\cos\phi$ provides a natural area weight required for the nine-point averaging of the PV field).

From the inversion procedure, the velocities are calculated both along and perpendicular to the contour. The root mean squared (RMS) errors are then obtained in the usual manner, by comparing the velocity field from numerical inversion to

the exact velocities in a coordinate system in which the centre of the vortex lies at the North pole, see figure (3.2). This presents a more interesting test case to further study the effects of resolution on the accuracy of CA_0.

3.2 A closer look at inversion and grid resolution

As discussed, PV inversion uses fast Fourier transforms (FFTs) in longitude and second-order finite differencing in latitude to calculate the velocities at each node on each contour. The RMS errors for velocities perpendicular and tangential to the contour were calculated for patches of radius 10° with $\phi_c = 0°, 10°, ..., 90°$ and $\lambda_c = 0°$. RMS errors in the velocity perpendicular to the contour are expected to be small as there is no perpendicular component in the exact velocity.

For any numerical method, increasing the resolution should lead to a decrease in errors, from which the efficiency and accuracy of the algorithm can be deduced. Increasing the number of grid points used on the sphere gave the expected results (not shown) — the perpendicular velocity RMS error at the contour decreases as $\mathcal{O}\left(n_\phi^{-2}\right)$. This shows that the inversion routine, based on second-order differencing in ϕ, was giving the expected level of accuracy.

A common grid for spherical spectral models takes the number of points in latitude to be half the number of points in longitude, i.e. $n_\phi = n_\lambda/2$. Here though we use a semi-spectral approach with second-order finite differencing in latitude and Fourier series in longitude. Extra resolution is used in latitude to compensate for the higher errors expected in finite differencing compared to Fourier (Legendre) series. Since the tridiagonal solver implemented is much more efficient than FFTs, it makes sense to increase the number of latitudinal grid points used (cyclic reduction method). The RMS errors produced for $n_\phi = n_\lambda/2$ are compared for those

	$n_\phi = n_\lambda/2$	$n_\phi = n_\lambda$
RMS Error Tangential Velocity	2.36×10^{-2}	2.07×10^{-2}
RMS Error Perpendicular Velocity	1.34×10^{-3}	5.62×10^{-4}
RMS Error Zonal Velocity	2.18×10^{-3}	6.59×10^{-4}
RMS Error Meridional Velocity	8.63×10^{-4}	8.05×10^{-4}

TABLE 3.1: RMS errors for the velocity components given, comparing ratios used for the number of grid points, n_λ and n_ϕ.

with equal grid points, $n_\lambda = n_\phi$, in table (3.1) for $\phi_c = 45°$. This simple amendment leads to significant improvements, except for the tangential and meridional velocities, as discussed below.

3.2.1 Further resolution tests

The baseline resolution in the CASL model is a 128×128 latitude/longitude grid, with a grid four times finer in each direction used in converting the contour representation of PV to gridded values — refer back to figure (2.2) for an example of this grid ratio. Changing the PV conversion to velocity grid scale ratio showed little improvement beyond four.

To quantify the error on this anisotropic grid, a 10° radius vortex, placed at 0° longitude, with centre varying in 10° increments between 0° and 90° latitude, was examined. The results for $128^2, 256^2$ and 512^2 resolutions are shown in figures (3.3) and (3.4). These follow a clear trend, with the RMS errors for perpendicular, zonal and meridional velocities decreasing like n_λ^{-2} and RMS errors for the tangential velocity decreasing like n_λ^{-1} with increasing resolution.

The error in tangential velocity is perhaps unexpected. However, the tangential velocity of the exact solution exhibits a point jet (or wedge) profile, with a discontinuity in its derivative. The numerical rounding off of the jet maximum always produces an error of $\mathcal{O}(n_\lambda^{-1})$, irrespective of the numerical inversion method used,

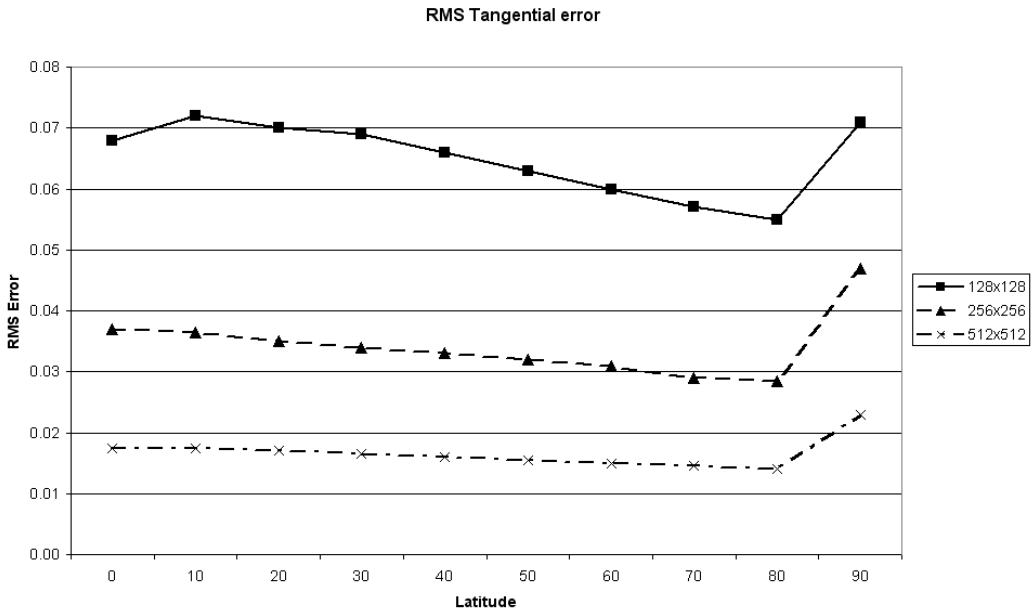

FIGURE 3.3: RMS error for tangential velocity

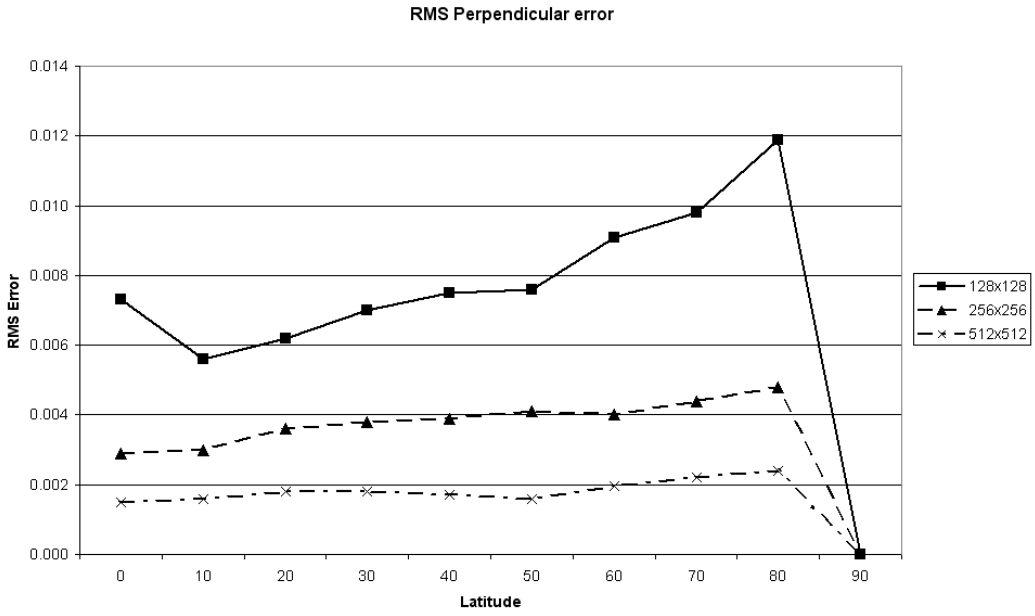

FIGURE 3.4: RMS error for perpendicular velocity

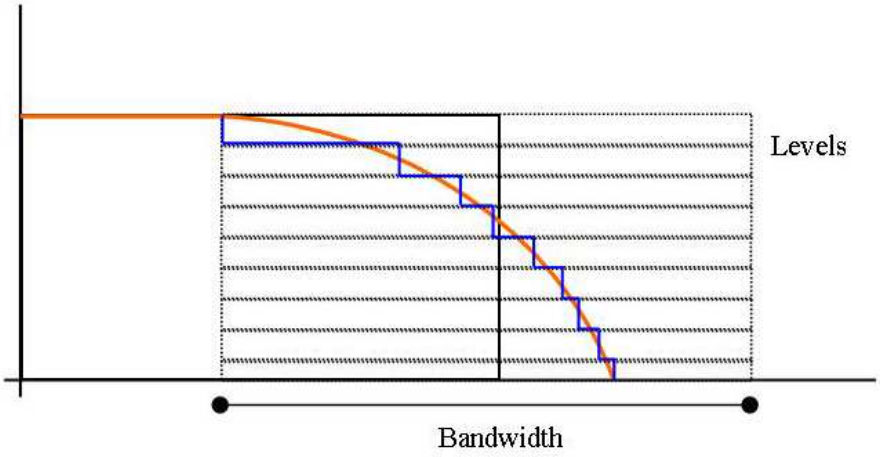

FIGURE 3.5: Approximation of the idea of using a stepped vortex edge (blue line) to create a smoother appearance of PV (red line).

[13]. On the other hand, the tangential velocity does not influence the shape of a contour, and is not important in practise.

3.3 A smoother approach

The test programme was adapted to smooth the vortex edge and compare the results to the previous section. In order to do this simply, layers were introduced over a finite bandwidth — see figure (3.5) for an idea of how this layered vortex edge is set up in comparison to the step in PV at the vortex edge (black line in figure).

Instead of a single jump in PV, there is now a series of small jumps. This gives the edge a smoother appearance and should minimise the tangential velocity errors produced by a large jump in PV across the vortex edge. This was tested by placing the vortex centre at latitudes 10°, 45° and 80° with $2, 4, 6, 8, 10, 15$ and 20 PV levels, and bandwidths of $0°, 1°, 5°$ and 10°. All these permutations were considered, with the results summarised in figures (3.6) to (3.8) for a vortex patch placed at 10° latitude (the other results are similar). The RMS errors for each

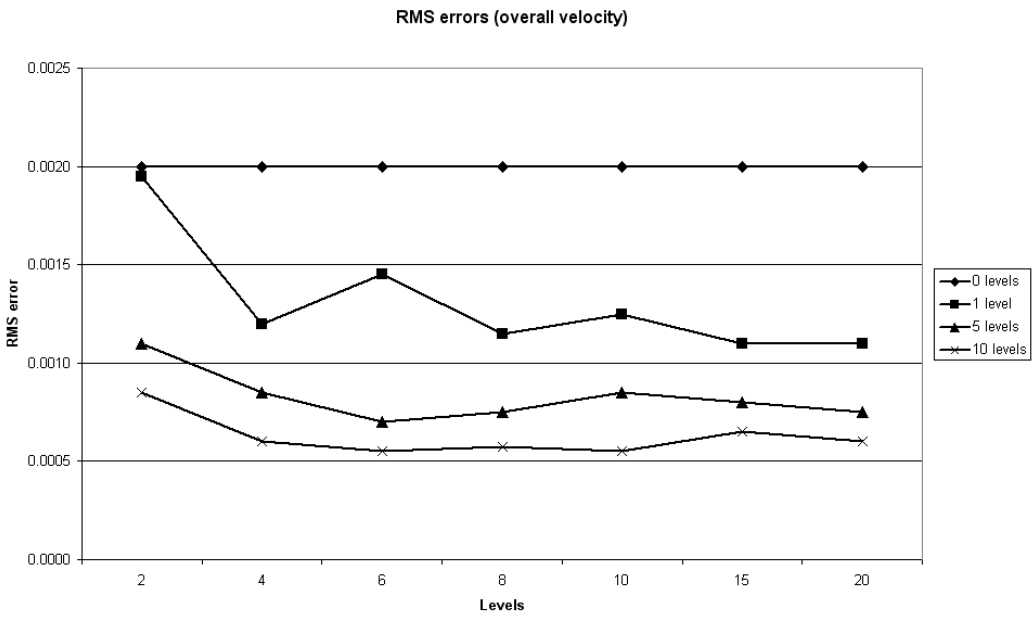

FIGURE 3.6: Vortex patch bandwidth results, showing the RMS errors for the overall RMS velocity error. Shown are bandwidths 0 (diamond markers, where appropriate), 1 (square markers), 5 (triangular markers) and 10 (cross markers), used on a patch placed at 10° latitude and the number of levels shown along the x-axis.

part of the velocity field (overall, as well as inside and outside the patch) and for u and v are plotted against the number of levels at 128^2 resolution.

We can see that the error reduces and flattens out on increasing the number of levels in the vortex edge. Results also indicate that there is little further gain in accuracy upon taking more than 10 levels and a bandwidth greater than 10°, at this resolution. Notably, now doubling resolution leads to a four-fold reduction in all errors, showing that one can recover the $\mathcal{O}(n_\lambda^{-2})$ behaviour of second-order finite differencing with smooth PV distributions. In conclusion, we have found that sharp variations in PV limit the order of accuracy for any form of PV inversion on a grid.

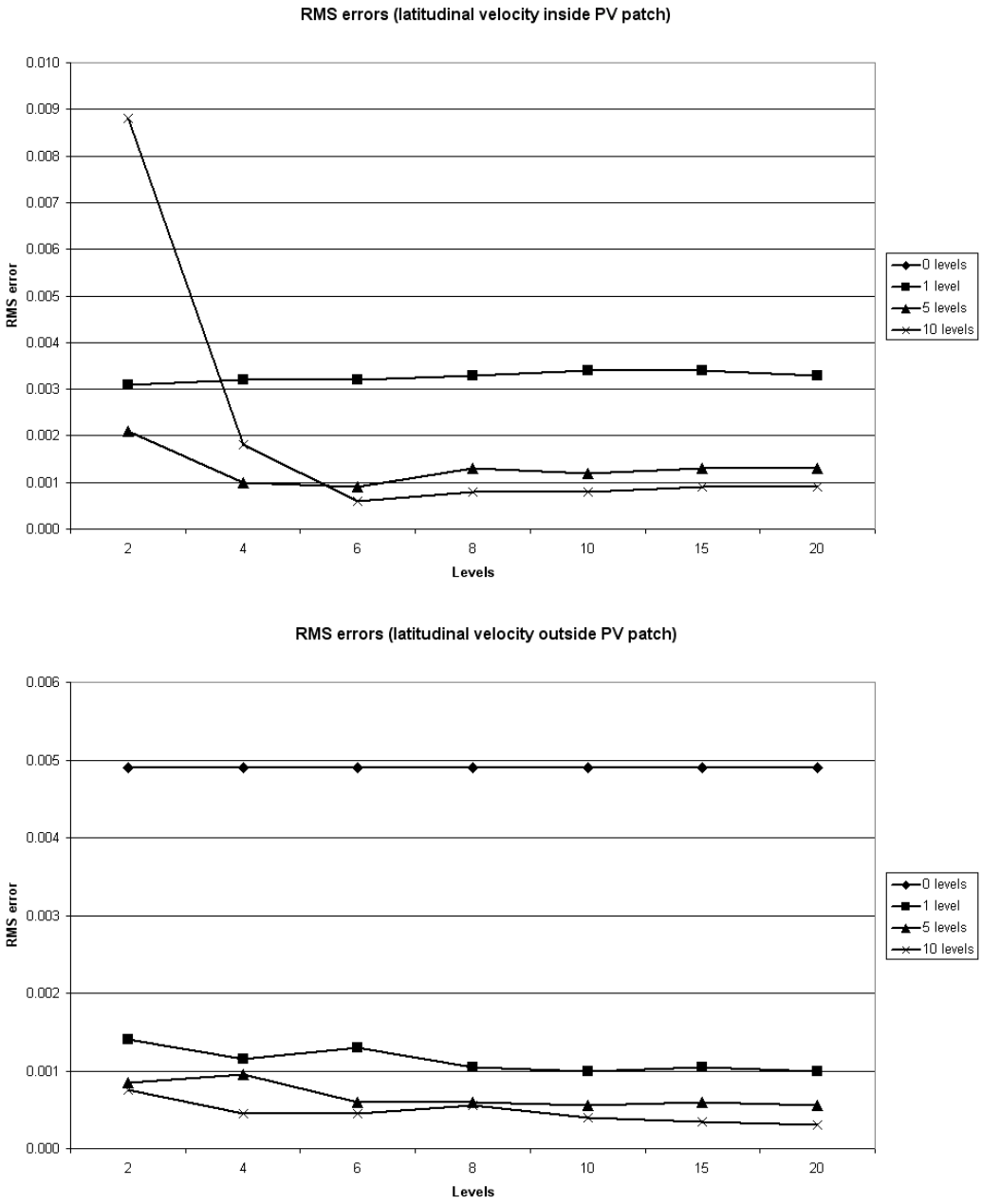

FIGURE 3.7: Vortex patch bandwidth results, showing the RMS errors for velocities inside (top graph) and outside (bottom graph) the patch along the latitudinal direction. Shown are bandwidths 0 (diamond markers, where appropriate), 1 (square markers), 5 (triangular markers) and 10 (cross markers), used on a patch placed at 10° latitude and the number of levels shown along the x-axis.

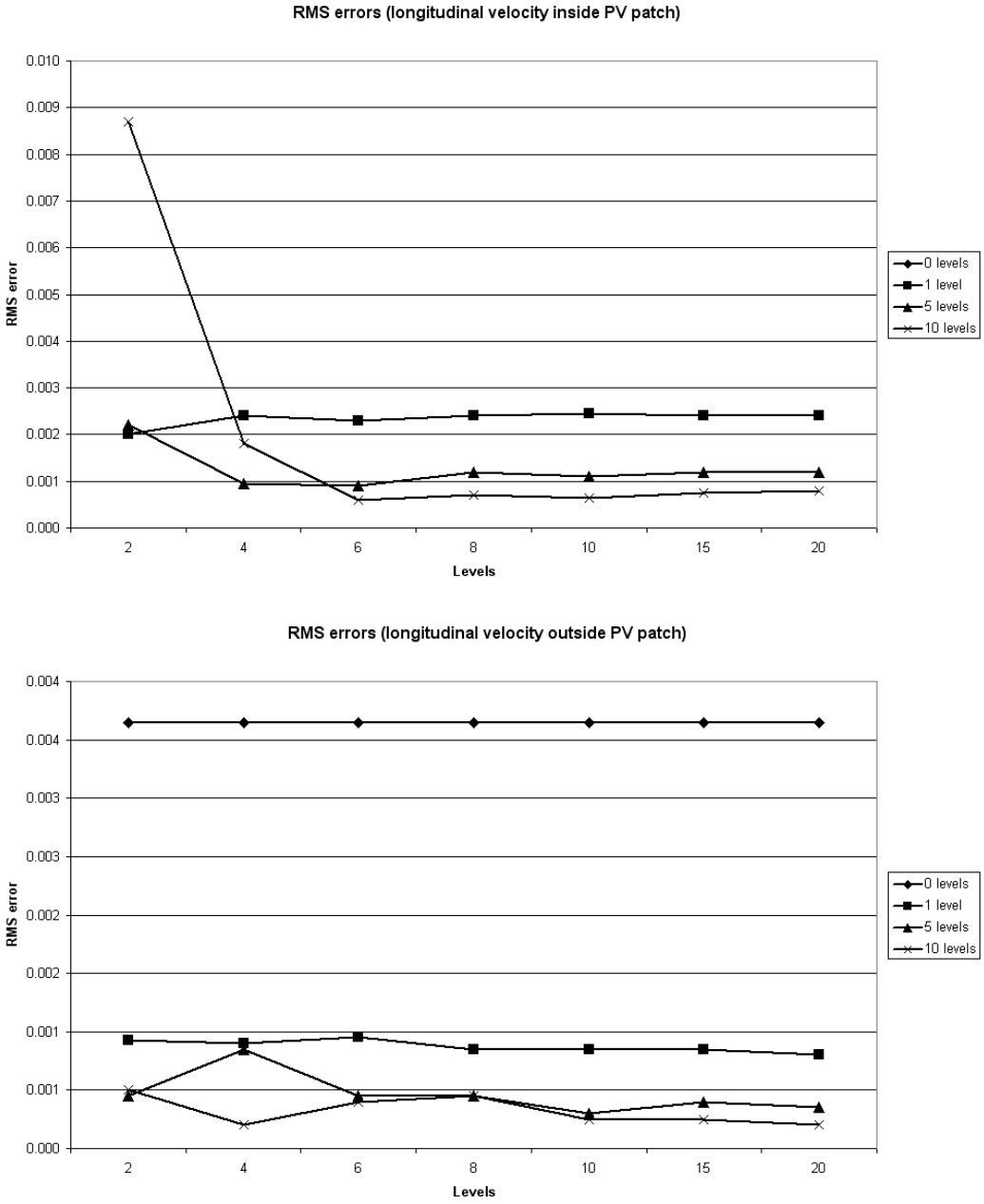

FIGURE 3.8: Vortex patch bandwidth results, showing the RMS errors for velocities along the longitudinal direction. Shown are bandwidths 0 (diamond markers, where appropriate), 1 (square markers), 5 (triangular markers) and 10 (cross markers), used on a patch placed at 10° latitude and the number of levels shown along the x-axis.

Chapter 4

Rossby-Haurwitz waves

4.1 Introduction to Rossby waves

To further test the CASL model, we shall now re-examine a basic test case used for spherical shallow-water numerical models[1], and underscore the need for accurate, high resolution models of atmospheric and ocean dynamics. The Rossby-Haurwitz test case, first proposed by Williamson *et al.* [77], has been examined using a wide variety of shallow-water models in previous papers. Here, two Contour-Advective Semi-Lagrangian (CASL) models are considered, and results are compared with previous test results. We go further by modifying this test case in a simple way to initiate a rapid breakdown of the basic wave state. This breakdown is accompanied by the formation of sharp potential vorticity gradients (fronts), placing far greater demands on the numerics than the original test case does. We also examine other dynamical fields, besides the height and potential vorticity, to assess how well the models deal with gravity waves. Such waves are sensitive to the presence,

[1]The following two chapters have been reproduced from a paper by R. K. Smith & D. Dritschel, JCP September 2006, cited [64]. Some points, such as specific CASL methods, will have been touched on previously. However, for continuity within these chapters I have chosen not to remove minor duplications.

or not, of sharp potential vorticity gradients, as well as to numerical parameter settings. In particular, large time steps (convenient for semi-Lagrangian schemes) can seriously affect gravity waves, but can also have an adverse impact on the primary fields of height and velocity. These problems are exacerbated by a poor resolution of potential vorticity gradients.

4.2 Outlining the Rossby-Haurwitz wave test

Rossby-Haurwitz waves are steadily propagating solutions of the fully nonlinear non-divergent barotropic vorticity equation on the sphere, [35]. This case is useful for testing numerical models as it can be described exactly by analytic formulae and, although the SWEs do not have analytic solutions, a Rossby-Haurwitz initial condition is expected to evolve nearly steadily. This motivated Williamson *et al.* to propose Rossby-Haurwitz waves as one of seven standard test cases in [77].

In the following, as in all previous tests on this case, a zonal wavenumber of 4 is used. It was believed that a zonal wavenumber greater than 5 was unstable, [37], but as recently shown by Thuburn & Li in [67], this wavenumber 4 case is actually also weakly unstable and will eventually break down once perturbed. In fact, even truncation errors cause instability.

4.2.1 The numerical method

A previous comparative study (Dritschel, Polvani & Mohebalhojeh 1999, hereafter referenced [16]) demonstrated that explicit PV conservation can greatly improve the accuracy of shallow-water simulations in the f-plane context. Here, we extend this approach to spherical geometry. The CASL model used here, CA_0, replaces equation (1.10) with equation (1.22), thus making the prognostic variables $(q, \delta, \tilde{h})$.

The PV is represented in a fully Lagrangian way as material contours, between which the PV is uniform and across which it jumps by a specified value Δq (see [13] for details). This is the basis of "Contour-Advection". Other variables are held on a grid, and evolved in a conventional way. A common grid for spherical spectral models takes the number of points in latitude to be half the number of points in longitude, i.e. $n_\phi = n_\lambda/2$. Here though we use a semi-spectral approach with second-order finite differencing in latitude and Fourier series in longitude. Extra resolution is used in latitude to compensate for the higher errors expected in finite differencing compared to Fourier (Legendre) series. By experimentation, using $n_\phi = n_\lambda$ was found to be optimal, in terms of representing the velocity field, when balancing accuracy and efficiency for flows having sharp vorticity gradients. Indeed, as mentioned in the CASL method, for a vorticity discontinuity, one may show that the formal accuracy of the spectral approach is no greater than that for second-order finite differences, [61].

Time-stepping of δ and $\tilde{h}$ makes use of the standard semi-implicit leap-frog procedure introduced in the previous chapter, [56], together with the Robert-Asselin filter to ensure stability. After extensive testing, we found that the filter coefficient A can be chosen as small as $c\Delta t/a$, where Δt is the time-step and a is the Earth's mean radius, [61]. For large time-steps, A is limited to 0.2.

Also, whilst not explicit in the basic equations, some kind of numerical diffusion is often added to reduce aliasing errors and filter poorly resolved short-scale (and typically high-frequency) motions. The explicit use of PV in CA_0 permits much weaker diffusion for stability, [16] — much of the difficulty faced by conventional models includes the resolution of sharp gradients of PV (fronts) and small-scale filamentary structures, common features in the atmosphere and oceans. Even in contour advection, it is impossible to keep up with this scale cascade entirely, and thin filaments are removed by 'surgery' ([13] and references therein), here at a

tenth of the latitude spacing of grid points. This however results in much better *material* conservation of PV than is possible in conventional methods (cf. [16]). For the fields δ and $\tilde{h}$, a 'Broutman' spectral filter is applied to their nonlinear tendencies (cf. [17]). This filter is applied in longitude only, and essentially removes all azimuthal variations shorter than two grid lengths at the equator (where the upper third wavenumbers $m > n_\lambda/3$ are strongly damped). The specific form used is $F(m) = \exp[-\alpha(\xi/r)^{10}]$, for $m \geq 2$, where $\xi = (m-2)/(M-2)$, $M = n_\lambda/2$ and α is chosen so that $F(M) = 10^{-14}$. Wavenumbers $m = 0$ and 1 are not damped. Approaching the poles, $r \to 0$, an increasing proportion of wavenumbers are filtered. This is consistent with the decreasing spacing of longitudes. If one omits the $r = \cos\phi$ factor, the filter is not adequate to ensure numerical stability in polar regions.

The above, purely longitudinal filter, is often sufficient for numerical stability. But occasionally numerical noise develops in latitude, and some damping appears to be necessary. Here, this is done by adding latitudinal diffusion to the δ and $\tilde{h}$ tendencies (using the discrete Laplacian operator). Only a very small damping rate of $D = 0.01$ per day was necessary at the equivalent maximum wavenumber in latitude. The results are insensitive to this coefficient, as shown explicitly at the end of this chapter.

4.2.2 The initial flow

A complete description of the test case is given by Williamson *et al.* [77], so only a few key aspects are noted here. The initial velocity is non-divergent ($\delta = 0$) with the streamfunction (in dimensional units) given by

$$\psi = -a^2\omega \sin\phi + a^2 K \cos^R\phi \sin\phi \cos R\lambda\,, \tag{4.1}$$

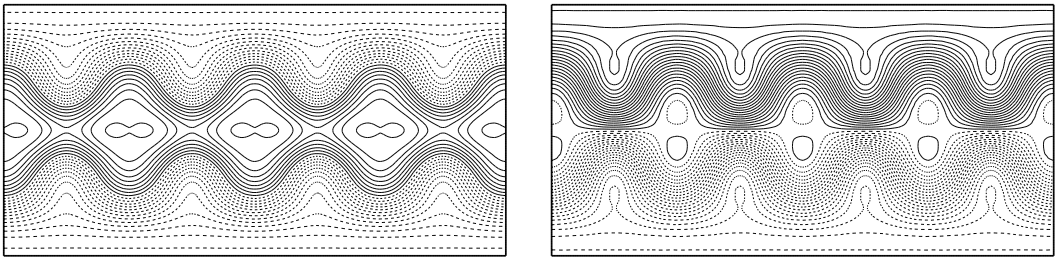

FIGURE 4.1: Initial Rossby-Haurwitz height (left) and PV (right) fields, plotted as a function of longitude $-\pi < \lambda < \pi$ and latitude $-\pi/2 < \phi < \pi/2$. Positive contour levels are solid, while negative ones are dashed. Contour levels displayed are $\pm\Delta/2$, $\pm 3\Delta/2$, etc., where Δ is the contour interval.

where $a = 6.37122 \times 10^6$m, $\omega = K = 7.848 \times 10^{-6} s^{-1}$ and $R = 4$. Haurwitz, [35], showed that the initial height field moved west to east without deviation in a non-divergent barotropic model and that the angular velocity, ν, was given by the relation

$$\nu = \frac{R(3+R)\omega - 2\Omega}{(1+R)(2+R)}\,. \tag{4.2}$$

The velocity components are given by

$$u = a\omega\cos\phi + aK\cos^{R-1}\phi\left(R\sin^2\phi - \cos^2\phi\right)\cos R\lambda\,, \tag{4.3}$$

$$v = -aKR\cos^{R-1}\phi\sin\phi\sin R\lambda\,, \tag{4.4}$$

and vorticity by

$$\zeta = 2\omega\sin\phi - K\sin\phi\cos^R\phi(R^2+3R+2)\cos R\lambda\,. \tag{4.5}$$

The initial height field h is chosen to be "in balance with" the velocity field, by requiring the initial divergence tendency to be zero. The analytical form of h, from [77], is obtained from the streamfunction by the relation

$$gh = gh_0 + a^2\left(A(\phi) + B(\phi)\cos R\lambda + C(\phi)\cos(2R\lambda)\right)\,, \tag{4.6}$$

where

$$
\begin{aligned}
A(\phi) &= \frac{\omega}{2}(2\Omega+\omega)\cos^2\phi + \frac{1}{4}K^2\cos^2\phi[(R+1)\cos^2\phi \\
&\quad +(2R^2-R-2)-2R^2\cos^{-2}\phi]\,, \qquad (4.7)\\
B(\phi) &= \frac{2(\Omega+\omega)K}{(R+1)(R+2)}\cos^R\phi[(R^2+2R+2) \\
&\quad -(R+1)^2\cos^2\phi]\,, \qquad (4.8)\\
C(\phi) &= \frac{1}{4}K^2\cos^{2R}\phi\left[(R+1)\cos^2\phi-(R+2)\right]\,. \qquad (4.9)
\end{aligned}
$$

The minimum fluid height occurs at the poles, where $h_0 = 8000m$, and the mean fluid height is $H = 9523m$. We use a height contour interval of $120m$, and a PV contour interval of $9.3385 \times 10^{-6}s^{-1}$ to compare directly with [67]. The initial height and PV fields are shown in figure (4.1).

Using a variety of numerical parameters, the CA_0 model was run for 40 days. The benchmark case employed a resolution of 128^2, a time-step of $\Delta t = 0.0025$ of a day (a little less than half the Courant-Friedrichs-Lewy (CFL) criterion time-step (where the maximum Courant number, taken to be $c\Delta t/\Delta x$ is below one) $\Delta t_{\mathrm{CFL}} = \Delta\phi/c = 0.0059387$, where $c = \sqrt{gH} = 305.59ms^{-1}$), and a latitudinal damping coefficient of $D = 0.01$. The results at early times (figure (4.2)) closely reproduce those found by [67] using independent models.

4.2.3 Why re-visit this test case?

While this test case has been carried out in many previous studies, attention has been largely focused on the early time evolution of the height field, which exhibits little variation — see figure (4.2). Thuburn & Li (2000) illustrate the PV as well, which is also a simple field at early times (they show day 8). They also take the test case further in time and find that the stability of the Rossby-Haurwitz wave

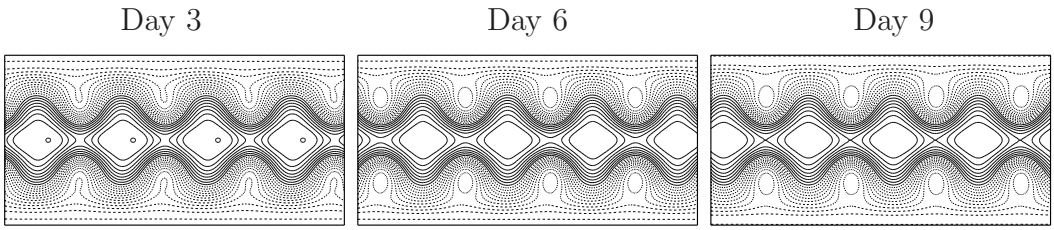

FIGURE 4.2: Height field at days 3, 6 and 9 (left to right): cf. [67].

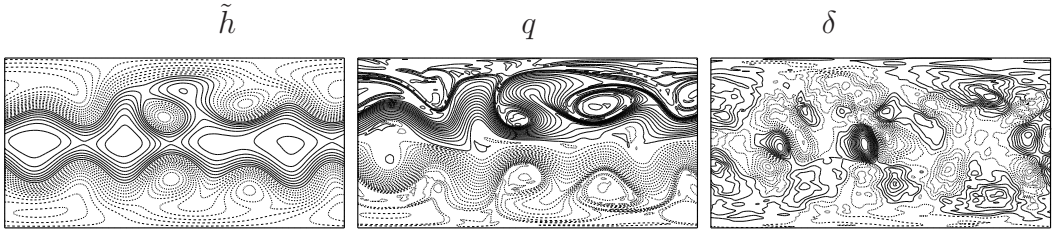

FIGURE 4.3: Height, PV and Divergence fields (left to right) at day 35. The divergence contour interval is 0.001 days^{-1} in this and subsequent figures.

is sensitive to numerical error. In particular, the flow breaks down between 30 and 40 days, depending on numerical parameters and the model employed.

Qualitatively similar behaviour is found when using the CA_0 model. The flow becomes noticeably unstable around day 30. By day 35, the PV and divergence fields have become turbulent, as exhibited in figure (4.3). PV gradients sharpen into virtual discontinuities, fronts, which dominate the subsequent evolution. The divergence field becomes highly structured, only in part from gravity waves (see below). This complex late time behaviour was not anticipated in the design of this test case, but it is in fact more characteristic of realistic atmospheric and oceanic flows than is the simple early time behaviour.

This turbulent flow puts severe demands on the numerics, at least if one tries to maintain accuracy. Numerical parameters, particularly the time-step and the diffusion coefficient, need to be carefully chosen to represent the flow — both the vortical part and the gravity wave part — as accurately as possible while keeping

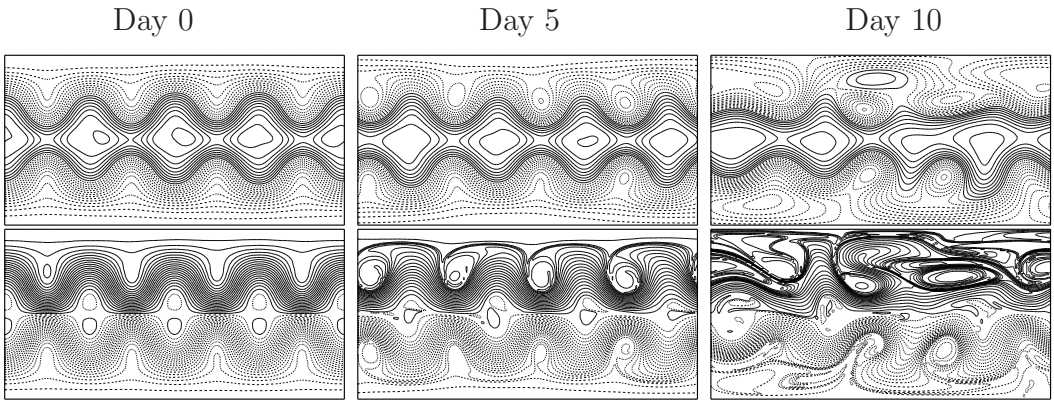

FIGURE 4.4: Perturbed height (top) and PV (bottom) fields at the initial time, then days 5 and 10 (left to right).

numerical stability. This is a balancing act, as both accuracy and stability are flow dependent.

The key point is that the test case must be sufficiently demanding for numerical methods intended for the core of more realistic atmospheric and oceanic models (as advocated by [16]). The test case must also be reproducible, i.e. insensitive to numerical noise. This is not true of any of the test cases proposed by Williamson *et al.* [77]. But the Rossby-Haurwitz test case does suggest a simple modification: we can seed the instability so that at least the early complex stages of the flow are reproducible.

4.3 Modification of the Rossby wave test

A broad-scale small-amplitude disturbance was added to the dimensionless height anomaly $\tilde{h}$ at $t = 0$ to destabilise the flow quickly. The disturbance has the form $(xx_0 + yy_0 + zz_0)/40$, where (x, y, z) are the Cartesian coordinates of a point on the sphere, and (x_0, y_0, z_0) is a specific point located at latitude $\phi = 40°$ and longitude $\lambda = 50°$. Using the benchmark parameter settings (128^2 resolution, $\Delta t \approx 0.43521 \Delta t_{\mathrm{CFL}}$, and a damping coefficient $D = 0.01$), the flow evolution is

shown in figure (4.4). Within just a few days the flow breaks down into a complex assortment of fronts and vortices, most evident in the PV field. The maximum Froude number, $F_r = |\mathbf{u}|/c(1+\tilde{h})^{1/2}$, reaches 0.435 (the time mean is 0.35) and the minimum and maximum Rossby numbers, $R_o = \zeta/2\Omega_E$, reach -0.80 and 0.87. The height field distorts significantly, but remains broad-scale. In particular, there is no visible trace of gravity waves in this field.

4.3.1 Numerical sensitivity

We examine next the sensitivity to the choice of numerical parameters. The effect of resolution is shown in figure (4.5), for the height, divergence and PV fields at day 15 and at resolutions 64^2, 128^2, 256^2, and 512^2. In each case, the time-step is just under half the CFL value (so it varies with resolution), and $D = 0.01$. Rapid convergence with resolution occurs, with minor differences between the highest resolution cases (as found previously in the f-plane context in [16]). The time-averaged r.m.s. height differences between the highest resolution case and the others are 1.71%, 7.41% and 26.0%, for 256^2, 128^2 and 64^2 resolutions respectively (these are percentages of the r.m.s. height anomaly in the highest resolution case). The PV differences are 3.00%, 7.87% and 19.1%. The differences diminish sharply with resolution, most strongly for the smoother height field, as expected. The PV differences are created by advection errors, arising mainly from errors in the velocity field. Numerical convergence is less marked for the divergence field, which exhibits errors of 16.0%, 33.6% and 60.4% (i.e. only inversely proportional to spatial resolution). The instantaneous errors grow in time as the solutions diverge, but the dependence on resolution is similar — see figure (4.6).

As elaborated in the next section, a significant part of this error arises from the poor numerical representation of the underlying PV-controlled balanced motions

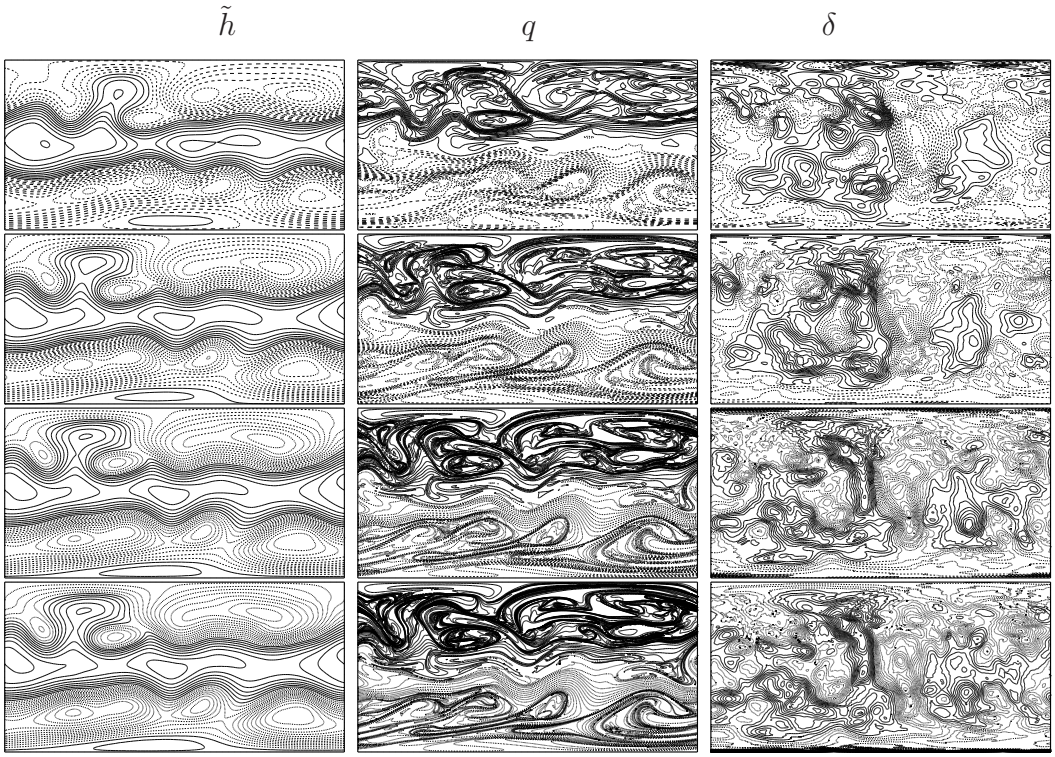

FIGURE 4.5: Effect of varying resolution on the perturbed fields. Height anomaly (left), PV (middle) and divergence (right) at day 15 are compared at 64^2, 128^2, 256^2 and 512^2 resolution (top to bottom).

when using $\tilde{h}$ and δ as prognostic variables [49, 50]. This leads to excessive noise, particularly near the poles (seen here in δ at the two highest resolutions), which can sometimes cause the model to blow up, even with larger latitudinal damping. This noise does not develop in the more advanced model, CA_1, described in the following section.

The effect of time-step is shown in figure (4.7), for the height field at day 15 and for time steps $\Delta t = 0.00125$, 0.0025, 0.005, 0.01, 0.02 and 0.04 (corresponding to 0.210, 0.43521, 0.842, 1.684, 3.368 and $6.735\Delta t_{\mathrm{CFL}}$) (note: [67] used $\Delta t \approx 7\Delta t_{\mathrm{CFL}}$). The time-averaged r.m.s. height differences between the finest time-step case and the others (in order of increasing Δt) are 0.534%, 1.11%, 2.25%, 4.81% and 7.59%. (The corresponding PV differences are 0.43571%, 0.744%, 1.33%, 1.48% and 3.94%.) Using larger time steps is not nearly as detrimental as using

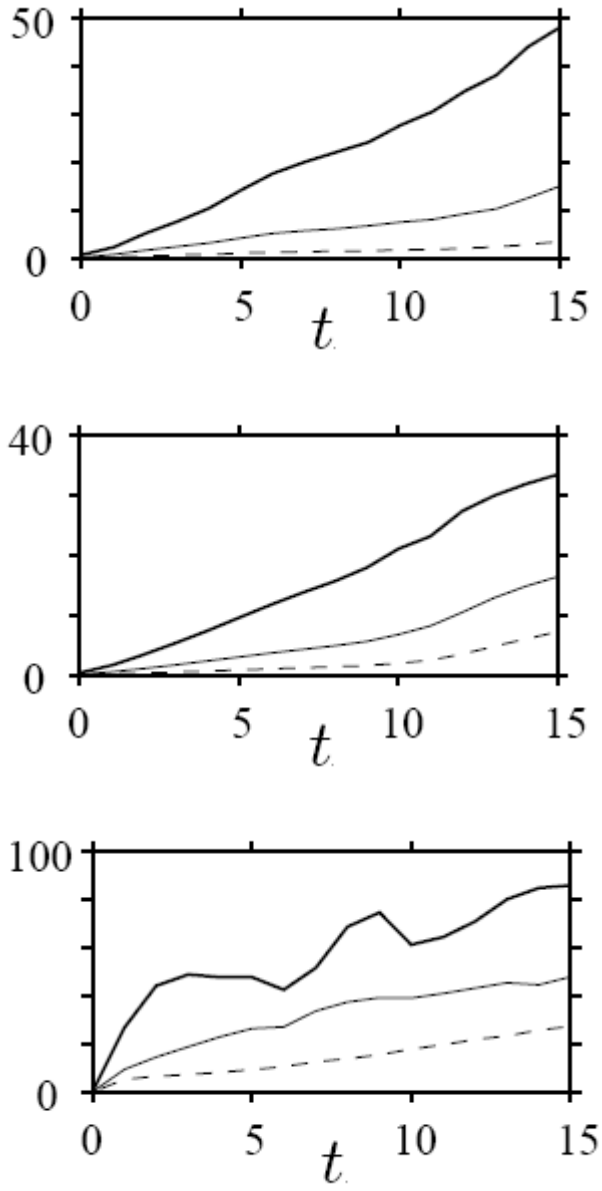

FIGURE 4.6: Instantaneous percentage r.m.s. error in height anomaly (top), PV (middle) and divergence (bottom) versus time. The errors for 64^2 (solid bold), 128^2 (solid) and 256^2 (dashed) resolutions are computed relative to the average r.m.s. field amplitudes in the 512^2 resolution case.

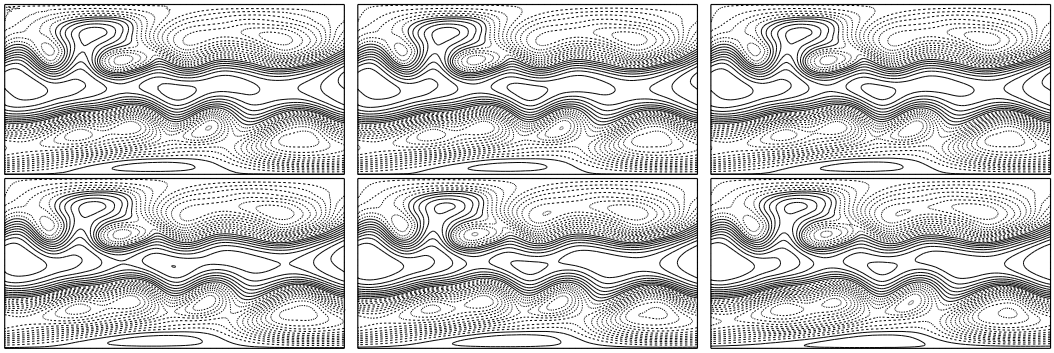

FIGURE 4.7: Effects of varying time-step on the perturbed height field at day 15. The time-step increases in factors of 2 from the upper left (where $\Delta t = 0.00125$) to the lower right (where $\Delta t = 0.04$).

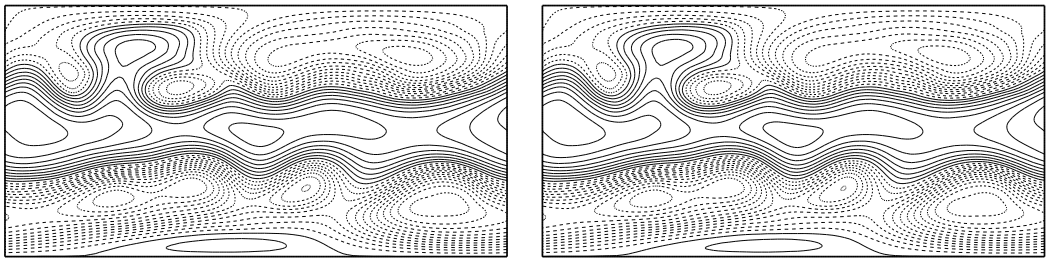

FIGURE 4.8: Effects of varying damping on the perturbed height field at day 15. Damping coefficients 0.1 and 0.01 are compared (left and right).

coarser spatial resolution, but errors are clearly noticeable for time-steps much is excess of t_{CFL} (errors for divergence are much higher, ranging from 40 to 80%). The errors stem in part from the semi-implicit scheme, which couples the equations for height and divergence, fields which are often very different in character. The height field tends to be dominantly balanced and slowly evolving (like the PV), while the divergence tends to contain significantly more high frequency motions, i.e. gravity waves. Simply slowing down the waves in the semi-implicit scheme does not eliminate them — indeed they may be more easily excited by the vortical motions. This coupling can, and arguably should, be avoided, as the results of the next section demonstrate.

Finally, the latitudinal damping coefficient has no perceptible impact on the solution accuracy, for $0.01 \leq D \leq 0.1$ — see figure (4.8). Time-averaged r.m.s.

differences in $\tilde{h}$, δ and PV are just 0.314%, 4.82% and 0.43532%. Values of D smaller than 0.01 however lead to numerical instability in some cases.

Chapter 5

An improved numerical method

5.1 Introduction to CA_1

Previous work [17, 49] identified a new approach to significantly improving solution accuracy at little extra computational cost. The CA_0 model differs from conventional models principally in the way that it handles PV conservation. Otherwise, it uses standard variables, at least for spectral models. But there is another important aspect of PV which is not treated explicitly, namely the way in which PV controls much of the fluid motion, through underlying "balance relations" (see [38, 44]). For example, at small Rossby and Froude numbers, geostrophic balance may be expected to hold everywhere except near the equator. This balance implies that the height field is instantaneously related to the PV field (in general via an elliptic operator). Now suppose one tried to run a shallow-water model under these conditions, with the height field as one of the prognostic variables. Balance implies there is a direct link between height and PV at any time, but the numerics does not see this and instead integrates the height field as an independent variable. Of course it should, one might believe, in order to also capture gravity waves, motions not part of the balance. But the problem is that numerical discretisation errors,

both in space and in time, make it difficult to maintain the underlying balance, and the errors show up erroneously as gravity waves.

A way around this problem is to use a set of prognostic variables which better distinguishes balanced motions and gravity waves, ideally PV and a pair of 'wave' variables (cf. [17, 49]). The idea is to represent the *departure* from balance by these 'wave' variables. Then, to recover the original variables $\tilde{h}$, u and v, one solves a series of elliptic problems, like in "PV inversion" [44], but involving the complete set of new variables (see below). The crucial point is that these elliptic problems *reduce* to balance relations when the 'wave' variables are ignored. This feature leads to a significant reduction in erroneous gravity waves, and it improves the prediction of the dominant balanced motions.

In reality, there is no pair of variables that represent pure gravity waves for nonlinear flows, and efficiency considerations force a compromise. Here, we use a pair of variables that proved optimal in the f-plane context, see [49], taking into account robustness, accuracy, and efficiency. One of the variables is the velocity divergence $\delta = \boldsymbol{\nabla} \cdot \mathbf{u}$, already used in CA_0. The other is the acceleration divergence

$$\gamma = \boldsymbol{\nabla} \cdot \frac{\mathrm{D}\mathbf{u}}{\mathrm{D}t} = f\zeta - \beta u - c^2 \boldsymbol{\nabla}^2 \tilde{h} \tag{5.1}$$

where $\beta = \mathrm{d}f/\mathrm{d}\phi = 2\Omega_E \cos\phi$.

In the f-plane context, γ/f is the ageostrophic vorticity. The prognostic equations for δ and γ are straightforwardly obtained using equations (1.10) and (1.12), [11]. This model is referred to as CA_1.

The primitive variables $(\tilde{h}, u, v)$ are recovered from the new ones (q, δ, γ) as follows. First, the divergence potential χ is recovered directly from δ using equation (1.6). This then gives the divergent part of the velocity field from equation (1.13). The non-divergent part involving ψ however requires ζ, which depends on q and $\tilde{h}$. So,

we need $\tilde{h}$ to proceed. An equation for $\tilde{h}$ is available in the definition of γ, which however depends on u and hence ψ. So, the equations for $\tilde{h}$ and ψ are coupled. But, they are both linear, given (q, δ, γ). In practise, the equations are solved iteratively, rewriting equation (5.1) as

$$\left(\boldsymbol{\nabla}^2 - \frac{f^2}{c^2}\right)\tilde{h} = f\left(\zeta - f\tilde{h}\right) - \beta u - \gamma \tag{5.2}$$

with terms on the right-hand-side evaluated using previous iterates. Numerically, these equations converge exponentially fast, so that only a few iterations are required to achieve convergence (here when the maximum pointwise difference between successive $\tilde{h}$ iterates is less that 10^{-8}).

5.2 CA_1 results for the Rossby-Haurwitz test case

First of all, no latitudinal damping was found to be necessary for CA_1. Divergence fields are noticeably smoother, not because of diffusion, but because the underlying balance is better respected.

At early time periods, the CA_0 and CA_1 results differ negligibly for the original Rossby-Haurwitz wave test. But this only tests the correctness of the numerical model. To test accuracy, we need to look at how the models deal with a complex flow having a wide range of spatial and temporal scales. We focus on the perturbed Rossby-Haurwitz case, which destabilises quickly and reproducibly. At the benchmark resolution, 128^2 and $\Delta t \approx \frac{1}{2}\Delta t_{\mathrm{CFL}}$, the height and PV fields differ little between the models, see figures (5.1) and (5.2), which compare the main fields given by CA_0 and CA_1, but the divergence field is significantly smoother in CA_1. Movies of the dynamical evolution show that the pattern of δ moves with the PV, indicating that even δ is dominantly balanced in this flow. Time-averaged

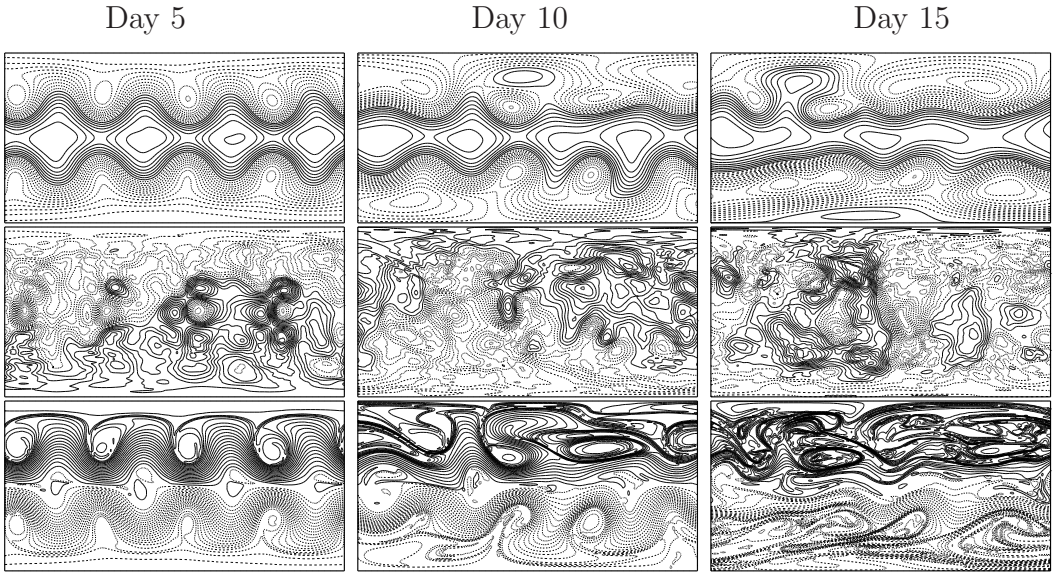

FIGURE 5.1: CA_0 perturbed fields at days 5, 10 and 15 (left to right). Top row: height. Middle row: divergence. Bottom row: PV.

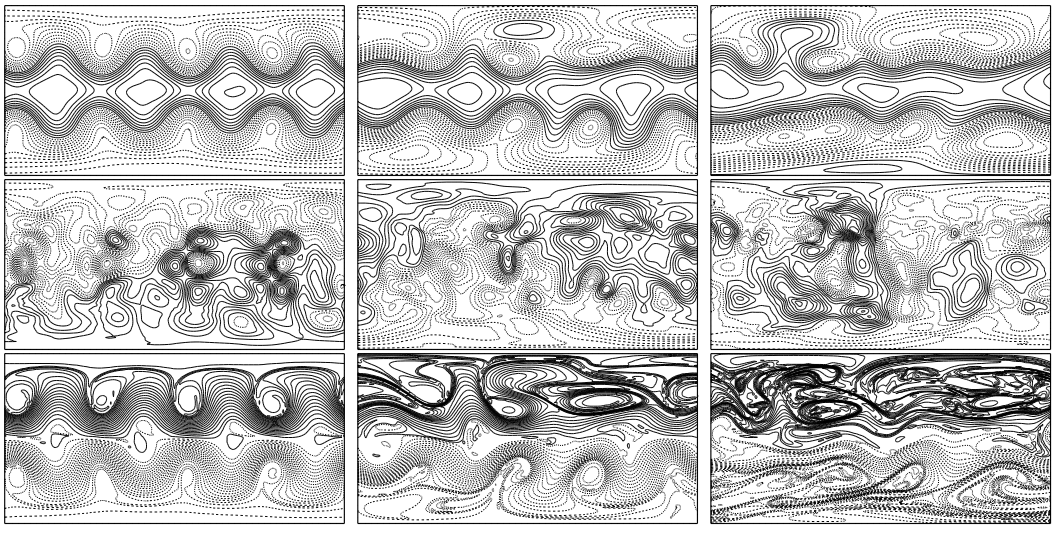

FIGURE 5.2: CA_1 perturbed fields at days 5, 10 and 15 (left to right). Top row: height. Middle row: divergence. Bottom row: PV.

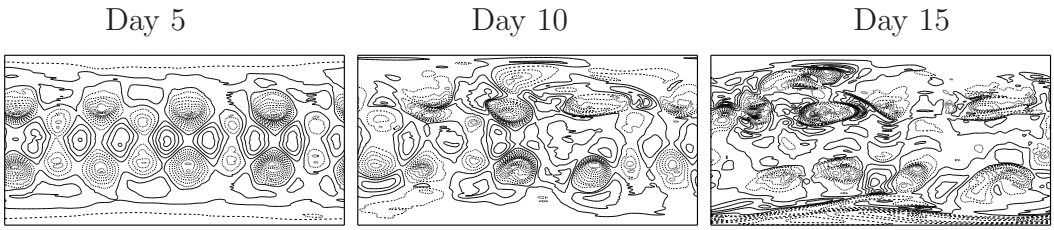

FIGURE 5.3: Acceleration divergence (γ) at days 5, 10 and 15. Contour interval: 0.02 days^{-2}.

r.m.s. differences between the fields in the two models are 1.77%, 8.62% and 2.46%, for $\tilde{h}$, δ and PV respectively. Note that the divergence error is most significant. Convergence is faster in CA_1, as seen for instance when comparing time-steps of $\Delta t = 0.00125$ and $\Delta t = 0.0025$, for which $\tilde{h}$, δ and PV differences are 0.43513%, 21.7% and 0.349%, compared to 0.534%, 40.2% and 0.43571% in CA_0. Also, when comparing 256^2 and 128^2 resolutions, $\tilde{h}$, δ and PV differences are 4.82%, 27.3% and 5.65% in CA_1, while they are 5.76%, 29.0% and 6.53% in CA_0.

The field of acceleration divergence γ, never previously illustrated, is shown in figure (5.3) at times corresponding to figures (5.1 and 5.2). This field is more highly structured than δ, with many more small-scale features.

Largest values occur within strong cyclonic vortices, which tend to be more ageostrophic than anti-cyclonic vortices in shallow-water flows, [55]. Again however the pattern of γ largely follows PV (not shown), indicating that γ like δ is dominantly balanced. Ideally, we would like to use a better choice of 'wave' variables, e.g. the first time derivatives of δ and γ (cf. [49, 50]), but the reduced computational efficiency and the potential lack of robustness for strongly ageostrophic flows indicate that it is impractical to do so. Nonetheless, CA_1 does appear to build in a degree of balance, which — perhaps surprisingly — *includes* equatorial regions. Overall, γ and δ contribute little to the fluid motion, as seen for example when comparing the meridional velocity v at day 15 with its 'balanced' counterpart v_0 (obtained

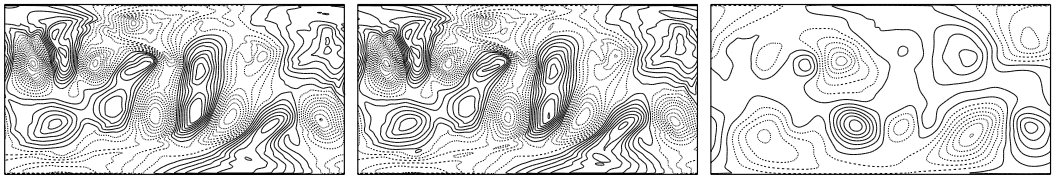

FIGURE 5.4: The Meridional velocity v (left), its 'balanced' counterpart v_0 (middle), and the difference $v - v_0$ (right) at day 15. Note that the contour intervals are $5ms^{-1}$ for v and v_0, but only $0.5ms^{-1}$ for $v - v_0$.

from the PV alone by imposing $\delta = \gamma = 0$), see figure (5.4). Differences are no more than a few percent, *even at the equator*. This important finding underscores the utility of this choice of variables for modelling spherical shallow-water flows. In addition, $\delta = \gamma = 0$ balance may prove useful for diagnosing fluid motion near the equator, where geostrophic balance fails.

5.3 Conclusion

We have revisited one of the standard test cases proposed for the shallow-water equations in spherical geometry using an explicitly PV-conserving contour-advection model. Our results closely reproduce previous results obtained with a variety of different models at early times. At late times, Thuburn & Li demonstrated that this simple test breaks down into a complex turbulent flow. This suggested a small modification of the original test to exploit the physical instability and obtain a rapid and reproducible turbulent breakdown of the original flow. This, we argue, is a better test for numerical methods being considered for implementation in more realistic global atmospheric and oceanic models. The flow develops a wide range of spatial and temporal scales, and properly challenges numerical models. This is important.

The new contour-advection model introduced here copes well with this complexity by explicitly conserving PV and preserving dynamically active sharp gradients

(fronts). This is a major advantage of contour advection, and one which is not lessened when non-conservative diabatic effects are taken into account [14]. We also found that it is important to preserve the underlying balance, the implicit control exerted by PV, in these flows. To this end, we extended an idea, first implemented in the f-plane context, of using a new set of prognostic variables which distinguishes balanced vortical motions and unbalanced gravity waves, at least to leading order [49]. At almost no extra computational expense, this significantly improves the accuracy of the balanced part of the flow, and in turn, the unbalanced part as well. This simple transform may be worthwhile extending to more realistic contexts.

Chapter 6

Further developments in CASL

6.1 Modification to fourth-order finite differencing in latitude

Next, we discuss a recent development in the latitudinal representation of variables in the CASL algorithm. Two main improvements have been made — the use of fourth-order compact differencing and the use of a shifted grid in latitude, at "half-latitudes", to increase accuracy at the poles. The algorithm modifications were carried out by Ali Mohebalhojeh and David Dritschel at the University of St Andrews. In [51], the fourth-order routine is introduced within the CASL method and many of the numerical details from that paper have been reproduced here, cited where appropriate. This extension of the CASL algorithm is tested under simple and more complex conditions by the author to provide validation of the improvements and allow the reader to note the advancements made and the impacts on CASL calculations.

In addition, a new type of regular grid is also introduced. In [51], polar boundary conditions were found to cause a loss of formal accuracy from fourth-order to

third-order. This can be avoided by the use of a grid shifted half the latitudinal grid-length, $\Delta\phi$, from the poles. This allows straightforward differentiation with respect to ϕ across the poles, effectively removing any need for boundary conditions there (indeed the sphere has no boundary). As in [51], with the full grid points given as $\phi_j^* = -\pi/2 + j\Delta\phi$, for $j = 0, 1, \ldots, N$, we can define the new half-grid points as $\phi_j = -\pi/2 + (j - 1/2)\Delta\phi$, for $j = 1, 2, \ldots, N$.

6.1.1 Fourth-order CASL models

As a continuation of Chapter 1.4, where the Helmholtz operator for second-order finite differencing ($\mathcal{H}$) was introduced, we must also discuss a second operator, arising in the semi-implicit time-stepping of both δ and γ, which takes the form $\Gamma = \boldsymbol{\nabla}^2 - c^2/(\Delta t)^2$, with Δt the time step. Here, we outline how these operators are treated using fourth-order compact differencing.

We first consider the Helmholtz equation

$$\left(\boldsymbol{\nabla}^2 - \frac{f^2}{c^2}\right)\tilde{h} = \left(\frac{1}{\cos^2\phi}\frac{\partial^2}{\partial\lambda^2} + \frac{1}{\cos\phi}\frac{\partial}{\partial\phi}\cos\phi\frac{\partial}{\partial\phi} - \frac{f^2}{c^2}\right)\tilde{h} = F\,, \tag{6.1}$$

where F represents the terms on the right hand side of the acceleration divergence equation (equation (5.2)). This is the central equation used to obtain the height field from γ and q. For each longitudinal Fourier component with wavenumber m, we have that $F = \hat{F}_m(\phi)e^{im\lambda}$ and the solution for equation (6.1) is therefore of the form $\tilde{h} = \hat{h}_m(\phi)e^{im\lambda}$, with the relation for $\hat{h}$, from [51],

$$\frac{d^2\hat{h}}{d\phi^2} - \tan\phi\frac{d\hat{h}}{d\phi} - \left(\frac{m^2}{\cos^2\phi} + \frac{f^2}{c^2}\right)\hat{h} = \hat{F}\,. \tag{6.2}$$

Using the notation

$$\hat{\Gamma} = \frac{d\hat{h}}{d\phi} \quad \text{and} \quad \hat{\Gamma}_\phi = \frac{d^2\hat{h}}{d\phi^2}\,,$$

one may obtain the fourth-order compact relations for the first and second latitudinal derivatives of $\tilde{h}$, from [51], as

$$\frac{1}{6}\hat{\Gamma}_{j-1} + \frac{2}{3}\hat{\Gamma}_j + \frac{1}{6}\hat{\Gamma}_{j+1} = \frac{\hat{h}_{j+1} - \hat{h}_{j-1}}{2\Delta\phi}\,, \tag{6.3}$$

$$\frac{1}{12}\left(\hat{\Gamma}_\phi\right)_{j-1} + \frac{5}{6}\left(\hat{\Gamma}_\phi\right)_j + \frac{1}{12}\left(\hat{\Gamma}_\phi\right)_{j+1} = \frac{\hat{h}_{j+1} - 2\hat{h}_j + \hat{h}_{j-1}}{(\Delta\phi)^2}\,. \tag{6.4}$$

The general result for points ($j = 2, 3, \ldots, N-1$), from [51], is

$$A_j \begin{pmatrix} \hat{h} \\ \hat{\Gamma} \end{pmatrix}_{j-1} + B_j \begin{pmatrix} \hat{h} \\ \hat{\Gamma} \end{pmatrix}_j + C_j \begin{pmatrix} \hat{h} \\ \hat{\Gamma} \end{pmatrix}_{j+1} = \begin{pmatrix} \hat{G}_j \\ 0 \end{pmatrix}, \tag{6.5}$$

where

$$\hat{G}_j = \frac{1}{12}\hat{F}_{j-1} + \frac{5}{6}\hat{F}_j + \frac{1}{12}\hat{F}_{j+1}\,,$$

and A_j, B_j, and C_j are the 2×2 matrices

$$A_j = \begin{pmatrix} \dfrac{1}{(\Delta\phi)^2} - \dfrac{1}{12}\left(\dfrac{f_{j-1}^2}{c^2} + \dfrac{m^2}{\cos^2\phi_{j-1}}\right) & -\dfrac{1}{12}\tan\phi_{j-1} \\ \dfrac{1}{2\Delta\phi} & \dfrac{1}{6} \end{pmatrix},$$

$$B_j = \begin{pmatrix} -\dfrac{2}{(\Delta\phi)^2} - \dfrac{5}{6}\left(\dfrac{f_j^2}{c^2} + \dfrac{m^2}{\cos^2\phi_j}\right) & -\dfrac{5}{6}\tan\phi_j \\ 0 & \dfrac{2}{3} \end{pmatrix},$$

$$C_j = \begin{pmatrix} \dfrac{1}{(\Delta\phi)^2} - \dfrac{1}{12}\left(\dfrac{f_{j+1}^2}{c^2} + \dfrac{m^2}{\cos^2\phi_{j+1}}\right) & -\dfrac{1}{12}\tan\phi_{j+1} \\ -\dfrac{1}{2\Delta\phi} & \dfrac{1}{6} \end{pmatrix}.$$

For the polar points, $j = 1$ and $j = N$, separate treatment is required, [51]. To be able to use the differencing relations in equations (6.3) and (6.4), ϕ must vary monotonically when crossing the poles. This is possible by noting that equation

(6.2) is valid if ϕ is extended periodically from $[-\pi/2, \pi/2]$ to $[-\pi/2, 3\pi/2]$ in crossing the north pole and to $[-3\pi/2, \pi/2]$ in crossing the south pole, [51]. Consequently, sign changes in the cosine and tangent functions must be considered at the poles.

For odd wavenumber m, we have $\hat{h}_0 = -\hat{h}_1$, $\hat{\Gamma}_0 = \hat{\Gamma}_1$ and $\hat{F}_0 = -\hat{F}_1$ because of a sign change due to the phase shift of π in $\mathrm{e}^{\mathrm{i}m\lambda}$ when crossing the south pole. There is a further sign change in $\hat{\Gamma}$ when crossing the pole, coming from the latitudinal derivative. The above relations together with $\cos\phi_0 = -\cos\phi_1$ and $\tan\phi_0 = -\tan\phi_1$ are used to remove contributions from the point $j = 0$ in equation (6.5) for $j = 1$ (note, A_1 is not used).

In a similar fashion, $\hat{h}_{N+1} = -\hat{h}_N$, $\hat{\Gamma}_{N+1} = \hat{\Gamma}_N$, $\hat{F}_{N+1} = -\hat{F}_N$, $\cos\phi_{N+1} = -\cos\phi_N$, and $\tan\phi_{N+1} = -\tan\phi_N$ are used to remove contributions from the point $j = N + 1$ in equation (6.5) for $j = N$ (now, C_N is not used). The result, from [51], is

$$
\begin{aligned}
B_1 &= \begin{pmatrix} -\dfrac{3}{(\Delta\phi)^2} - \dfrac{3}{4}\left(\dfrac{f_1^2}{c^2} + \dfrac{m^2}{\cos^2\phi_1}\right) & -\dfrac{3}{4}\tan\phi_1 \\ -\dfrac{1}{2\Delta\phi} & \dfrac{5}{6} \end{pmatrix}, \\
B_N &= \begin{pmatrix} -\dfrac{3}{(\Delta\phi)^2} - \dfrac{3}{4}\left(\dfrac{f_N^2}{c^2} + \dfrac{m^2}{\cos^2\phi_N}\right) & -\dfrac{3}{4}\tan\phi_N \\ \dfrac{1}{2\Delta\phi} & \dfrac{5}{6} \end{pmatrix}.
\end{aligned}
$$

For even m, we have $\hat{h}_0 = \hat{h}_1$, $\hat{\Gamma}_0 = -\hat{\Gamma}_1$, $\hat{F}_0 = \hat{F}_1$, $\hat{h}_{N+1} = \hat{h}_N$, $\hat{\Gamma}_{N+1} = -\hat{\Gamma}_N$, and $\hat{F}_{N+1} = \hat{F}_N$. These result in similar relations for B_1 and B_N:

$$B_1 = \begin{pmatrix} -\frac{1}{(\Delta\phi)^2} - \frac{11}{12}(\frac{f_1^2}{c^2} + \frac{m^2}{\cos^2\phi_1}) & -\frac{3}{4}\tan\phi_1 \\ \frac{1}{2\Delta\phi} & \frac{1}{2} \end{pmatrix},$$

$$B_N = \begin{pmatrix} -\frac{1}{(\Delta\phi)^2} - \frac{11}{12}(\frac{f_N^2}{c^2} + \frac{m^2}{\cos^2\phi_N}) & -\frac{3}{4}\tan\phi_N \\ -\frac{1}{2\Delta\phi} & \frac{1}{2}\,. \end{pmatrix}.$$

For the Poisson equation,

$$\boldsymbol{\nabla}^2\psi = F\,, \tag{6.6}$$

the same relations are used for non-zero m, omitting the f^2/c^2 term. For $m = 0$, the Poisson equation is singular and the zonally averaged solution ($\bar{\psi}$) is known only to within a constant. The dynamically important quantity is the latitudinal derivative, $\mathrm{d}\bar{\psi}/\mathrm{d}\phi$, and not $\bar{\psi}$ itself. Using the auxiliary variable

$$\bar{\Upsilon} = \frac{\mathrm{d}\bar{\psi}}{\mathrm{d}\phi}\cos\phi$$

and multiplying equation (6.6) by $\cos\phi$, the equation for $m = 0$ becomes

$$\frac{\mathrm{d}\bar{\Upsilon}}{\mathrm{d}\phi} = \bar{F}\cos\phi = \bar{G}\,. \tag{6.7}$$

To discretise equation (6.7), we use the fourth-order compact relation relating the derivative of a function at half-grid points to the function values at full-grid points (denoted by $\bar{\Upsilon}^*_j$), [26, 68],

$$\frac{1}{22}\bar{G}_{j-1} + \bar{G}_j + \frac{1}{22}\bar{G}_{j+1} = \frac{12}{11}\left(\frac{\bar{\Upsilon}^*_j - \bar{\Upsilon}^*_{j-1}}{\Delta\phi}\right). \tag{6.8}$$

The boundary condition at the south and north poles are $\bar{\Upsilon}^*_0 = \bar{\Upsilon}^*_N = 0$, and

equation (6.8) is solved for $(j = 1, 2, \ldots, N-1)$. For consistency with the boundary conditions, we require that $\sum_{j=1}^{N} \left[\frac{1}{22}\bar{G}_{j-1} + \bar{G}_j + \frac{1}{22}\bar{G}_{j+1}\right] = 0$ (this is the fourth-order expression for the integral of G with respect to ϕ). To enforce this consistency requirement, we modify F_j to $F_j - C$, where C is a constant to be determined by the consistency condition, given by [51] as

$$C = \frac{\bar{G}_1 + \frac{12}{11}\sum_{j=2}^{N-1}\bar{G}_j + \bar{G}_N}{\cos\phi_1 + \frac{12}{11}\sum_{j=2}^{N-1}\cos\phi_j + \cos\phi_N}\,. \tag{6.9}$$

Note that $\bar{G}_0 = \bar{F}_0\cos\phi_0 = -\bar{F}_1\cos\phi_1 = -\bar{G}_1$ and therefore $\bar{\Upsilon}_1^* = \frac{\Delta\phi}{24}(21\bar{G}_1 + \bar{G}_2)$, which enables us to solve equation (6.8) for $\bar{\Upsilon}_j^*$ recursively, as follows

$$\bar{\Upsilon}_j^* = \bar{\Upsilon}_{j-1}^* + \frac{\Delta\phi}{24}(\bar{G}_{j-1} + 22\bar{G}_j + \bar{G}_{j+1}) \qquad (j = 2, \ldots, N-1)\,. \tag{6.10}$$

The full grid, $\bar{\Upsilon}^*$, is then interpolated to the half-grid using the fourth-order compact interpolation, from [26],

$$\frac{1}{6}\bar{\Upsilon}_{j-1} + \bar{\Upsilon}_j + \frac{1}{6}\bar{\Upsilon}_{j+1} = \frac{2}{3}(\bar{\Upsilon}_{j-1}^* + \bar{\Upsilon}_j^*)\,, \tag{6.11}$$

for $\bar{\Upsilon}_1, \bar{\Upsilon}_2, \ldots, \bar{\Upsilon}_N$. In crossing the poles, there are two sign changes for $\bar{\Upsilon}$, one due to the cosine function and the other due to the latitudinal derivative, giving $\bar{\Upsilon}_0 = \bar{\Upsilon}_1$ and $\bar{\Upsilon}_{N+1} = \bar{\Upsilon}_N$. Therefore, equation (6.11) for $j = 1$ and $j = N$ becomes

$$\frac{7}{6}\bar{\Upsilon}_1 + \frac{1}{6}\bar{\Upsilon}_2 = \frac{2}{3}\bar{\Upsilon}_1^* \tag{6.12}$$

$$\frac{1}{6}\bar{\Upsilon}_{N-1} + \frac{7}{6}\bar{\Upsilon}_N = \frac{2}{3}\bar{\Upsilon}_{N-1}^*\,, \tag{6.13}$$

which together with equation (6.11), for $(j = 2, \ldots, N-1)$, constitute a tridiagonal system.

6.2 The new CASL algorithms

As in [51], we shall denote the second-order, full grid algorithms, seen in previous chapters as CA_0 and CA_1, as $\mathrm{CA}^{2-fg}_{\tilde{h},\delta}$ and $\mathrm{CA}^{2-fg}_{\delta,\gamma}$, respectively. The new half-grid, fourth-order algorithms, corresponding to the above prognostic variable choices, will be denoted as $\mathrm{CA}^{4-hg}_{\tilde{h},\delta}$ and $\mathrm{CA}^{4-hg}_{\delta,\gamma}$.

6.2.1 Examination of fourth-order finite differencing and the γ field

The acceleration divergence field, γ, was found to also provide valuable diagnostics for comparison and subsequent improvements in the CASL algorithms. Upon viewing the γ fields for the second and fourth-order algorithms it was clear that, whilst differences were expected, this field was susceptible to developing noise around the poles in both second and fourth-order algorithms.

To help resolve this issue, a simple smooth test case was devised by D. Dritschel in order to quickly and easily see where any problem areas occurred within the γ fields of $\mathrm{CA}^{2-fg}_{\delta,\gamma}$ and $\mathrm{CA}^{4-hg}_{\delta,\gamma}$. This test case considered a non-divergent flow with the streamfunction given by

$$\psi = A z_{r1} \left(\frac{3}{5} - z_{r1}^2 \right) , \tag{6.14}$$

where z_{r1} is a rotated z coordinate computed from a given latitude (default 30°) and longitude (default 60°) and A is a given constant (default 1). The vorticity is then given by $\zeta = -12\psi$. Additionally, a dimensionless height anomaly of the form

$$\tilde{h} = B \left(z_{r2}^2 - \frac{1}{3} \right) , \tag{6.15}$$

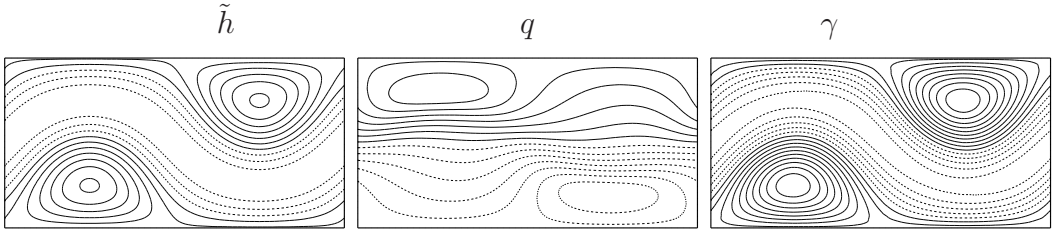

FIGURE 6.1: Initial depth, PV and acceleration divergence fields for the acceleration divergence test case.

in which z_{r2} is another rotated z coordinate, given by latitude (default $-45°$) and longitude (default $-90°$) and B is a constant (default 0.2).

The exact fields of depth, divergence, vorticity, acceleration divergence and velocity components are then computed analytically and the initial condition (shown in figure (6.1)) is then run by the CASL algorithms so that the fractional RMS errors computed at initial time for each field may be found.

One crucial point was highlighted by an erroneous increase in RMS error in the γ field on increasing resolution. This was found to be due to a lack of Broutman filtering acting upon the Laplacian solver routine. Such a filter is routinely used in computing longitudinal derivatives, and for consistency, we found that it should also be included when applying the Laplace operator. This led to substantial improvements near the poles, restoring second and fourth-order accuracy to $\mathrm{CA}_{\delta,\gamma}^{2-fg}$ and $\mathrm{CA}_{\delta,\gamma}^{4-hg}$, respectively. For a detailed analysis of the effect of this filtering, see Chapter 7.1.2 and the discussion regarding table (7.3).

Two main links between the acceleration divergence field and other fields were noted. Changes made during fourth-order algorithm testing included variation of the PV jump value with resolution. This was fixed at all resolutions in the original Rossby test case in order to maintain a direct comparison to previous contour intervals shown by Thuburn and Li in [67]. At higher resolutions, however, it makes sense to reduce the PV jump for increased accuracy. This results in a

Resolution	**Error for** $\mathrm{CA}^{2-fg}_{\delta,\gamma}$	**Error for** $\mathrm{CA}^{4-hg}_{\delta,\gamma}$
128^2	0.02098163	0.001587233
256^2	0.01035668	0.000686866
512^2	0.00510787	0.000311070

TABLE 6.1: Fractional RMS errors in the vorticity field for $\mathrm{CA}^{2-fg}_{\delta,\gamma}$ and $\mathrm{CA}^{4-hg}_{\delta,\gamma}$ at resolutions 128^2, 256^2 and 512^2 for the γ test case.

Resolution	**Error for** $\mathrm{CA}^{2-fg}_{\delta,\gamma}$	**Error for** $\mathrm{CA}^{4-hg}_{\delta,\gamma}$
128^2	0.00110117	0.000619827
256^2	0.00053003	0.000275764
512^2	0.00025858	0.000127800

TABLE 6.2: Fractional RMS errors in the acceleration divergence field for $\mathrm{CA}^{2-fg}_{\delta,\gamma}$ and $\mathrm{CA}^{4-hg}_{\delta,\gamma}$ at resolutions 128^2, 256^2 and 512^2 for the γ test case.

reduction in noise within the γ field upon increasing resolution and reducing the PV jump value. Further details are provided in the next chapter.

Tables (6.1) and (6.2) show the fractional RMS errors for vorticity (top) and acceleration divergence (bottom) with varying resolution, after the corrections mentioned to the CASL algorithms were made. Here, as expected, the errors decrease with increasing resolution and the fourth-order CASL algorithm has less fractional RMS errors for both vorticity and acceleration divergence fields. The equivalent RMS errors for zonal and meridional velocity components (not shown) were comparable between the second and fourth-order algorithms, again as expected, since the test case produces a very smooth initial flow and therefore the initial numerical fields should be (and are) very close to the analytical fields. We also note that, although the results in both fields detailed is better than second-order accurate for $\mathrm{CA}^{4-hg}_{\delta,\gamma}$, true fourth-order accuracy has not yet been attained and this point shall be revisited in the following chapter.

Chapter 7

Fourth-order finite differencing in CASL

7.1 Comparisons for the perturbed Rossby test case

Having identified and implemented changes required within the algorithms for a simple smooth flow, we now return to the modified Rossby-Haurwitz test case for more rigorous analysis of the fourth-order algorithms.

Figure (7.1) shows the initial conditions for the perturbed Rossby test case, detailed earlier. Both second and fourth-order algorithms are given to corroborate earlier results. The point to note, however, is the difference in the initial acceleration divergence, γ, field. In the fourth-order result, the field is much smoother and the sharp edges seen in the second-order contours are removed.

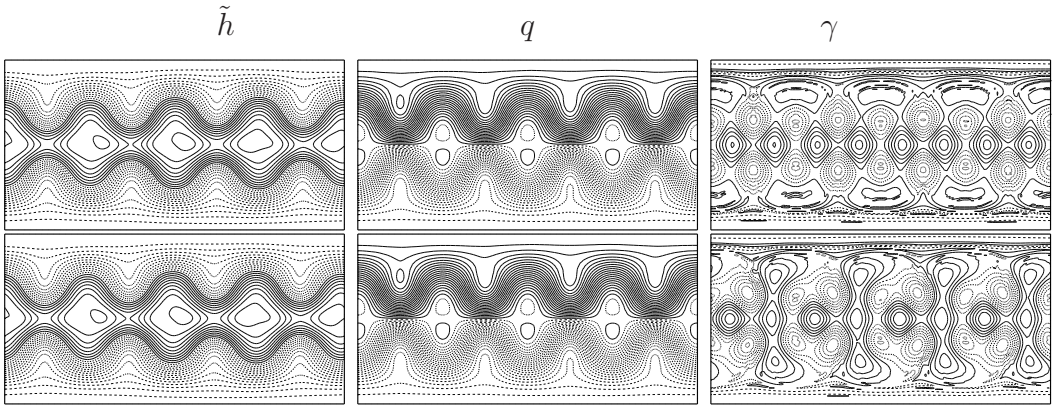

FIGURE 7.1: Initial conditions for the perturbed Rossby test case for the second (top) and fourth-order (bottom) CASL algorithms. Fields shown are the height (left column), PV (middle) and acceleration divergence (right).

Figure (7.1) was obtained by computing γ from the input fields of h and q ($\delta = 0$), i.e. from the discretised form of equation (5.1). It is apparent that this discretisation leads to significant differences in the gamma fields already at t = 0. These differences affect other fields (notably divergence) at subsequent times. After careful analysis of the early time evolution of the flow at resolutions up to 1024^2, it became clear that the problem lies with the 4th-order algorithm, not with the original 2nd-order one (see section 7.1.1 below). At the time of writing, the source of this potential numerical error has not been found. Nevertheless, the 4th-order results are presented for completeness.

Figure (7.2) gives a direct comparison between $\mathrm{CA}^{2-fg}_{\delta,\gamma}$ and $\mathrm{CA}^{4-hg}_{\delta,\gamma}$ algorithms at 128^2 resolution, for the perturbed Rossby test case at later times. As shown, the PV field remains very similar in detail between the two algorithms, as expected, since the flow is dominated by PV and fourth-order accurate advection only slightly changes the position of the PV contours. There are however, visible differences between the fields on increasing finite differencing order at this resolution (128^2).

Figure (7.3) gives a subsequent comparison for increasing resolution on the fourth-order algorithms, comparing $\mathrm{CA}^{4-hg}_{\delta,\gamma}$ at resolutions 64^2, 128^2 and 256^2.

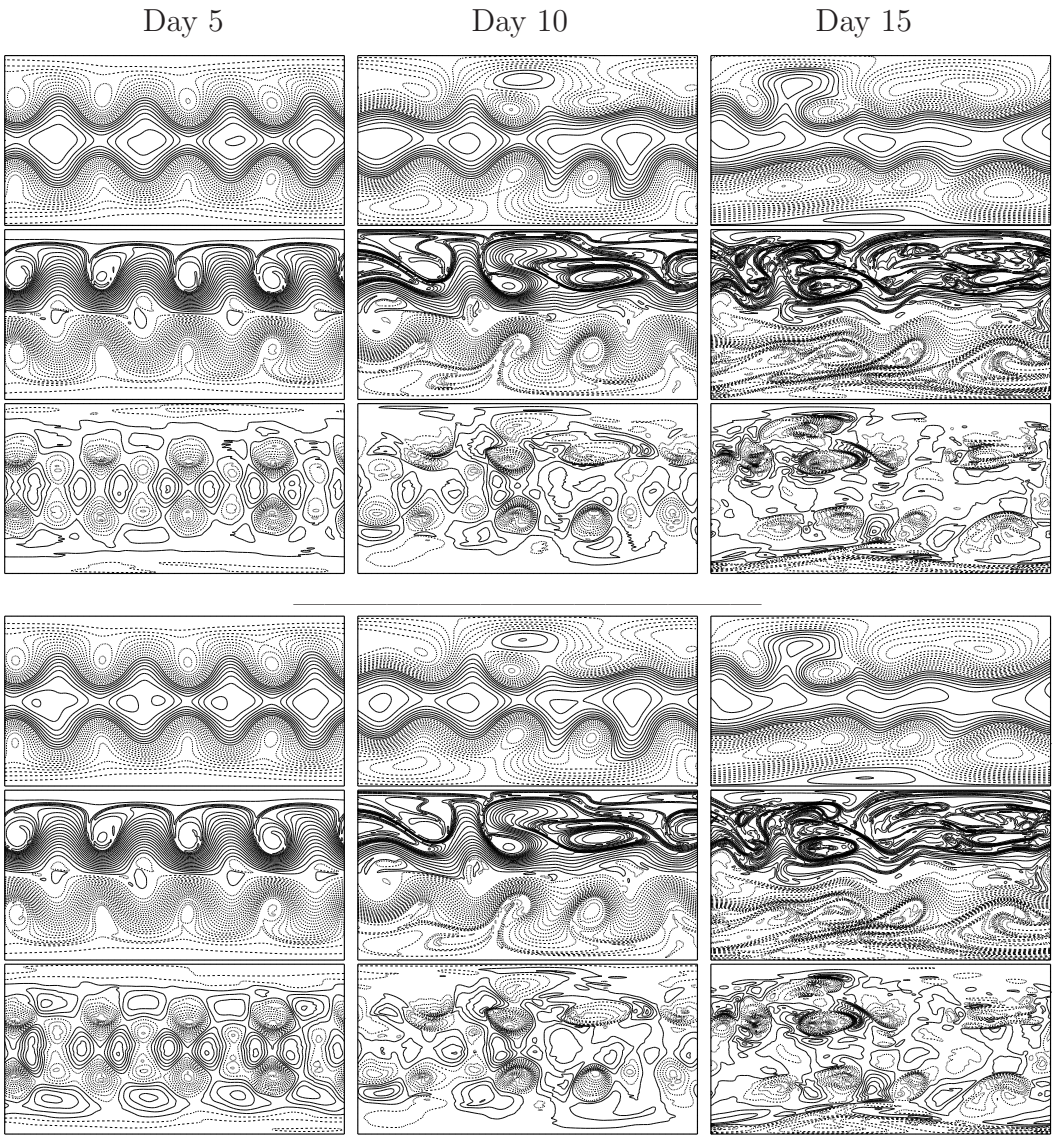

FIGURE 7.2: Detailed comparisons of $\tilde{h}$ (top), q (middle) and γ (bottom) for the second-order $\mathrm{CA}^{2-fg}_{\delta,\gamma}$ (top section) and fourth-order $\mathrm{CA}^{4-hg}_{\delta,\gamma}$ (bottom section) algorithms at days 5, 10 and 15 (left to right) of the perturbed Rossby test case at 128^2 resolution.

Resolution Comparison	**Depth field**	**Divergence field**
64^2 **to** 128^2	0.259822702	0.492281762
128^2 **to** 256^2	0.114428535	0.353599199

TABLE 7.1: Relative RMS differences in the depth and divergence fields for $\mathrm{CA}^{2-fg}_{\delta,\gamma}$ at resolutions 64^2, 128^2 and 256^2 for the Rossby-Haurwitz test case.

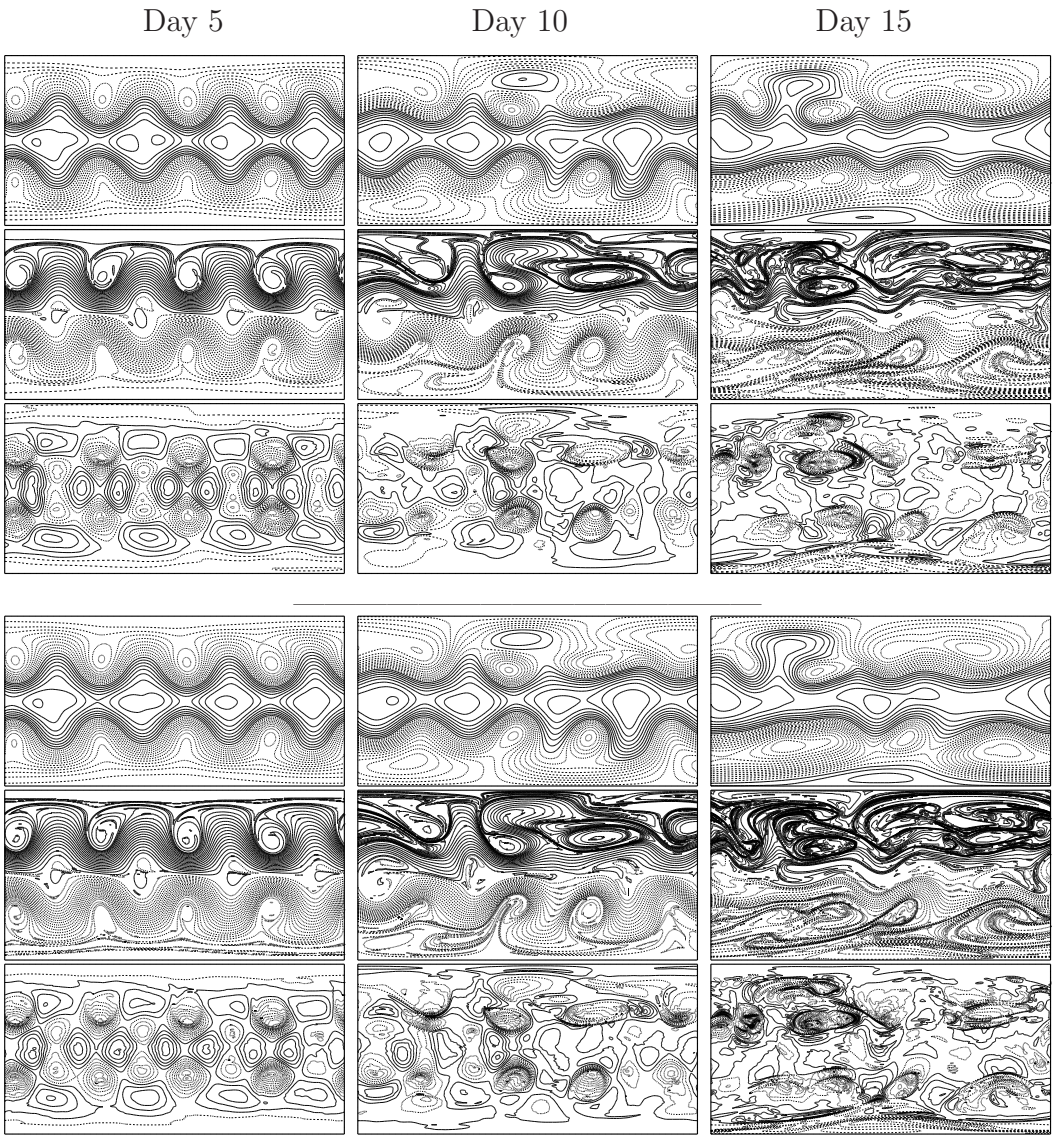

FIGURE 7.3: Resolution comparison of $\tilde{h}$ (top), q (middle) and γ (bottom) for the fourth-order $\mathrm{CA}^{4-hg}_{\delta,\gamma}$ at 128^2 resolution (top section) and at 256^2 resolution (bottom section) for days 5, 10 and 15 (left to right) of the perturbed Rossby test case.

Resolution Comparison	**Depth field**	**Divergence field**
64^2 **to** 128^2	0.304378660	0.914773193
128^2 **to** 256^2	0.133703858	0.789378828

TABLE 7.2: Relative RMS differences in the depth and divergence fields for $\mathrm{CA}^{4-hg}_{\delta,\gamma}$ at resolutions 64^2, 128^2 and 256^2 for the Rossby-Haurwitz test case.

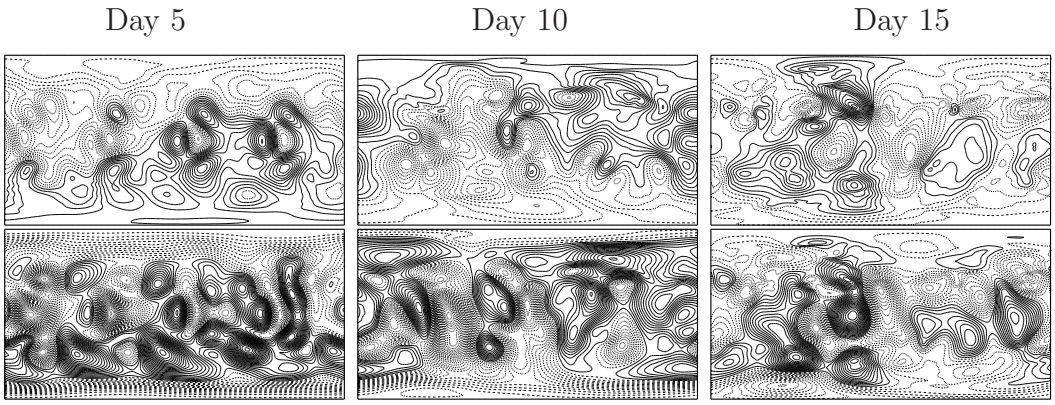

FIGURE 7.4: Comparison of δ fields for $\mathrm{CA}^{2-fg}_{\delta,\gamma}$ (top) and $\mathrm{CA}^{4-hg}_{\delta,\gamma}$ (bottom) algorithms for days 5, 10 and 15. Contour interval for all images 0.002 days^{-1}.

Tables (7.1) and (7.2) show the Relative RMS differences between depth and divergence fields as the resolution is increased. These results do not show the desired (expected) trend of a decrease in the RMS errors, given the improvement in finite differencing order.

Treating the divergence fields separately, figure (7.4) shows the divergence fields for the $\mathrm{CA}^{2-fg}_{\delta,\gamma}$ and $\mathrm{CA}^{4-hg}_{\delta,\gamma}$ algorithms, at days 5 and 10. As can be seen, there is significantly more detail and fine-scale structure in the fourth-order algorithm at the same contour interval. This, together with the erroneous RMS error results, warrants further investigation.

7.1.1 Further analysis of the fourth-order algorithm at high resolutions

Due to the previous unexpected results, a detailed analysis of the updated CASL algorithm was made, during which an interesting anomaly was discovered. At very early time periods, the second and fourth-order algorithms were found to differ in certain fields. Upon closer examination, the divergence field was noted to be significantly different at the standard resolution of 128^2.

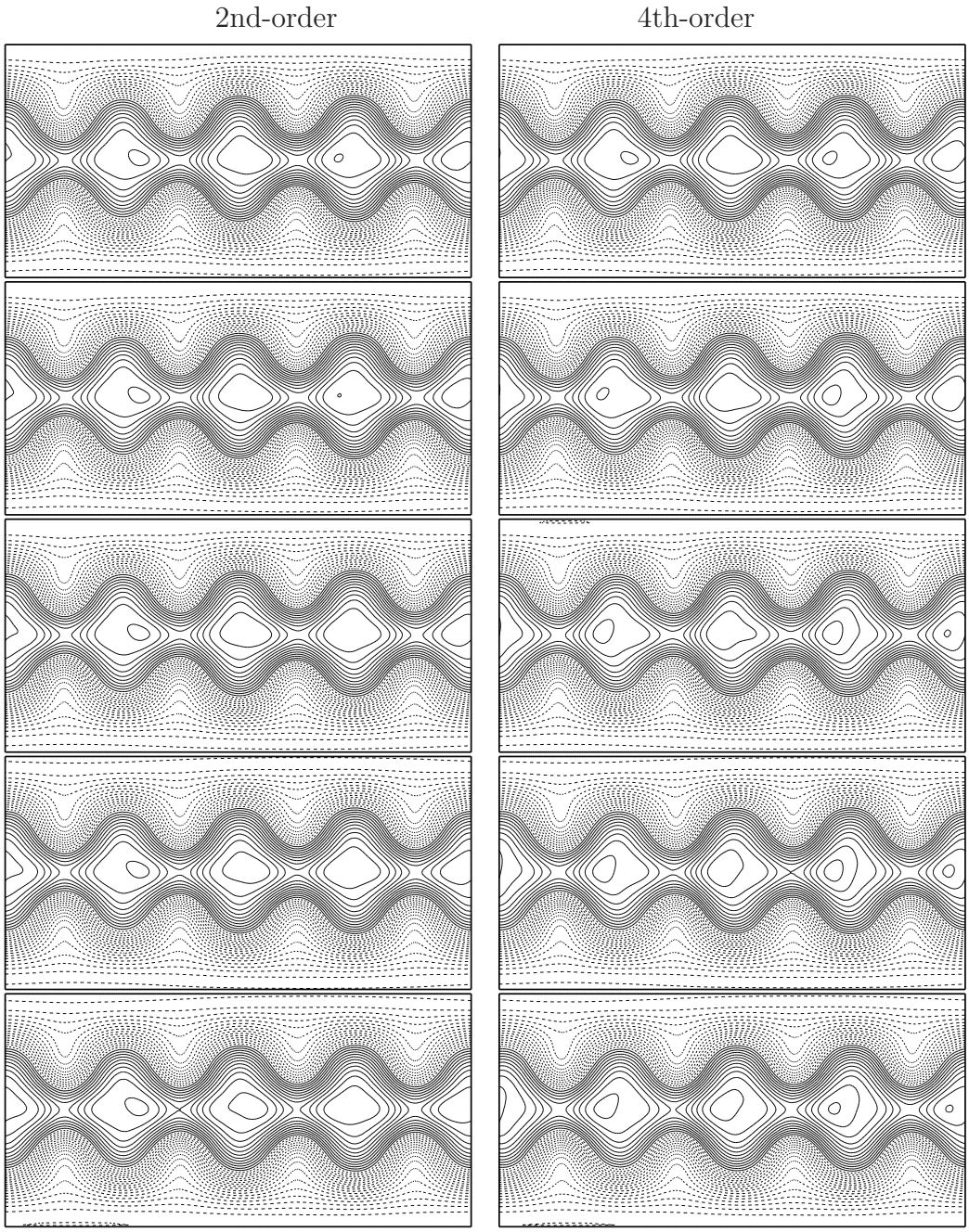

FIGURE 7.5: Comparison of the depth field for $t = 0.02$, $t = 0.04$, $t = 0.06$, $t = 0.08$ and $t = 0.1$ (days) at 128^2 resolution for the second-order (left) and fourth-order (right) algorithms.

In order to diagnose this issue, a very short time integration (0.1 days) was examined to study the initial evolution of the divergence and height fields. The results of this analysis are displayed in figure (7.5). In this figure, it can be seen that during the evolution of the flow, by day 0.1, the height field is different between the two algorithms.

To understand the reason for this difference, the divergence fields were examined for the same time periods, shown in figure (7.6). This figure indicates that there may a problem, at least in the initialisation, of one of the algorithms. The results below indicate that the problem lies within the fourth-order algorithm. To determine the nature of this variation in divergence fields, we carried out a convergence study for both algorithms at early times. Figure (7.7) shows time $t = 0.02$ for varying resolutions. Clearly seen is that upon increasing resolution, the second-order algorithm converges almost immediately, whereas the number of contours in the fourth-order algorithm simply reduce by a factor of two on each doubling of resolution.

Figure (7.8) gives the full picture, showing that, at $t = 0.1$, the fourth-order algorithm is tending to converge to the results of the second-order algorithm, which shows much faster convergence. A. Mohebalhojeh (private communication) believes that the error stems from the calculation of γ from equation (5.1) initially, which appears to be much more sensitive in the fourth-order algorithm. This is currently under investigation.

In subsequent chapters, a ramped initialisation procedure is used in the fourth-order algorithm, thereby avoiding any potential error arising from the discretisation of equation (5.1).

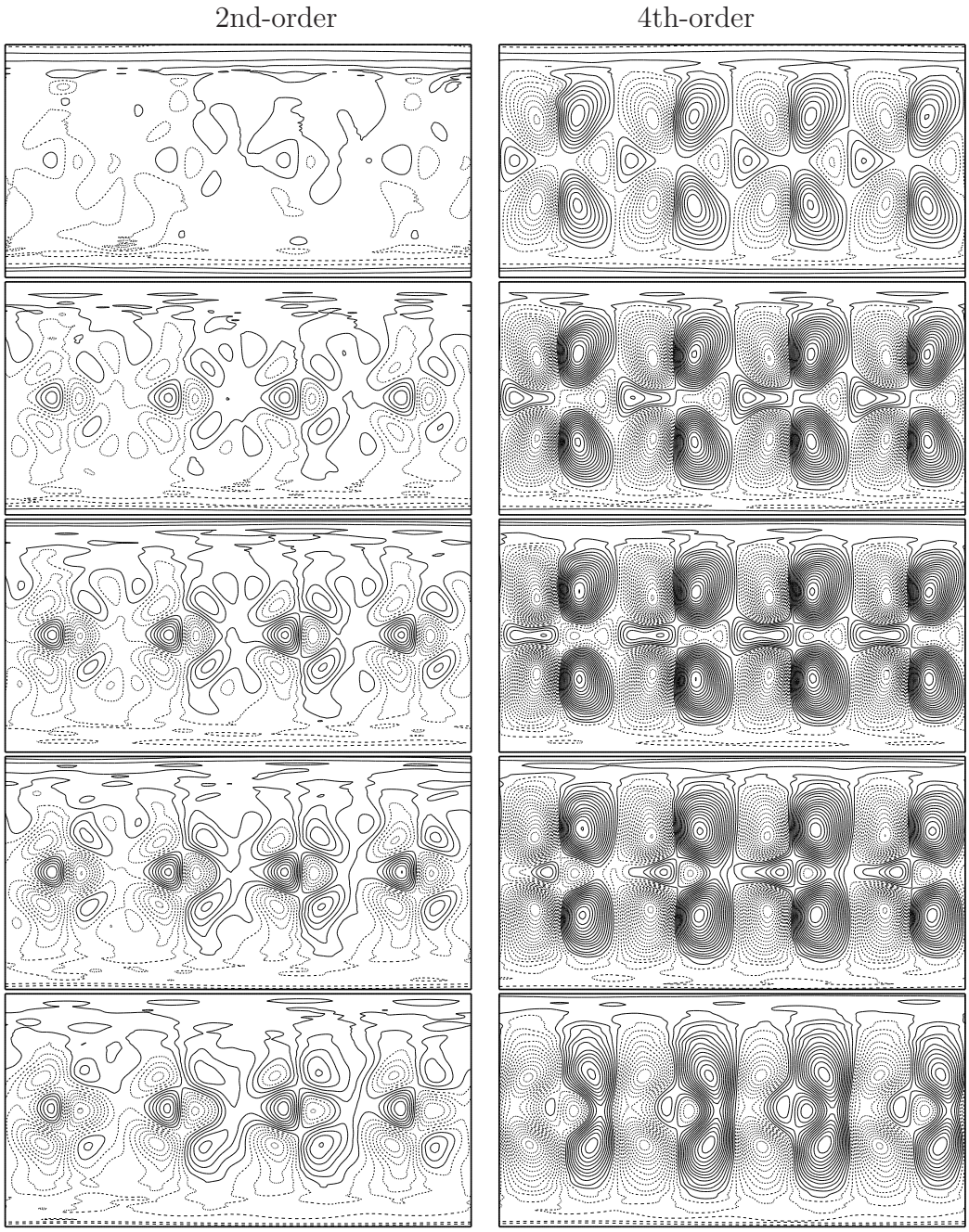

FIGURE 7.6: Comparison of the divergence field for $t = 0.02$, $t = 0.04$, $t = 0.06$, $t = 0.08$ and $t = 0.1$ (days) at 128^2 resolution for the second-order (left) and fourth-order (right) algorithms.

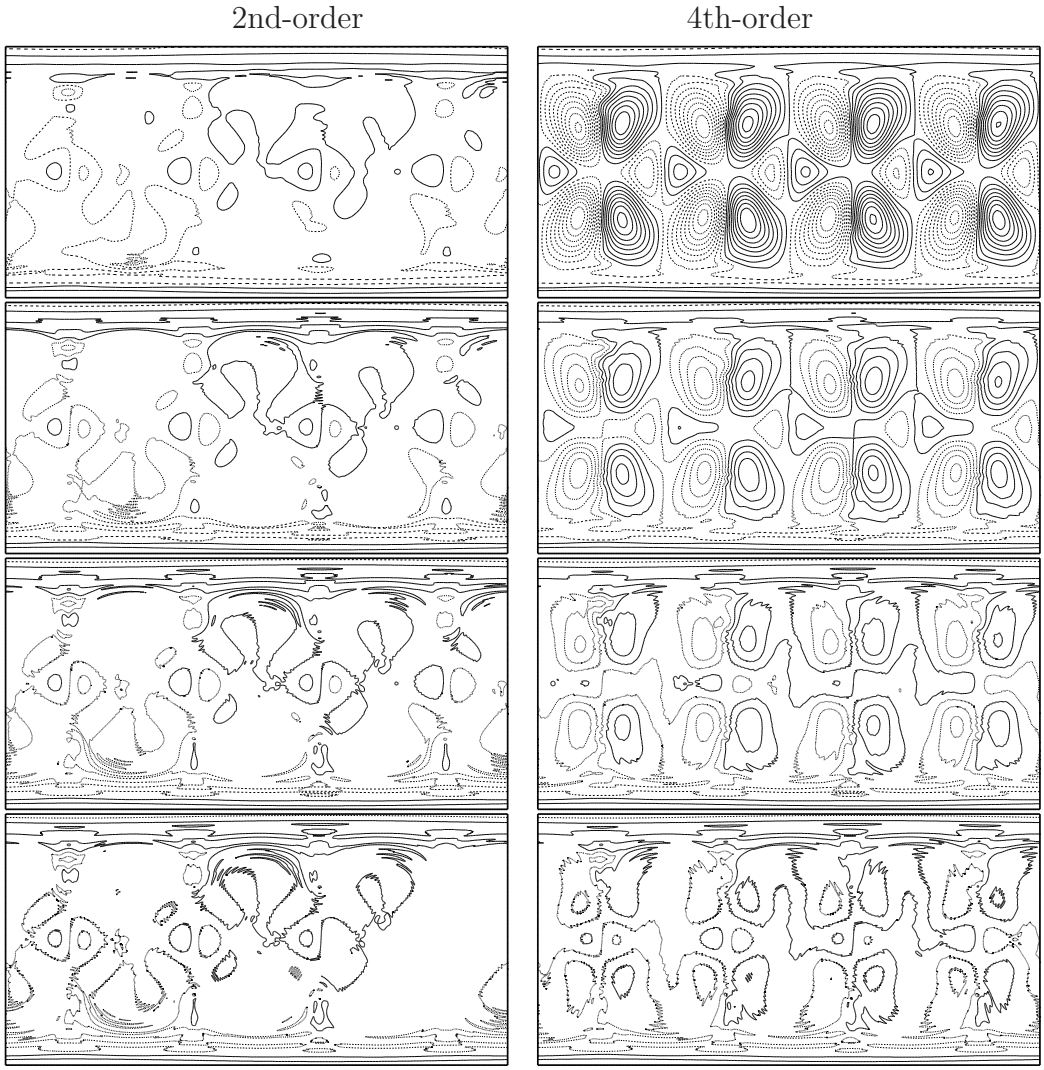

FIGURE 7.7: Comparison of the divergence field for $t = 0.02$ (days) for 128^2, 256^2, 512^2 and 1024^2 resolution for the second-order (left) and fourth-order (right) algorithms.

7.1.2 Energy and momentum conservation

We next compare the second and fourth-order CASL algorithms in terms of their global conservation properties. The energy, E, and angular momentum (neglecting momentum due to rigid rotation), J, about the Earth's axis are conserved in the absence of forcing and dissipation. They are given by the double integrations over

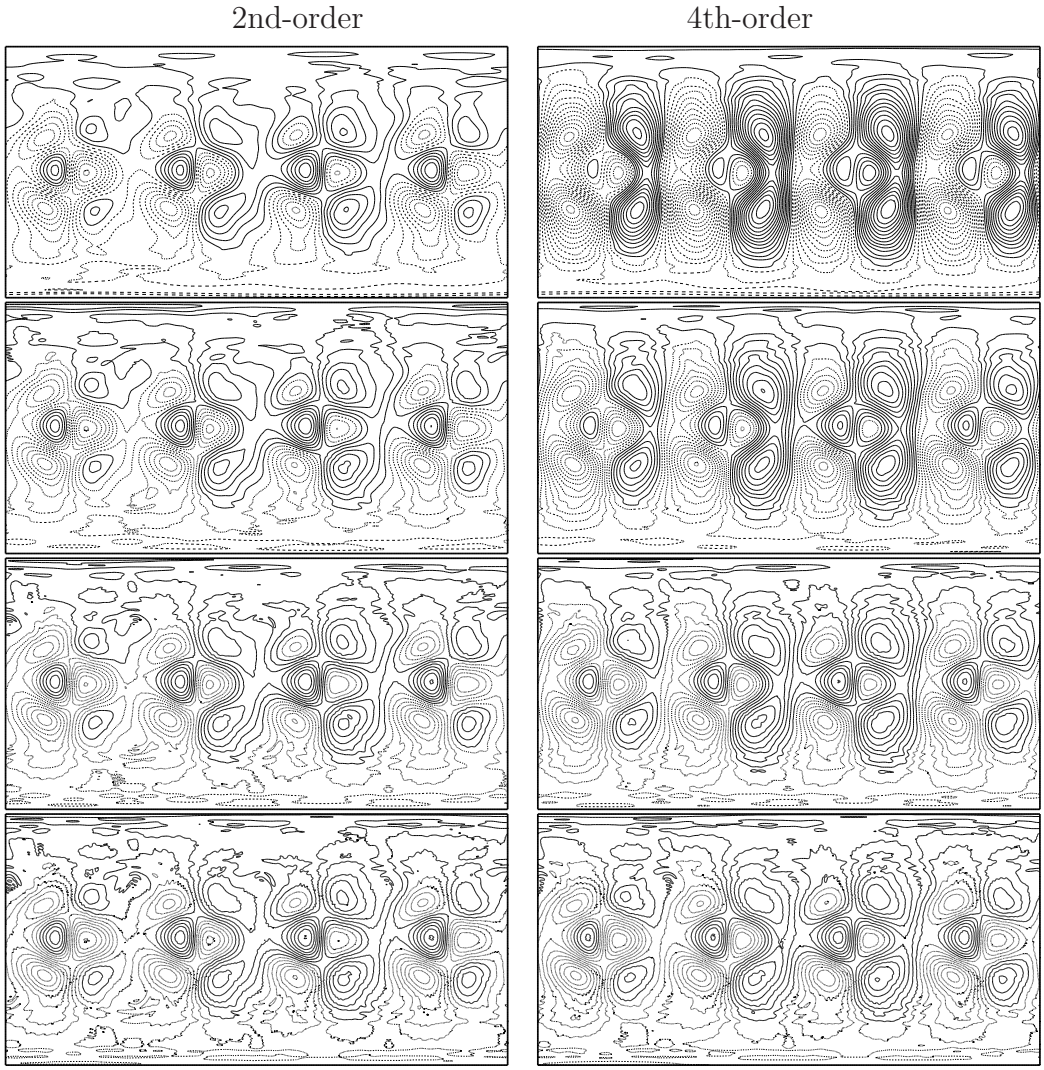

FIGURE 7.8: Comparison of the divergence field for $t = 0.1$ (days) for 128^2, 256^2, 512^2 and 1024^2 resolution for the second-order (left) and fourth-order (right) algorithms.

the domain Ω, as follows,

$$E = \frac{1}{2}\int\int\left((1+\tilde{h})|u|^2 + c^2\tilde{h}^2\right)d\Omega\,, \tag{7.1}$$

$$J = \int\int\left((1+\tilde{h})u + \Omega_E\tilde{h}\cos\phi\right)d\Omega\,. \tag{7.2}$$

We also non-dimensionalise these quantities by the planetary radius and one day and so all graphs relating to these values do not carry dimesnions. Figure (7.9) shows the variation of energy and angular momentum over the 20 day integration in

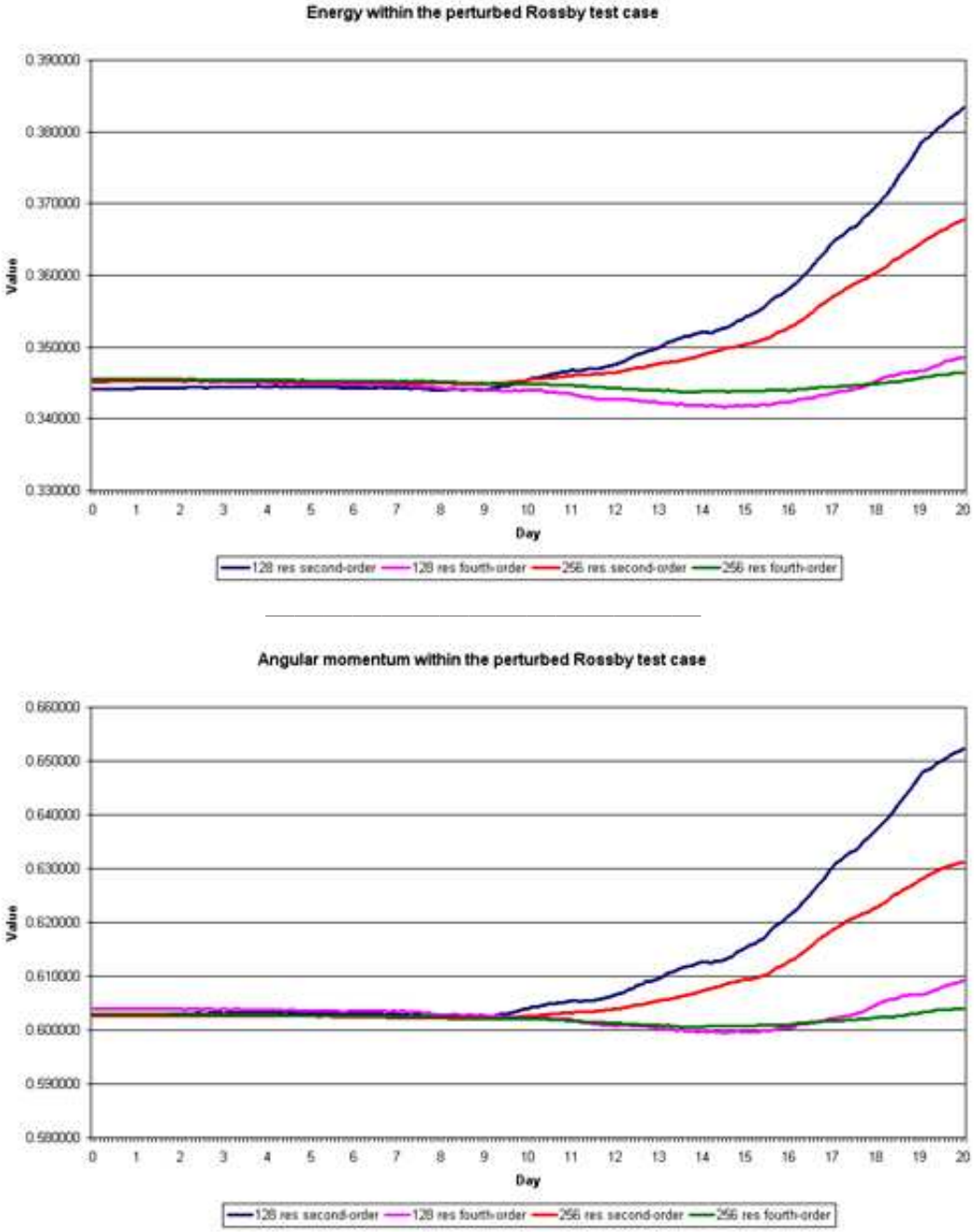

FIGURE 7.9: Comparison of energy (top) and momentum (bottom) values for the second and fourth-order CASL algorithms at 128^2 and 256^2 resolutions for the perturbed Rossby wave case, introduced in Chapter 4.3.

Algorithm	**Energy** $t = 0$	**Energy** $t = 20$	**% Increase**
128^2 $\mathrm{CA}^{2-fg}_{\delta,\gamma}$	0.344125	0.383368	11.4
256^2 $\mathrm{CA}^{2-fg}_{\delta,\gamma}$	0.345203	0.367717	6.5
128^2 $\mathrm{CA}^{4-hg}_{\delta,\gamma}$	0.345404	0.348580	0.9
256^2 $\mathrm{CA}^{4-hg}_{\delta,\gamma}$	0.345526	0.346479	0.3
	Momentum $t = 0$	**Momentum** $t = 20$	**% Increase**
128^2 $\mathrm{CA}^{2-fg}_{\delta,\gamma}$	0.602741	0.652292	8.2
256^2 $\mathrm{CA}^{2-fg}_{\delta,\gamma}$	0.602640	0.631128	4.7
128^2 $\mathrm{CA}^{4-hg}_{\delta,\gamma}$	0.603904	0.609155	0.9
256^2 $\mathrm{CA}^{4-hg}_{\delta,\gamma}$	0.602933	0.603962	0.2

TABLE 7.3: Conservation of energy and momentum for second and fourth-order CASL algorithms for a 20 day Rossby test case at 128^2 and 256^2 resolutions.

the perturbed Rossby wave test case, for both $\mathrm{CA}^{2-fg}_{\delta,\gamma}$ and $\mathrm{CA}^{4-hg}_{\delta,\gamma}$. Conservation at resolutions of 128^2 and 256^2 has been analysed to assess the impact fourth-order finite differencing has on these diagnostics. As can be seen, the lower 128^2 resolution $\mathrm{CA}^{4-hg}_{\tilde{h},\delta}$ shows better conservation properties in E and J than even the 256^2 resolution $\mathrm{CA}^{2-fg}_{\delta,\gamma}$.

Table (7.3) gives the initial and final values of energy and angular momentum, corresponding to figure (7.9), and the improvement to conservation for fourth-order compact finite differencing can clearly be seen.

As an additional note, it is worth including the difference that the Broutman filtering on the Laplacian within the algorithm makes on the conservation of energy and angular momentum. At 128^2 resolution, without this filtering, the energy within $\mathrm{CA}^{2-fg}_{\delta,\gamma}$ increased by 11.5% and $\mathrm{CA}^{4-hg}_{\delta,\gamma}$ increased by 1.5%. The angular momentum also increased by 8.2% and 1.2% for the respective second and fourth-order algorithms. The major increase in conservation properties, however, becomes clear at higher resolution where, at 256^2 resolution without filtering, energy increased

by 7.4% and 0.6% for second and fourth-order algorithms respectively and momentum increased by 5.4% and 0.5%. As table (7.3) shows, with the relevant filtering in place, the increases in both energy and momentum values are greatly reduced over the 20 day integration, especially at higher resolutions.

7.2 OPV balance

Bringing the points from Chapters 1.5.1 and 1.5.2 together and using a technique known as *Optimal PV* balance (OPV balance), [18, 74], it has been shown that a system remains close to balance if the initial conditions are close to balance, [18, 45]. In observed geophysical flows, balance is thought to hold to a high degree for meso and large-scale fluid dynamics, where the fluid motion is significantly weaker than the Earth's rotation and is also strongly stratified, [45].

In order to create initial "balanced conditions" for the models the fields are first set to zero. Then, with the PV contours held fixed, the PV carried by each fluid particle (or contour) is multiplied by a ramp function, varying smoothly from 0 to 1, during each (non-physical) integration time. The fluid particles are allowed to move freely after the first forward ramp and the conditions will vary at the end of each backwards integration, with remaining non-zero motions due to internal gravity waves (IGWs). These IGW motions are then removed for the forward integration. Any difference in the PV distribution at the end of the forward integration is removed by resetting it to the actual PV configuration. This is repeated until convergence (when maximum differences in $\tilde{h}$ between successive forward integrations is less than 10^{-7}), with the particle distribution thus found for the start of the ramp period, usually in 6 to 8 cycles, [17, 74].

The period of this PV ramping was analysed in order to build a picture of how this affected the fields. To demonstrate simply the concept of OPV balance within the

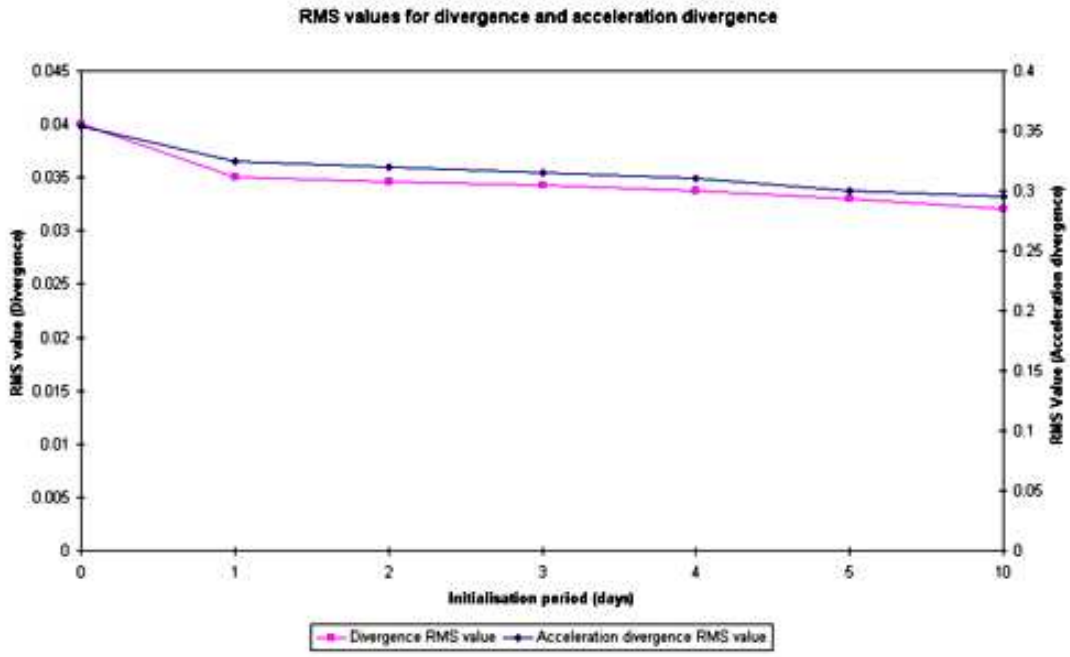

FIGURE 7.10: RMS values for the divergence (pink) and acceleration divergence (blue) fields for varying initialisation periods. Please note the different scale for each field.

SWEs for CASL, the single vortex patch test case from Chapter 3.1.2 was used at 128^2 resolution, with a single vortex patch of width 15° placed at 15° latitude and 0° longitude.

Analysis of the divergence and acceleration divergence fields, since such fields tend to be less balanced than the primary fields of height and velocity, was carried out and RMS values of these fields were calculated for the initialisation periods (days) 0.1, 1, 2, 3, 4, 5 and 10. The results of these tests are shown in figure (7.10). As can be seen a plateau is reached after 2 to 3 days, consistent with previous findings. Excessively long ramp periods cannot be used in general due to the winding up of PV contours. In this example, the PV patch is superimposed on a background rigid rotation and during the backward integration this patch winds the planetary vorticity contours around it. The forward integration then unwinds the vorticity, however excessively long ramp periods cause a loss of convergence in

the procedure.

Chapter 8

Equatorial atmosphere and ocean dynamics

8.1 Global atmospheric circulation

It was noted by sailors navigating the globe that, for approximately 5° latitude either side of the equator, there is very still, rising air in this region. This led to the term "doldrums" for the equatorial region. Solar radiation warms near surface air over the Earth's equator, leading to warmer air rising over this area. This rising air then moves into the cooler zone of higher latitudes, which naturally (from continuity) cools and sinks, moving at lower altitudes back towards the equator.

Therefore, approximately 20° to 30° either side of the equator, blowing towards the lower pressure doldrums, are the trade winds, named for their ability to quickly propel ships as they steadily blow at about 12 miles per hour. In the Northern hemisphere the trade winds blow from the north-east, whereas the Southern hemisphere trade winds blow from the south-east. This convergence of trade winds leads us to the modern term for the equatorial region, the Inter-Tropical Convergence

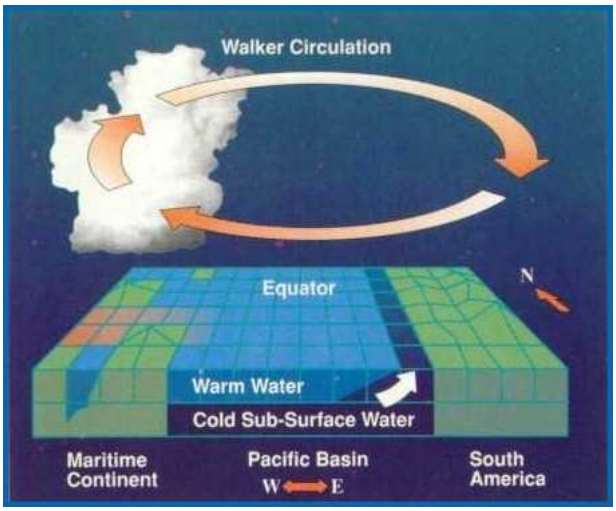

FIGURE 8.1: Diagram showing the Walker circulation.

Zone (hereafter ITCZ). This circulation dominates the weather patterns seen in the ITCZ, with warm, rising equatorial air leading to significant precipitation.

8.1.1 Walker circulation

East to west, over the Pacific ocean, there is a circulation of air along the equator caused by the pressure gradient between the cool, dry, high pressure system over the eastern Pacific and the warm, wet, low pressure system over the western Pacific. The low pressure system causes warm air to rise over the west, whereas the high pressure system leads to cooler air sinking over the east. This generates an overturning flow which is west to east at high altitudes and east to west at low altitudes. An image of this circulation can be seen in figure (8.1)[1]. This circulation is known as the Walker circulation, named after the English physicist Sir Gilbert Walker, who theorised the southern oscillation phenomenon, which will be discussed in Chapter 8.3.

[1]Figures 8.1 to 8.4 courtesy of nsipp.gsfc.nasa.gov

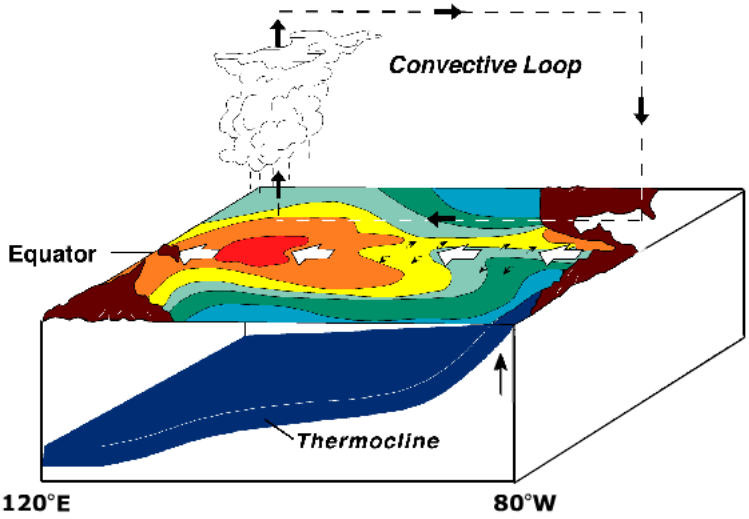

FIGURE 8.2: Diagram showing the ocean thermocline level and Walker circulation during normal conditions.

"It is a natural supposition that there should be in weather free oscillations with fixed natural periods, and that these oscillations should persist except when some external disturbance produces discontinuous changes in phase or amplitude." — Sir Gilbert Walker, [75].

8.2 Ocean temperature and circulation

The ocean surface itself absorbs much of the sun's radiation, heating the surface layer. Below this surface layer, however, the temperature drops rapidly and where this occurs we have the observed transition depth, where the temperature suddenly drops, known as the thermocline [29, 33]. Along this temperature gradient there is significant mixing, where cold, deep fluid interacts with warm surface fluid [69, 70].

The trade winds across the Pacific ocean in turn interacts with the ocean surface, giving the observed sea surface temperature (SST), with warmer SSTs seen in the West. How much the trade wind stress affects the SST can be quantified by

observing the thermocline depth across the Pacific, shown, including the observed Walker circulation during normal conditions, in figure (8.2). The interface between warm surface fluid and cold deep ocean fluid means that a thermocline near the surface is mixing more cold, deep fluid with that near the surface (hence cooler SST) than a thermocline at lower depth, where less surface mixing occurs hence warmer SST.

As shown in figure (8.2), the normal thermocline level across the Pacific creates ocean upwelling off eastern coastlines. This means that nutrient rich, cold water is brought to the surface, increasing fish stocks, vital to those areas. It has been noted that in a recent paper in *Nature* that the Walker circulation may be decreasing [73]. This, as we shall see in the following chapter, may lead to more violent and unpredictable weather events and declining fish stocks.

8.3 The ENSO phenomenon

8.3.1 Introduction

In the following chapters another important phenomenon will be investigated numerically, namely the generation and propagation of a special type of gravity wave — the equatorial Kelvin wave, [7, 30, 39]. These waves are key to the El Niño Southern Oscillation phenomenon (ENSO). In the ENSO phenomenon, the SST in the East Pacific sea is affected by a positive feedback term due to Kelvin waves. This system is very complex, and was raised at a conference for collaboration in mathematical geosciences and ocean dynamics in Breckenridge, USA 2006 by Eli Tziperman, see for example [20, 69, 70].

A heuristic understanding of ENSO can be discussed by using basic models, e.g. the delayed oscillator model [4, 66], to show the feedback effects of different aspects

within ENSO. We shall be concentrating on one effect, namely Kelvin waves, which propagate along the equator, as it is most relevant to the previous work within the CASL model. This effect highlights the importance of gravity wave modelling and how improving full global circulation models, in a similar manner, may gain more insight into less well understood phenomena. Remarkably, such basic models can prove to be extremely useful in understanding climate variability. Once the phenomena present are understood within an idealised model, then more complex models may be used for a more rigorous study. Most surprising is the accuracy of basic models when relating to observational data, in spite of the complexity of a real climate system, for example with reference to TOPEX/Poseidon satellite data in [2, 40]. This shows the systems observed are largely governed (at least at large scales) by a relatively simple low order set of dynamics, often showing little deviation from a "balanced" flow [45].

I have chosen to include a pedagogical description of the ENSO model below[2]. This is not strictly a requirement for the test case to be outlined for the CASL model, but it will show how even the most idealised test case can include complex and real life phenomena, which may be used to further understand important dynamical systems.

First, let us consider the mean states involved in this phenomena, which, for the ENSO model, include both the ocean and atmospheric dynamics, detailed in the introduction to this chapter. The mean trade winds are easterly, with warm air rising over the west Pacific and cold air sinking over the east Pacific. The easterly trade wind stress causes warm water to collect in the east Pacific which leads to an east-west gradient in SST, shown for August 2006 in figure (8.3). This, in turn, causes feedback effects in the Walker circulation and mean wind stress.

[2]For more advanced detail of ENSO, see http://www.pmel.noaa.gov/tao/elnino/nino-home.html from which the El Niño images in this thesis have been taken

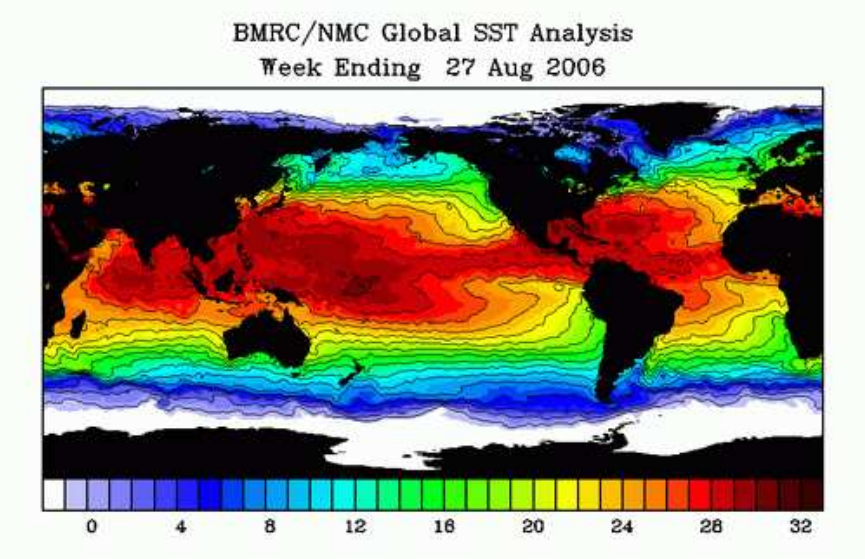

FIGURE 8.3: The Sea Surface Temperature showing the East-West temperature gradient across the equatorial region of the Pacific Ocean.

8.3.2 Building the El Niño mechanism

The thermocline and wind stress play a very important part in ENSO variations around the mean state; SST changes during ENSO are accompanied by a decline in the Walker circulation, which weakens the easterly trade winds. This starts a cycle of events which play the main part in El Niño and La NiÑa (the cooling mode of ENSO) events. Figure (8.4) shows a graphical representation of the observed thermocline and Walker circulations during an El Niño event and a La NiÑa event.

During El Niño the decline in easterly trade winds leads to a depression in the thermocline depth in the east Pacific and rise in thermocline depth in the west. The subsequent reduced upwelling in the east leads to less nutrient rich, cold water mixing at the surface, meaning fish stocks are greatly reduced, as mentioned. Precipitation moves eastward with the warmer SST, often leading to a drought in Indonesia and Australia and subsequent flooding in Peru.

The El Niño phenomenon tends to peak towards the end of the year and there

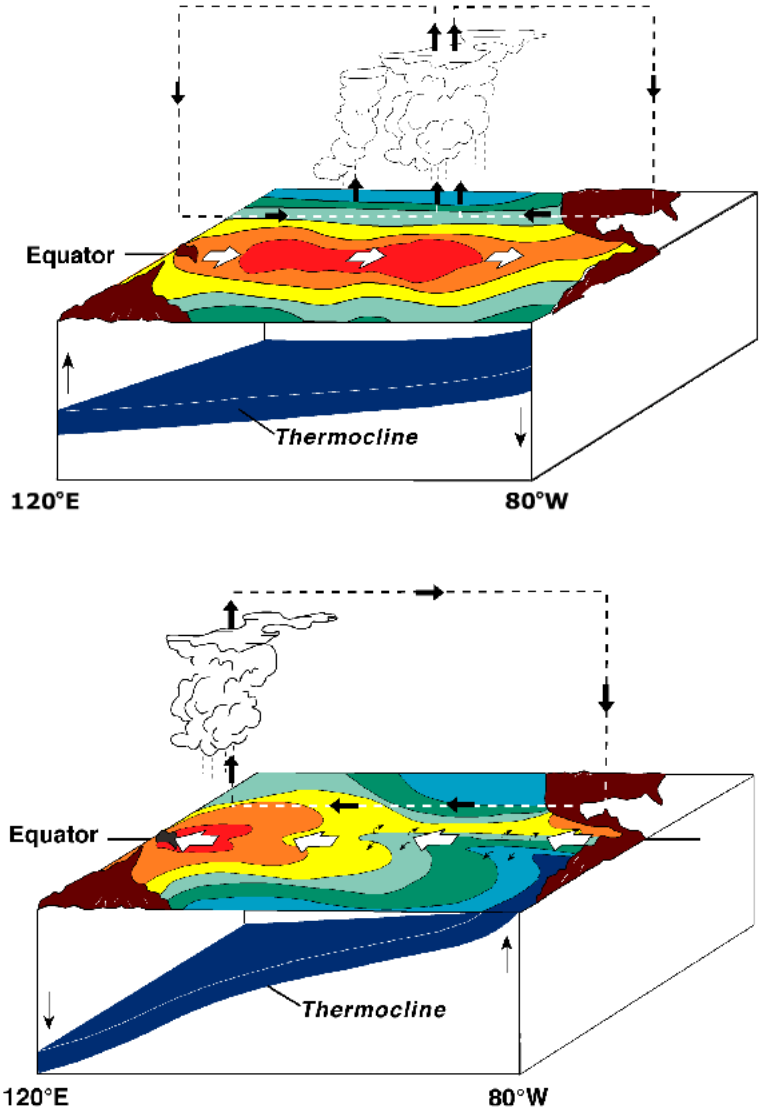

FIGURE 8.4: Graphical comparison of the thermocline state during an El Niño event (top) and then a La NiÑa event (bottom), including the corresponding Walker circulations in the atmosphere.

is a several year time scale between events (the reasons for which are still not fully understood). This is a world-wide event: the effects of ENSO are reflected in severe global weather events, typically with intense wet weather in America and drought, with subsequent fires, in Australia. To put into perspective the importance of understanding and modelling these events, the (poorly predicted) 1997-1998 El Niño event was responsible for fires, droughts and floods which killed

21,000 people in Indonesia [78], and the financial impact was estimated to be in the region of $32 billion (source: BBC News August 2001).

8.3.3 Ending the El Niño event

In its mean state, the easterly wind forcing is balanced by an ocean pressure gradient, due to the thermocline near to the surface, in the East Pacific (i.e. the mean state SST is cooler in the East, resulting in what is called the cold tongue). Due to the weakening of the trade winds, outlined in Chapter 8.3.2, the thermocline depth changes across the Pacific. This creates both Kelvin waves (which deepen the thermocline depth, inducing an SST heating) and Rossby waves (which have the opposite effect) and this is physically manifested in a "wavy" thermocline layer.

This system of Rossby and gravity waves plays the main part in the delayed oscillator mechanism theory [4, 66], whereby the "warm" Kelvin waves are restricted to the equator, travelling towards the east at the start of the El Niño. The slower, "cold" Rossby waves travel a few degrees off the equator towards the west and will eventually reflect off the western boundary. Then, travelling east as "cold Kelvin" waves, they will eventually start a La NiÑa event, meaning the El Niño mechanism stops. The amplitude of these waves are typically tens of meters, with a wavelength of between 100 and 1000km. The Kelvin waves cross the Pacific in 2 months, where the Rossby waves take around 8 months and the La NiÑa event, occurring at that time, ends the system of events. This system, although governed by a relatively simple set of dynamics, is still poorly calculated, both by statistical and numerical methods and, since there are such widespread climatological

(and financial) implications, it is a vitally important event to isolate and understand why there seems to be a certain random factor involved in the phenomenon, [20, 70].

Chapter 9

Generation and detection of Kelvin waves

The following chapter combines the previous work on the CASL algorithm and observed gravity waves, detailed in the previous chapter. Here the fourth-order CASL algorithm is used to diagnose equatorial Kelvin waves observed in the ENSO phenomenon and references to other work on gravity waves will introduce the reader to the complex links between the ENSO phenomenon and Kelvin waves.

9.1 Analysing equatorial waves

Kelvin waves can only travel along the equator, meaning they have no meridional velocity ($v = 0$). The shallow-water equations in a local Cartesian coordinate

system reduce to

$$\frac{\partial u}{\partial t} = -c^2 \frac{\partial \tilde{h}}{\partial x}\,, \tag{9.1}$$

$$fu = -c^2 \frac{\partial \tilde{h}}{\partial y}\,, \tag{9.2}$$

$$\frac{\partial u}{\partial x} = -\frac{\partial \tilde{h}}{\partial t}\,, \tag{9.3}$$

for a small-amplitude (linear) disturbance to a state at rest.

Combining equations (9.1) and (9.2), one obtains

$$\frac{\partial^2 u}{\partial t^2} = c^2 \frac{\partial^2 u}{\partial x^2}\,, \tag{9.4}$$

which has a solution of the form $u = E(y)F(x \pm ct)$, with E and F arbitrary functions. The only physical solution, following [30], is that of an eastwardly propagating gravity wave, $u = E(y)F(x - ct)$, with $\tilde{h} = c^{-1}E(y)F(x - ct)$, for consistency with equation (9.3). The y dependence, $E(y)$, is determined from equation (9.2), which, with $f = \beta y$ near the equator implies that $\beta y E = -c\frac{dE}{dy}$, whose solution is of the form

$$E(y) = Ae^{-y^2/2\lambda^2}\,, \tag{9.5}$$

where $\lambda = \sqrt{c/\beta}$ is the equatorial Rossby deformation length. Hence the Kelvin wave is trapped near the equator.

In the oceans, at the thermocline a typical wave speed [30] is

$$c = \sqrt{g'H} \approx 2.2\,\mathrm{ms}^{-1}\,, \tag{9.6}$$

so $\lambda \approx 300$km, or about 3° of latitude.

In order to diagnose the Kelvin waves at the equator, a topographic structure can be placed near the equator in order to generate gravity waves in the flow over it. Examining the tendency of the fluid depth $\partial\tilde{h}/\partial t$ along the equator will allow us to see the waves, without seeing the stationary topographic structure itself. However, to distinguish Kelvin waves $(u_{kw}, \tilde{h}_{kw})$ from other types of motion present, we minimise, in an energy norm sense, the differences $u - u_{kw}$ and $\tilde{h} - \tilde{h}_{kw}$. That is, we minimise

$$\frac{1}{2}\int_0^{2\pi} d\lambda \left[\left(\frac{\partial u}{\partial t}(\lambda, 0, t) - \frac{\partial u_{kw}}{\partial t} \right)^2 + \left(\frac{\partial v}{\partial t}(\lambda, 0, t) \right)^2 + c^2 \left(\frac{\partial \tilde{h}}{\partial t}(\lambda, 0, t) - \frac{\partial \tilde{h}_{kw}}{\partial t} \right)^2 \right] , \tag{9.7}$$

while requiring $\tilde{h}_{kw} = \tilde{u}_{kw}/c$, the relation satisfied by all Kelvin waves. Here, we minimise the function $\partial\tilde{u}_{kw}/\partial t$.

The solution is obtained by taking the functional derivative with respect to $\partial u_{kw}/\partial t$:

$$-\left(\frac{\partial u}{\partial t} - \frac{\partial u_{kw}}{\partial t} \right) - c\left(\frac{\partial \tilde{h}}{\partial t} - \frac{1}{c}\frac{\partial u_{kw}}{\partial t} \right) = 0 , \tag{9.8}$$

whose solution is

$$\frac{\partial u_{kw}}{\partial t} = c\frac{\partial \tilde{h}_{kw}}{\partial t} = \frac{1}{2}\left(\frac{\partial u}{\partial t} + c\frac{\partial \tilde{h}}{\partial t} \right) . \tag{9.9}$$

For pure Kelvin waves and nothing else, this solution is exactly what one would expect.

9.2 Topography

As indicated in the previous chapter, gravity waves are likely to be generated when flow passes over topography. Taking an idealised case of rigid body rotation on the

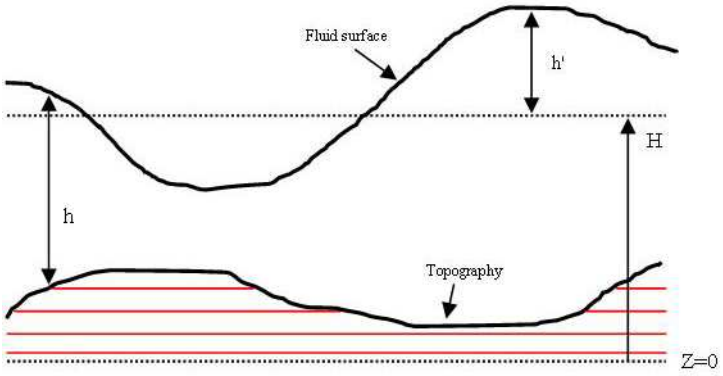

FIGURE 9.1: Complex topography.

sphere, a Gaussian topographic distribution can then be placed at varying latitudes in order to examine the gravity wave production arising from the interaction between the fluid motion and the topography.

Figure (9.1) gives an example of more complex topography, which may be taken as an uneven ocean base, or mountain range.

This is an important piece of the puzzle for the CASL algorithm. In global circulation models, topography has a major influence on the flow and as such its addition is essential to modelling realistic flows.

Within the CASL algorithms, there is a topographic contribution to both the height, divergence and ageostrophic tendencies, arising from the differentiation of the momentum equation (1.1), expressed as

$$\frac{\mathrm{D}\mathbf{u}}{\mathrm{D}t} + 2\boldsymbol{\Omega}_E \times \mathbf{u} = -\boldsymbol{\nabla}(gh_{\mathrm{tot}})\,, \tag{9.10}$$

where gh_{tot} is the hydrostatic pressure and the total free surface height, h_{tot}, is split into the fluid depth, h, and the height prescribed by the topography, h_{b}, as follows

$$\frac{\mathrm{D}\mathbf{u}}{\mathrm{D}t} + 2\boldsymbol{\Omega}_E \times \mathbf{u} = -\boldsymbol{\nabla}(g(h + h_{\mathrm{b}}))\,. \tag{9.11}$$

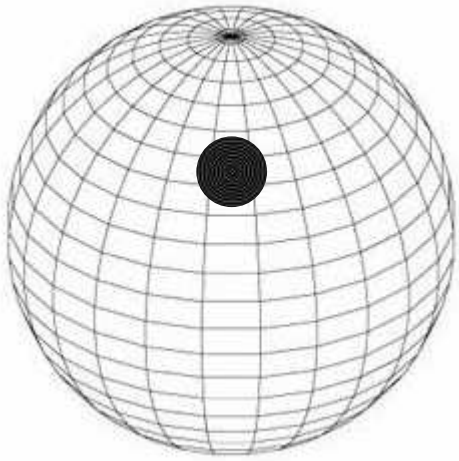

FIGURE 9.2: The Gaussian hill problem. The circle represents a topographic hill with Gaussian distribution, placed at various latitudes, as detailed.

The mass continuity equation is the same as before, since this equation arises from integrating $\boldsymbol{\nabla} \cdot \mathbf{u} = 0$ over the *fluid* depth h, not the full depth.

In a similar method to the OPV balance, described in Chapter 7.2, the topography is ramped up over a 3 day period to establish a non-trivial flow. This addition of topography within the momentum equation and the main SWE equations (1.10) to (1.12), generates a flow.

9.3 The Gaussian hill test case

As a simple test case, which will lead to the formation of gravity waves in a more natural manner, a topographic hill with a default Gaussian distribution of height half the fluid depth and a width of 15° was set up. This topographic structure is then placed at varying latitudes $\phi = 0°, 5°, 15°, 45°$... etc on a rigidly rotating flow with the PV given by the relation $q = 2\Omega_E z$. The flow in the absence of topography is therefore 0 in the rotating frame. A graphical representation is shown in figure (9.2).

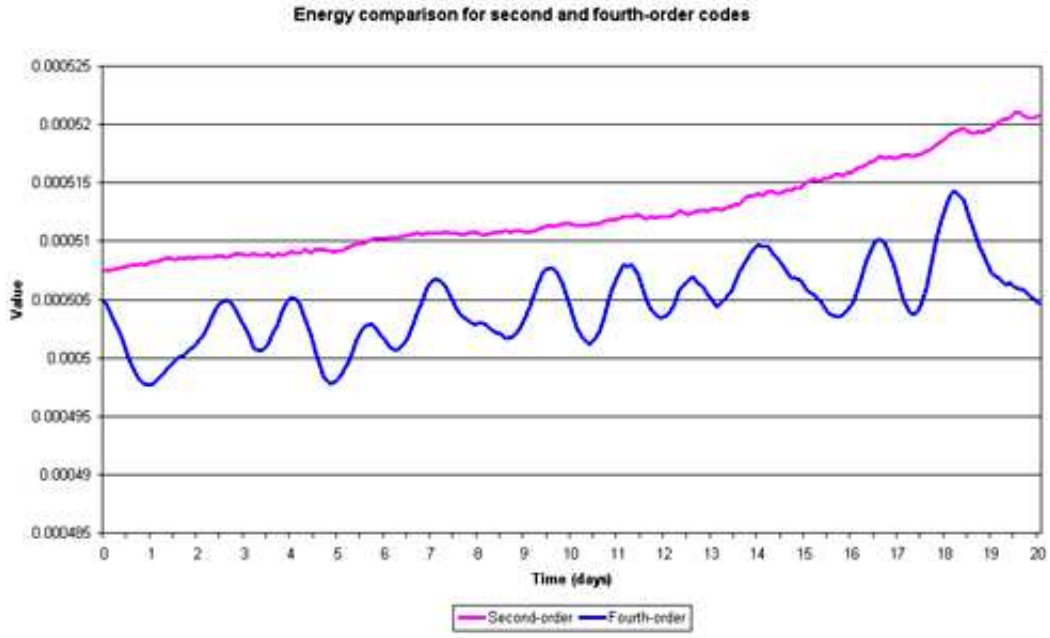

FIGURE 9.3: Comparison of the energy in second and fourth-order CASL simulations for a mid-latitude topographic hill.

9.4 Results

9.4.1 Finite differencing comparison

To begin with a reference case of a mid-latitude topographic hill, placed at 45° latitude, was run in order to compare the second and fourth-order numerical methods. To show the improvement in accuracy with the fourth-order algorithm, the values for energy and angular momentum were again looked at for both algorithms in this simple scenario.

The introduction of topography brings some changes to the calculation of the energy and momentum within the system - indeed the angular momentum is no longer conserved within the system, since the topography breaks the rotational symmetry of the domain. The changes to energy, introduced in equation (7.1), amount to replacing $\tilde{h}$ by $\tilde{h}(\tilde{h} + 2h_b)$.

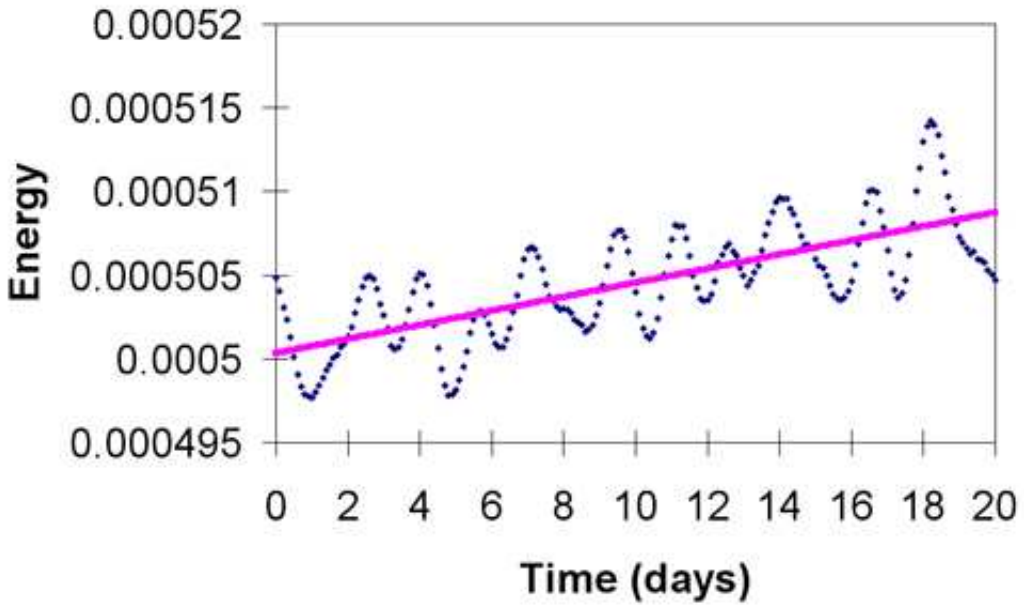

FIGURE 9.4: Regression analysis for the fourth-order energy over 20 days.

As shown in figure (9.3), the energy of the system is very well conserved in both second and fourth-order algorithms, due to the system being much smoother than the Rossby-Haurwitz test case already examined. Despite this, the fourth-order algorithm does show a slight improvement in conservation. Over the twenty day calculation, the energy in the second-order algorithm increases by 3%, whereas the fourth-order algorithm actually returns to the same value, showing no increase at all. The RMS error, calculated over the 20 days is 3.69×10^{-6} and 3.39×10^{-6} respectively, indicating a marginal increase in accuracy with the fourth-order finite differencing.

Figure (9.4) gives a more detailed view of the energy values from the fourth-order algorithm via a regression analysis. The energy values from the simulation are shown as the blue dots, while the pink line is the best-fit line via regression. As can be seen, the general trend of the data is an increase of 2% over 20 days.

Over a longer period of time, for the $\mathrm{CA}^{4-hg}_{\delta,\gamma}$ algorithm, the energy is nevertheless well conserved in this simple test case. During a 100 day run, with the hill placed

near in the equatorial region, the energy increases by 7%.

9.4.2 Effect of topographic placement on Kelvin waves

Next, the effects of placement of the topographic hill, with regards to the generation of equatorial Kelvin waves, shall be examined.

In order to excite Kelvin waves, it seems logical to place the hill near the equator. In the following, a hill placed at latitudes between 0° and 15° shall be examined. To visualise the Kelvin waves along the equator, the equatorial depth and velocity field values were saved and the tendencies computed in order to remove the mountain structure itself. Figure (9.5) gives a hodograph plot of the height tendency $\partial h_{kw}/\partial t$ at the equator, given a Gaussian hill structure placed at 5° latitude. Longitude goes from left to right and time (0-10 days) from bottom to top. This shows clearly the generation and propagation of Kelvin waves, with the diagonal lines visible having a slope equal to c, the phase speed of the Kelvin waves.

Figure (9.6) shows the dependence of Kelvin wave production on the location of the hill. Shown is the Kelvin wave amplitude (the RMS value of $\partial h_{kw}/\partial t$ along the equator) when the topographic hill is placed at 5° and then at 15°. The amplitude clearly reduces when the Gaussian hill is further from the equator. Figure (9.7) shows in more detail the sensitivity of the Kelvin wave to the placement of the hill. A hill placed directly over the equator generates the strongest Kelvin waves.

There is a marked reduction for a hill placement greater than 1° latitude and, as shown in figures (9.8) and (9.10) (showing the time evolution of the Kelvin wave amplitude for various hill locations), a hill placed at 45° still gives quantative wave production at the equator, appearing to mirror the low-latitude results.

FIGURE 9.5: Time plots of equatorial height tendency from a flow over a topographic hill placed at at 5° latitude.

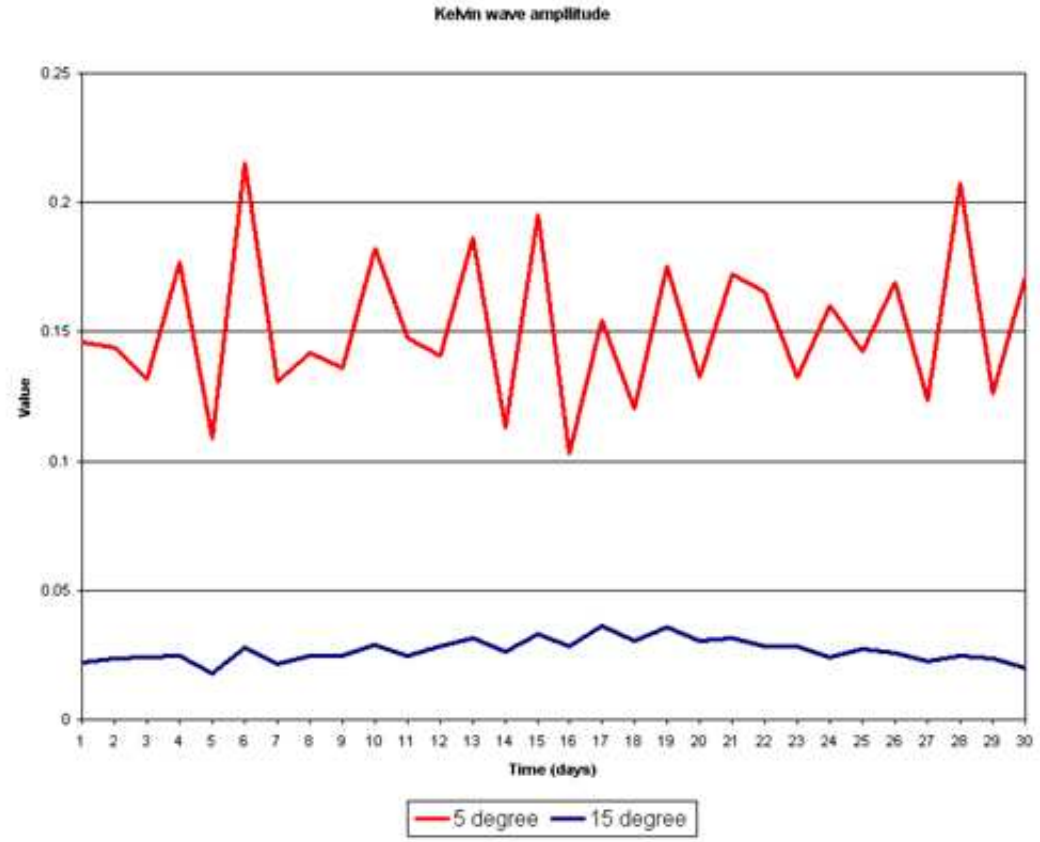

FIGURE 9.6: Kelvin wave amplitude with hill at 5° and 15° over a 30 day integration.

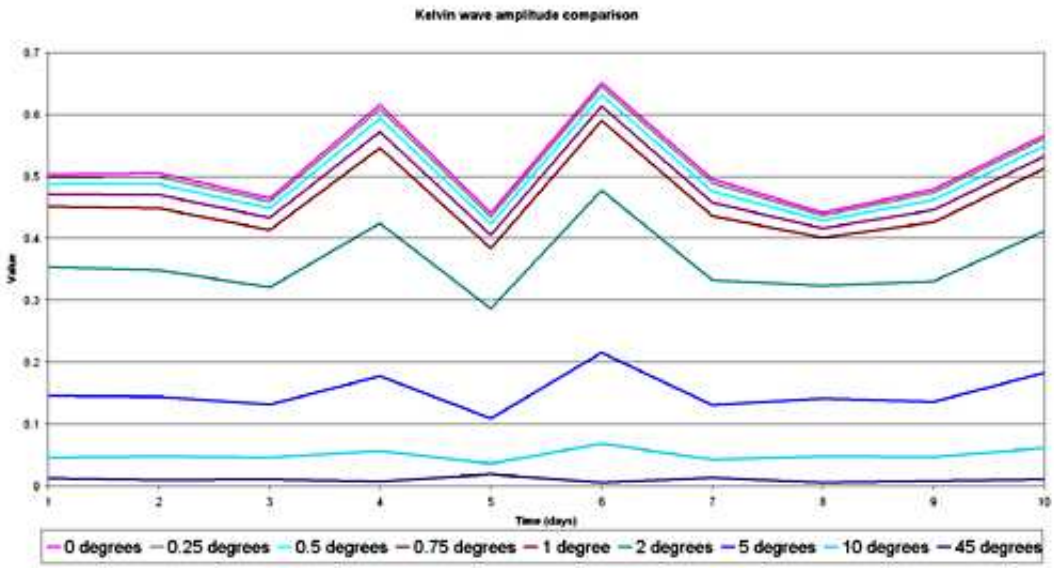

FIGURE 9.7: Kelvin wave amplitude with hill at selected latitudes from 0° to 45° as shown.

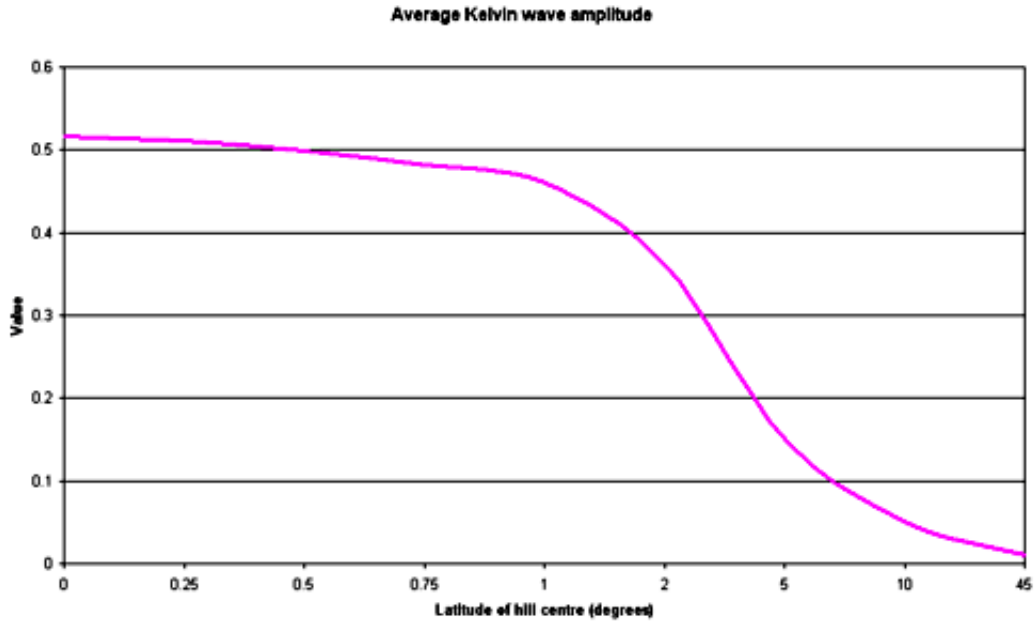

FIGURE 9.8: Average Kelvin wave amplitude with the hill at selected latitudes, showing the reduction in the amplitude of the Kelvin waves as the hill placement is varied as per figure (9.7).

Using the hodograph plots, we further investigate the results of Kelvin wave generation from mid-latitude and polar topography. Figure (9.9) shows how the structure of the equatorial waves changes with the position of the hill. At mid-latitude there is a very unstructured appearance to the Kelvin wave amplitude, however this again smoothes out as the hill moves to higher latitudes. It is possible that, at higher latitudes, there are other gravity waves being produced that are propagating from pole to pole. This may explain the "bands" seen in the equatorial hodograph plot with the hill at 85°.

To summarise, figure (9.10) shows the instantaneous amplitude of the Kelvin waves at the equator for a hill placed at latitudes 0° to 90° in 5° increments at the times stated. As can be seen, the amplitude rapidly drops as the topographic structure is placed further from the equator. However, the effects of Kelvin wave amplitude never completely diminish as the topography moves to higher latitudes. Indeed, Kelvin waves are enhanced for topography placed at high latitudes, with a local

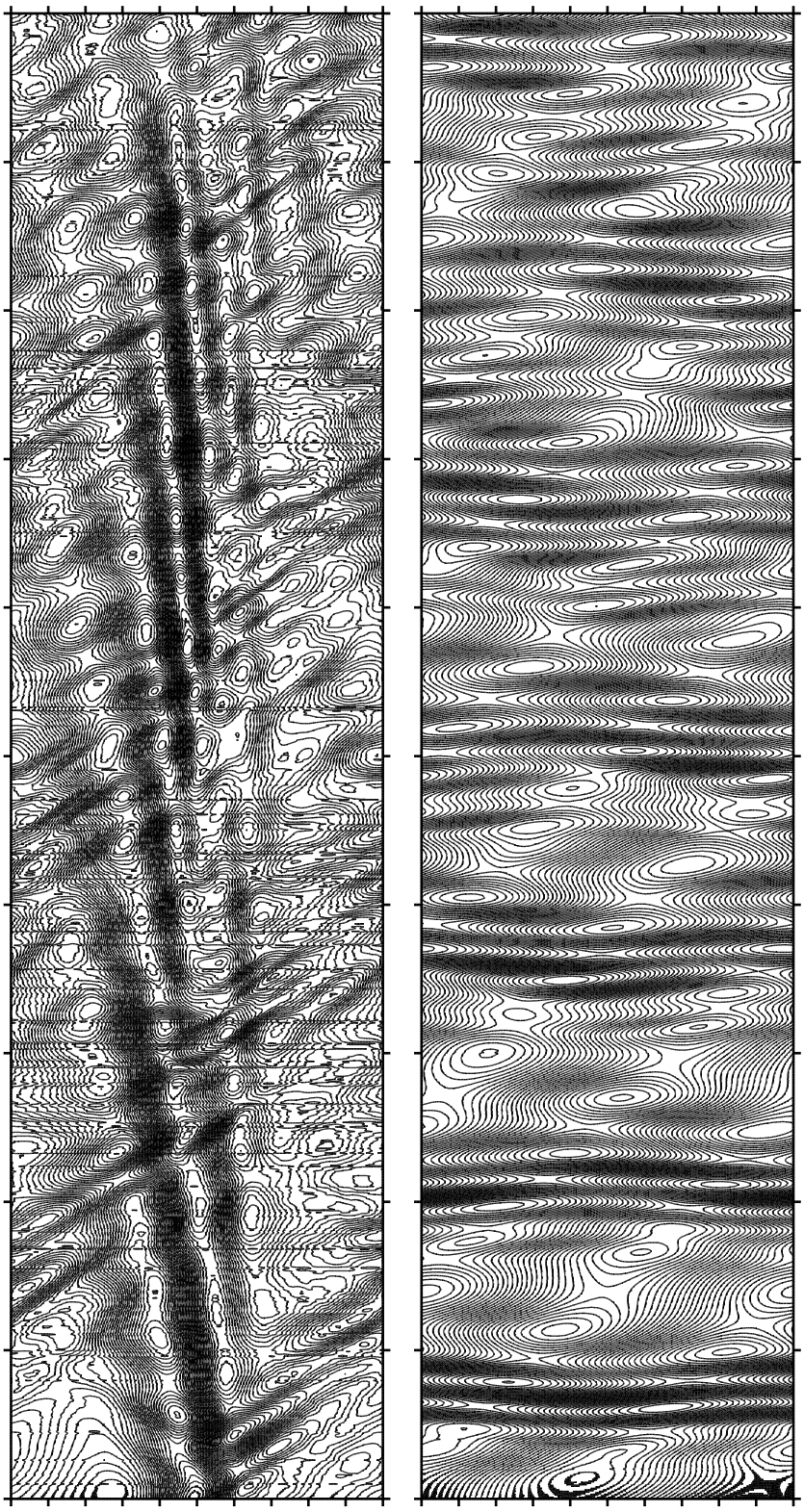

FIGURE 9.9: Time plots of equatorial height tendency from a flow over a hill placed at 45° and 85° latitude.

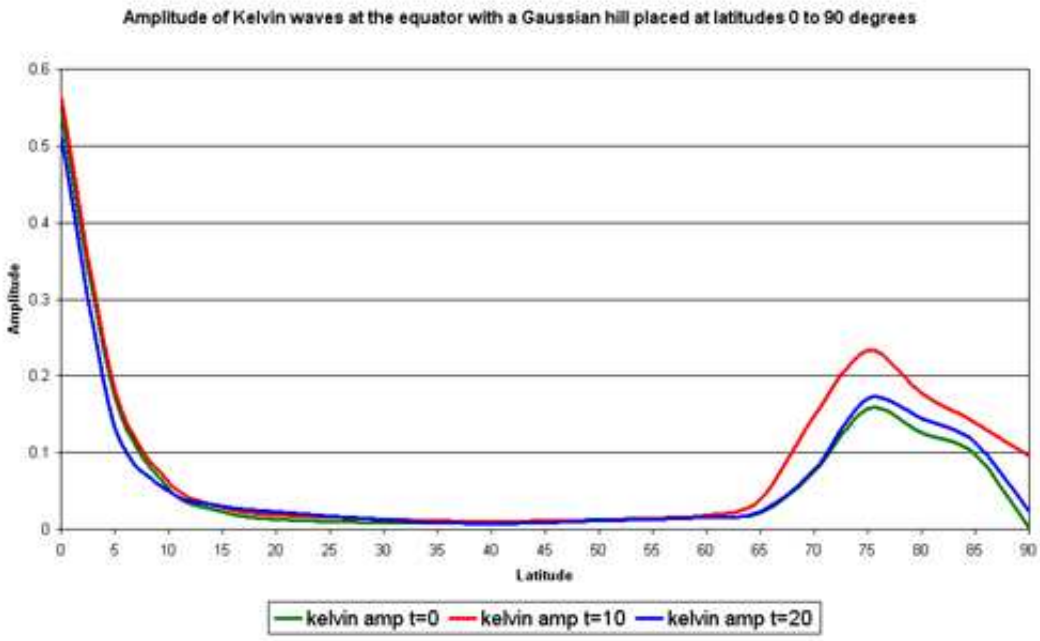

FIGURE 9.10: Kelvin wave amplitude at the equator with a Gaussian hill structure placed at the latitudes given along the x-axis at times $t = 0$, $t = 10$ and $t = 20$ (days).

maximum occurring for a hill placed at roughly 75°. Again, this is possibly due to gravity waves propagating from pole to pole.

This simple experiment shows there is a global impact of localised topography. In fact, the method of "growing" the topography used here may be analogous to a volcanic eruption (raising the fluid depth locally). The effects of volcanic eruptions have been documented to reduce the global average temperature of the Earth by around 0.5°C, due to the large quantity of aerosol emissions. More significantly, research by the University of Virginia has found that El Niño phenomena often occur in years when there is a volcanic eruption in the tropical region (roughly 23° either side of the equator), [62]. In our idealised study, we have found that equatorial topography induces the strongest Kelvin waves, a main feature of ENSO.

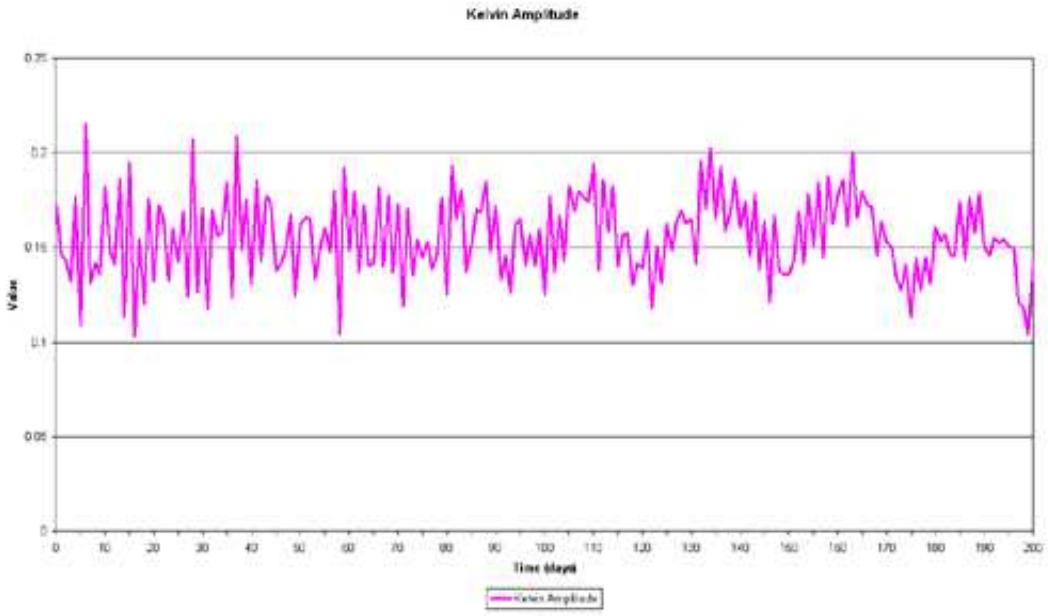

FIGURE 9.11: Kelvin wave amplitude with hill at 5° over 200 days.

9.5 Conclusions for Kelvin wave analysis

In addition to previous analysis, a much longer 200 day integration was run in order to determine the long-term impact of a hill placed 5° from the equator. Figure (9.11) shows the amplitude of the Kelvin waves at the equator for that 200 day period. Whilst the pattern appears chaotic, after roughly 100 days one may infer an oscillatory pattern over 22 to 30 days.

What has been shown in this chapter is that equatorial Kelvin waves diagnosed within results from the CASL methods, are clearly seen to be easily generated by topography in the equatorial region. Since these waves play a key part in the ENSO mechanism, their analysis here provides an indication of their sensitivity to disturbances near the equator, and is the first step to better understanding their role in ENSO.

9.6 Linking the Kelvin wave analysis to ENSO phenomenon detailed in previous work

This section aims to provide value in the previous analysis of Kelvin waves and the important role they play in the ENSO phenomenon by visiting previous work on El Niño events. [21] describes how altimeter data has been filtered to show Kelvin waves in the ocean thermocline. This imagery was then used to hypothesise a link between atmospheric phenomenon, known as the Madden Julian Oscillation (MJO), which displays westerly wind bursts, and the ENSO phenomenon, via the resulting production of oceanic Kelvin waves, [34, 41]. In particular, [34] assumes that the existing SST field is advected by anomalous currents to produce the anomalous warming, seen in the first few months of the 1982 El Niño, induced by downwelling Kelvin wave fronts. This connection was first hypothesised by Gill [31] and subsequent numerical experiments with nonlinear oceanic models, [34], have supported this basic premise. In this paper a primitive two-layer model is initialised to the conditions seen in June 1982 and a zonally confined uniform westerly wind patch was introduced, moving eastward 1 degree per day. This shows similarities to the simplistic test case presented in the previous chapter and proved to closely model the 1982 El Niño events.

The CASL method has captured the Kelvin waves in detail, allowing quick analysis of the effect of varying the position of topography, creating a pertubation leading to the generation of varying strengths of Kelvin waves. More recently, a case study by Yu et. al in 2003 [79] also speculates the effects of westerly wind bursts on the ENSO mechanism indicated by observation and data. This continuing line of enquiry into the ENSO mechanism shows that the full extend of the inter-relationships found between the ocean and atmosphere, leading to severe weather events such as El Niño and La Nina are still not fully understood. It is the authors

hope that analysis of the key dynamics, such as the Kelvin and Rossby waves, in these systems, using more advanced and detailed modelling techniques lead to a greater understanding and prediction of the ENSO phenomenon.

Chapter 10

Conclusions

Within this thesis variations of the CASL model have been outlined. The original two-dimensional barotropic algorithm was modified to suit the SWEs in spherical geometry. Several modifications of the original SWE algorithm were implemented that led to significant improvements in accuracy, without compromising efficiency. The unique merits of the CASL method include the representation of PV by contours, detailed in Chapter 2.2.1, which allows the model to retain fine details of this theoretically conserved field without severe detriment to the efficiency of the algorithm. Finite differencing procedures, presented under simple test conditions in previous chapters were modified to take advantage of this efficiency and again increase accuracy for the main fields of depth, divergence and PV.

Focusing on a standard test case, the dynamical fields' dependence on numerical parameters was assessed. This led to further improvements in the algorithm, demonstrated for the same test case. An important extension to this test case was also implemented and this resulted in a more reproducible, rigorous numerical analysis of the algorithm. The perturbation of the Rossby-Haurwitz test case leads to some important messages: the original test cases, commonly used in benchmarking numerical methods, may now be revised to more rigorously test the

numerics on the ever increasing power of today's computers. This allows one to focus on areas commonly thought of as complex, not only gaining feedback quickly, but also to a higher degree of accuracy. In addition, the time-step used by many numerical methods was shown to present an issue and a maximum time-step was recommended for use in this test case in order to ensure an acceptable degree of accuracy.

Using the results from the test case extension, an improved numerical method was detailed and the repercussions documented, with back-to-back testing of the two methods. This improved algorithm, exploiting the near balance exhibited by shallow-water flows at moderate Froude and Rossby numbers, showed an increase in accuracy, with conservation improved and dynamical fields more accurately represented.

After taking inspiration from many talks given at a conference on modern mathematical methods in physical oceanography in Colorado, the CASL algorithm was applied to study the genesis of the equatorial Kelvin waves, with emphasis on linking the results to the El Niño Southern Oscillation phenomenon in Chapter 8. Whilst a complete understanding of this phenomenon is still some way off, the effect of topography at varying latitudes on equatorial Kelvin waves was examined and some interesting results were gained from this analysis.

10.1 Further areas of research within the Vortex Dynamics Group, St Andrews

The successful inclusion of simple topography acting in the CASL method within this thesis and the "real-world" ENSO mechanism test case presented leads to the idea for development of realistic topography. This would be a major undertaking,

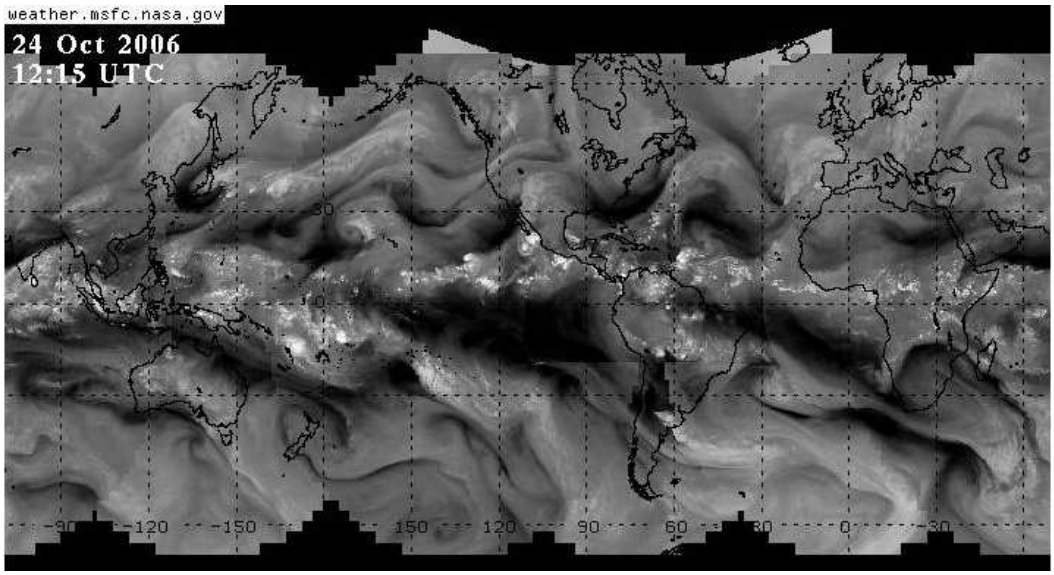

FIGURE 10.1: Satellite water vapour data.

but could lead to significant gains in further development within realistic test conditions. Figure (10.1) gives an indication as to how complex true atmospheric dynamics can be, even on a global scale.

In addition, for longer duration test cases, a slight relaxation of overall PV conservation may improve the results gained. This relaxation is seen within atmospheric and oceanic observations and certain constraints, placed on the properties of mixing and transport of particles across atmospheric layers, may thus be able to be revised [36]. The introduction of non-conservative effects acting on the PV field would then allow processes such as thermal forcing and Ekman transportation to be included within the algorithm [14].

Work currently being undertaken by members within the Vortex Dynamics group includes the testing and development of a multi-layer model and the implications of this advance are wide ranging. Examining the stratification of the atmosphere and oceans — beyond the highly-idealised shallow-water approximation made here — is important for realistic modelling. For example, the Atlantic meridional overturning circulation carries warmer waters to northern latitudes, returning the cool

water towards the equatorial regions. The slowing of this process over the past 50 years has implications for the climate over Europe [5] and, as such, carries much weight in the search for an accurate global model.

Specific to the CASL algorithm, Dr. Ali Mohebalhojeh has recently implemented an extension to the $CA_{\delta,\gamma}$ algorithm outlined in Chapter 6 to multiple layers, with diabatic forcing. The algorithm is applicable to models of the atmosphere from middle troposphere to mesosphere. As a continuation, this shall be tested and further extended to include continuous stratification with comprehensive treatment of lower and upper boundaries.

Finally, to demonstrate the speed at which the CASL method is able to resolve fine-scale detail, Prof Dritschel's comparison of CASL and pseudo-spectral methods at resolutions of 512^2 for the CASL method vs the 4096^2, required by the pseudo-spectral algorithm used, for a Navier-Stokes simulation show that much higher Reynolds numbers[1], R_e, are able to be achieved with the CASL model.

Figure (10.2) shows the pseudo-spectral and CASL algorithm comparison at the resolutions above. With the very high Reynolds numbers able to be captured within the CASL method, at a fraction of the computational cost, many more fine detail structures are retained which do contribute to the flow. The overall time taken for the models to complete the run is vastly different due to the very high resolution required by the pseudo-spectral method in order to achieve a suitable level of detail for comparison, clearly a major advantage of the CASL method.

[1]Within geophysical fluid dynamics, such high Reynolds numbers are incredibly difficult to obtain in numerical simulation and this may be seen as a major stumbling block for many models

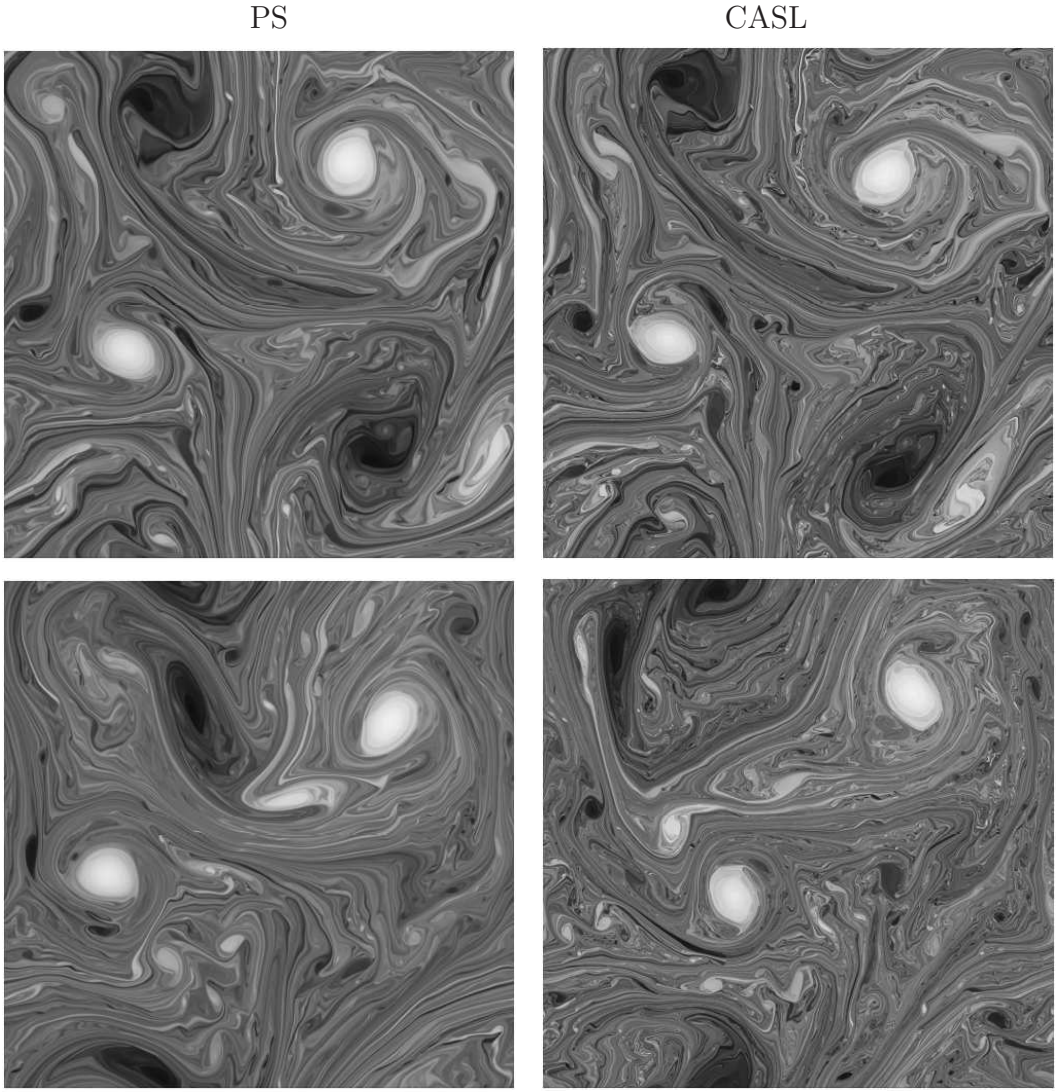

FIGURE 10.2: PV fields at days 12 (top) and 16 (bottom) for a Navier-Stokes flow. The pseudo-spectral method, at 4096^2 resolution, took 8 days on 32 processors (left) and the CASL method, at 512^2 resolution, required just 0.1 days on 1 processor (right).

Appendix A

Bibliography

[1] R. ASSELIN, Frequency filter for time integrations. *Mon. Wea. Rev.* **100**, 487-490, (1972).

[2] J. P. ANGELL, T. R. ROBINSON & S. P. LAWRENCE, TOPEX/Poseidon observations of Kelvin, Rossby and tropical instability waves in the equatorial Pacific Ocean. *Adv. in Space Research*, **22 (11)**, 1561-1565, (1998).

[3] J. R. BATES, Y. LI, A. BRANDT, S. F. MCCORMICK & J. RUGE, A global shallow-water numerical model based on the semi-Lagrangian advection of potential vorticity. *Quart. J. Roy. Meteor. Soc.* **121**, 1981-2005, (1995).

[4] D. S. BATTISTI, Dynamics and thermodynamics of a warming event in a coupled tropical atmosphere-ocean model. *J. Atmos. Sci.* **45**, 2889-2919, (1988).

[5] H. BRYDEN, H. LONGWORTH & S. CUNNINGHAM, Slowing of the Atlantic meridional overturning circulation at 25° N. *Nature* **438**, (7068), 655-657, (2005).

[6] J. CHO, M. DE LA TORRE JUÁREZ, A. INGERSOLL, D. DRITSCHEL, A high-resolution, three-dimensional model of jupiter's Great Red Spot. *J. geophys. res.*, **106**, 5099-5105, (2001).

[7] T. DELCROIX, J. PICAUT, & G. ELDIN, Equatorial Kelvin and Rossby Waves Evidenced in the Pacific Ocean Through Geosat Sea Level and Surface Current Anomalies. *J. Geophys. Res*, **96 supplement**, 3249-3362, (1991).

[8] D. G. DRITSCHEL, Contour surgery: a topical reconnection scheme for extended integrations using contour dynamics. *J. Comp. Phys.*, **77**, 240-266, (1988).

[9] D. G. DRITSCHEL, Contour dynamics/surgery on the sphere. *J. Comp. Phys.*, **78**, 477-483, (1988).

[10] D. G. DRITSCHEL, Contour dynamics and contour surgery: numerical algorithms for extended, high-resolution modelling of vortex dynamics in two-dynamics, inviscid, incompressible flows. *Comput. Phys. Rep.*, **10**, 77-146, (1989).

[11] D. G. DRITSCHEL, A new spherical shallow-water model: building in wave-vortex decomposition. *Seminar on Recent developments in numerical methods for atmospheric and ocean modelling*, ECMWF, (6-10 September 2004). http://www-vortex.mcs.st-andrews.ac.uk/~rks1/papers/D04.pdf

[12] D. G. DRITSCHEL, Numerical Simulation of Geophysical Flows. *Seminar on modern mathematical methods in physical oceanography, Breckenridge, CO*, Collaborations in Mathematical Geosciences, (13-23 August 2006). http://www-vortex.mcs.st-andrews.ac.uk/~rks1/papers/D06.pdf

[13] D. G. DRITSCHEL & M. H. P. AMBAUM, A contour-advective semi-Lagrangian algorithm for the simulation of fine-scale conservative fields. *Quart. J. Roy. Meteorol. Soc.* **123**, 1097-1130, (1997).

[14] D. G. DRITSCHEL & M. H. P. AMBAUM, The diabatic contour-advective semi-Lagrangian algorithm. *Mon. Wea. Rev.* **Vol 134**, 2503 - 2514, (2006).

[15] D. G. DRITSCHEL, & M. DE LA TORRE JUÁREZ, The instability and breakdown of tall columnar vortices in a quasi-geostrophic fluid. *J. Fluid Mech.* **328**, 129-160, (1996).

[16] D. G. DRITSCHEL, L. M. POLVANI & A. R. MOHEBALHOJEH, The Contour-Advective Semi-Lagrangian Algorithm for the Shallow-Water Equations. *Mon. Wea. Rev.* **127**, 1551-1565, (1999).

[17] D. G. DRITSCHEL & Á. VIÚDEZ, A balanced approach to modelling rotating stably stratified geophysical flows. *J. Fluid Mech.* **488**, 123-150, (2003).

[18] D. G. DRITSCHEL & Á. VIÚDEZ, The persistence of balance in geophysical flows. *J. Fluid Mech.* (Under review).

[19] D. DURRAN, The third-order Adams-Bashforth method: an attractive alternative to leapfrog time differencing. *Mon. Wea. Rev.*, **119**, 702-720, (1999).

[20] F. ECCLES & E. TZIPERMAN, Nonlinear effects on ENSO's period. *J. Atmos. Sciences*, **61**, 474-482, (2003).

[21] L. EDWARDS, R. HOUSEAGO-STOKES & P. CIPOLLINI, Alimeter observations of the MJO/ENSO connection through Kelvin waves. *International J. of Remote Sensing*, **27(6)**, 1193-1203, (2005).

[22] H. ERTEL, Ein neuer hydrodynamischer Erhaltungssatz. *Naturwissenschaften*, **30**, 543-544, (1942).

[23] H. ERTEL, Ein neuer hydrodynamischer Wirbelsatz. *Meteor. Z.*, **59**, 277-281, (1942).

[24] H. ERTEL, Über das Verhältnis des neuen hydrodynamischen Wirbelsatzes zum Zirkulationssatz von V. Bjerknes. *Meteor. Z.*, **59**, 385-387, (1942).

[25] H. ERTEL, Über hydrodynämische Wirbelsatze. *Phys. Z.*, **43**, 526-529, (1942).

[26] V. ESFAHANIAN, S. GHADER, & A. R. MOHEBALHOJEH, On the use of the super compact scheme for spatial differencing in numerical models of the atmosphere. *Quart. J. Roy. Meteorol. Soc.* **131**, 2109, (2005).

[27] K. S. GAGE, Radar observations of the free atmosphere: Structure and dynamics. *Radar in Meteorology, D. Atlas, Ed.*, American Meteorological Society, Boston, 534-545, (1990).

[28] K. S. GAGE & G. D. NASTROM, On the spectrum of atmospheric velocity fluctuations seen by MST/ST radar and their interpretation. *Radio Sci.*, **20**, 1339-1347, (1985).

[29] P. R. GENT & J. C. MCWILLIAMS, Isopycnal mixing in ocean circulation models. *J. Phys. Oceanogr.* **20**, 150-155, (1982).

[30] A. GILL, Atmosphere-Ocean Dynamics. *International Geophysics Series* **30**, (1982).

[31] A. GILL, An estimation of sea-level and surface-current anomalies during the 1972 El Niño and consequent thermal effects. *J. Phys. Oceanography* **13**, 586-606, (1982).

[32] S. GRAVEL, The semi-Lagrangian method. *Proc. Centre de Researches mathematiques*, Montreal, 1-11, (1996).

[33] S. M. GRIFFIES & E. TZIPERMAN, A linear thermohaline oscillator driven by stochastic atmospheric forcing. *J. Clim.* **8(10)**, 2240-2453, (1995).

[34] D. Harrison & P. S. Schopf, Kelvin-wave-induced anomalous advection and the onset of surface warming in El Niño events. *Mon. Weather Rev.* **112**, 923933, (1984).

[35] B. HAURWITZ, The motion of atmospheric disturbances on the spherical earth. *J. Marine Res.* **3**, 254-267, (1940).

[36] P. HAYNES, Transport and mixing in the atmosphere. *Mechanics of the* 21^{st} *century* **Springer Netherlands**, 139-152, (2005).

[37] B. J. HOSKINS, Stability of the Rossby-Haurwitz wave. *Quart. J. Roy. Meteorol. Soc.* **99**, 254-267, (1973).

[38] B. J. HOSKINS, M. E. MCINTYRE & A. W. ROBERTSON, On the use and significance of isentropic potential-vorticity maps. *Quart. J. Roy. Meteorol. Soc.* **111**, 877-946, (1985).

[39] W. S. KESSLER, Can Reflected Extra-Equatorial Waves Drive ENSO? *J. Phys. Oceanography*, **21**, 444-452, (1990).

[40] W. S. KESSLER & M. J. MCPHADEN, The 1991-1993 El Niño in the central Pacific. *Deep Sea Research Part II: Topical Studies in Oceanography* **42(2)**, 295-333, (1995).

[41] R. Knox & D. Halpern, Long range Kelvin wave propagation of transport variations in Pacific Ocean equatorial currents. *J. Mar. Res.* **40**, 329339, (1982).

[42] B. LEGRAS & D. G. DRITSCHEL, A comparison of the contour surgery and pseudo-spectral methods. *J. Comp. Phys.* **104**, 287-302, (1993).

[43] C. MACASKILL & B. M. BERWICK, The use of hyperviscosity in simulations of geophysical fluid flows. *Proc.* 12^{th} *Aus. Fluid Mech. Conf.*, Sydney, Australia, 415-418, (1995).

[44] M. E. MCINTYRE & W. A. NORTON, Potential vorticity inversion on a hemisphere. *J. Atmos. Sci.* **57**, 1214-1235, (Corrigendum **58**, 949), (2000).

[45] W. M. MCKIVER & D. G. DRITSCHEL, Balance in non-hydrostatic rotating stratified turbulence. *J. Fluid Mech.*, (under review).

[46] J. C. MCWILLIAMS, Statistical properties of decaying geostrophic turbulence. *J. Fluid Mech.* **198**, 199-230, (1989).

[47] J. C. MCWILLIAMS, The vortices of geostrophic turbulence. *J. Fluid Mech.* **219**, 387-404, (1990).

[48] J. METHVEN & B. HOSKINS, The advection of high resolution tracers by low resolution winds. *J. Atmos. Sci.*, **56**, 3262-3285, (1999).

[49] A. R. MOHEBALHOJEH & D. G. DRITSCHEL, On the representation of gravity waves in numerical models of the shallow water equations. *Quart. J. Roy. Meteorol. Soc.* **126**, 669-688, (2000).

[50] A. R. MOHEBALHOJEH & D. G. DRITSCHEL, Hierarchies of balance conditions for the f-plane shallow-water equations. *J. Atmos. Sci.* **58(16)**, 2411-2426, (2001).

[51] A. R. MOHEBALHOJEH & D. G. DRITSCHEL, Contour-advective semi-Lagrangian algorithms for the spherical shallow water equations. *submitted to Elsevier Science 2006.*

[52] S. MOORTHI & R. W. HIGGINS, Application of fast Fourier transforms to the direct solution of a class of two-dimensional separable elliptic equations on the sphere. *Mon. Weather Rev.* **121**, 290, (1993).

[53] J. NORBURY & I. ROULSTONE, Large-scale atmosphere-ocean dynamics. *Cambridge University Press*, (2002).

[54] W. A. NORTON, Breaking Rossby waves in a model stratosphere diagnosed by a vortex-following coordinate system and a technique for advecting material contours. *J. Atmos. Sci.* **51**, 654-673, (1994).

[55] L. M. POLVANI, J. C. MCWILLIAMS, M. A. SPALL & R. FORD, The coherent structures of shallow-water turbulence: deformation-radius effects, cyclone/anticyclone asymmetry and gravity-wave generation. *Chaos* **4**, 177-187, (1994).

[56] H. RITCHIE, A contour-advective semi-Lagrangian algorithm for the simulation of fine-scale conservative field. *Mon. Wea. Rev.* **117**, 1587-1598, (1998).

[57] H. RITCHIE, C. TEMPERTON, A. SIMMONS, H. HORTAL, T. DAVIES, D. DENT & M. HARMUD, Implementation of the semi-Lagrangian method in a high resolution version of the ECMWF forecast model. *Mon. Wea. Rev.* **123**, 489-514, (1995).

[58] A. J. ROBERT, The Integration of a Low Order Spectral Form of the Primitive Meteorological Equations, *J. Meteor. Soc. Japan*, **Ser. 2, Vol. 44, NO. 5**, 237-245, (1966).

[59] C. RONCHI, R. IACONO & P. S. PAOLUCCI, The "Cubed Sphere": A new method for the solution of partial differential equations. *J. Comp. Phys.* **124(1)**, 93-114, (1996).

[60] C. G. ROSSBY, Planetary flow patterns in the atmosphere. *Quart. J. Roy. Meteor. Soc.*, **66** (Suppl.), 68-87, (1940).

[61] J. SHIPTON & D. G. DRITSCHEL, Balance and gravity waves in spherical shallow-water turbulence. *J. Fluid Mech.* (under review).

[62] S. DE SILVA, Global change: Eruptions linked to El Niño. *Nature*, **426 (6964)**, 239, (2003).

[63] A. J. SIMMONS, B. J. HOSKINS & D. M. BURRIDGE, Stability of the semi-implicit method of time integration. *Mon. Weather Rev.* **106**, 405-412, (1978).

[64] R. SMITH & D. G. DRITSCHEL, Revisiting the Rossby-Haurwitz wave test with contour-advection. *J. Comp. Phys.* **217 (2)**, 473-484, (2006).
http://www-vortex.mcs.st-andrews.ac.uk/~rks1/papers/SD06.pdf

[65] A. STANIFORTH & J. CÔTÉ, Semi-Lagrangian integration schemes for atmospheric models - A review. *Mon. Weather Rev.* **119**, 2206-2223, (1991).

[66] M. J. SUAREZ & P. S. SCHOPF, A delayed action oscillator for ENSO. *J. Atmos. Sci.* **45**, 3283-3287, (1988).

[67] J. THUBURN & Y. LI, Numerical simulations of Rossby-Haurwitz waves. *Tellus A* **52 (2)**, 181-189, (2000).

[68] M. A. TOLSTYKH, Vorticity-divergence semi-Lagrangian shallow-water model of the sphere based on compact finite differences. *J. Comput. Phys.* **179**, 180 (2002).

[69] E. TZIPERMAN, L. STONE, M. CANE, & H. JAROSH, El Niño Chaos: Overlapping of Resonances between the Seasonal Cycle and the Pacific Ocean-Atmosphere Oscillation. *Science*, **264**, 72-74, (1994).

[70] E. TZIPERMAN, M. CANE, & S. ZEBIAK, Irregularity and locking to the seasonal cycle in an ENSO prediction model as explained by the quasi-periodicity route to chaos. *J. Atmos. Sciences*, **52**, 293-306, (1995).

[71] G. K. VALLIS, Potential vorticity inversion and balanced equations of motion for rotating and stratified flows. *Quart. J. Roy. Meteorol. Soc.*, **122**, 291-322, (1996).

[72] G. K. VALLIS, Atmospheric and Oceanic Fluid Dynamics: Fundamentals and Large-Scale Circulation. *Cambridge University Press*, (2006).

[73] G. VECCI, B. SODEN, A. WITTENBERG, I. HELD, A. LEETMAA & M. HARRISON, Weakening of tropical Pacific atmospheric circulation due to anthropogenic forcing. *Nature* **441**, 73-76, (2006).

[74] Á. VIÚDEZ & D. G. DRITSCHEL, Optimal potential vorticity balance of geophysical flows. *J. Fluid Mech.* **521**, 343-352, (2004).

[75] G. T. WALKER, On periodicity (with discussion). *Quart. J. Roy. Meteorol. Soc.*, **51**, 337-346, (1925).

[76] D. W. WAUGH, & R. A. PLUMB, Contour-advection with surgery: A technique for investigating fine scale structure in tracer transport. *J. Atmos. Sci*, **51**, (1994).

[77] D. L. WILLIAMSON, J. B. DRAKE, J. J. HACK, R. JAKOB & P. N. SWARZTRAUBER, A Standard Test Set for Numerical Approximations to the Shallow-Water Equations on the Sphere. *J. Comp. Phys.*, 221-224, (1992).

[78] World Disasters Report, *International Federation of Red Cross and Red Crescent Societies*, (1999).

[79] L. YU, R. WELLER & T. LIU, Case analysis of a role of ENSO in regulating the generation of westerly wind bursts in the Western Equatorial Pacific. *J. Geophys. Research.*, **108**, (2003).